https://ntrs.nasa.gov/search.jsp?R=19910009749 2020-03-19T18:40:37+00:00Z

NASA Technical Memorandum 102206

An Experimental Study of the Turbulent Boundary Layer on a Transport Wing in Subsonic and Transonic Flow

Frank W. Spaid, Frederick W. Roos,
and Raymond M. Hicks

IN-02
2514

(NASA-TM-102206) AN EXPERIMENTAL STUDY OF THE TURBULENT BOUNDARY LAYER ON A TRANSPORT WING IN SUBSONIC AND TRANSONIC FLOW (NASA) 78 p CSCL 01A

N91-19062

Unclas
G3/02 0002514

August 1990

National Aeronautics and
Space Administration

NASA Technical Memorandum 102206

An Experimental Study of the Turbulent Boundary Layer on a Transport Wing in Subsonic and Transonic Flow

Frank W. Spaid and Frederick W. Roos
McDonnell Douglas Research Laboratories, St. Louis, Missouri

Raymond M. Hicks
Ames Research Center, Moffett Field, California

August 1990

National Aeronautics and
Space Administration

Ames Research Center
Moffett Field, California 94035-1000

TABLE OF CONTENTS

PAGE ii INTENTIONALLY BLANK

PRECEDING PAGE BLANK NOT FILMED

NOMENCLATURE

b	wingspan
c	section chord
c_ℓ	section lift coefficient
C_L	wing lift coefficient
C_f	local skin friction coefficient, τ/q_e
C_p	pressure coefficient, $(p - p_\infty)/q_\infty$
H	streamwise boundary-layer shape factor, δ_1^* / θ_{11}
k	height of roughness element
M	Mach number
p	pressure
q	dynamic pressure, $(1/2)\rho u^2$
Re_c	Reynolds number based on chord
u	velocity magnitude
u_s	component of velocity parallel to flow direction at the boundary-layer edge
u_τ	shear velocity, $\sqrt{\tau_w / \rho}$
w	component of velocity normal to flow direction at the boundary-layer edge
x	coordinate measured parallel to free-stream direction
y	spanwise coordinate
z	coordinate normal to wing mean reference plane
z^+	law-of-the-wall coordinate, zu_τ/ν_w
α	angle of attack with respect to model planform reference plane
β	yaw-plane flow-direction angle, measured with respect to u_∞, positive outboard

PAGE iv INTENTIONALLY BLANK PRECEDING PAGE BLANK NOT FILMED

δ boundary-layer thickness

δ_1^* streamwise displacement thickness, $\int_0^\delta \left(1 - \frac{\rho u_s}{\rho_e u_e}\right) dz$

δ_2^* crossflow displacement thickness, $-\int_0^\delta \frac{\rho w}{\rho_e u_e} dz$

η spanwise coordinate normalized by the semispan, 2y/b

θ_{11} streamwise momentum thickness, $\int_0^\delta \frac{\rho u_s}{\rho_e u_e}\left(1 - \frac{u_s}{u_e}\right) dz$

Λ sweep angle

ν kinematic viscosity

ρ density

τ shear stress

Subscripts

e conditions at edge of boundary layer

rms root-mean-square value of fluctuation

t location of boundary-layer transition

w conditions at surface

∞ free-stream conditions

SUMMARY

The upper-surface boundary layer on a transport wing model was extensively surveyed with miniature yaw probes at a subsonic and a transonic cruise condition. Additional data were obtained at a second transonic test condition, for which a separated region was present at mid-semispan, aft of mid-chord. Significant variation in flow direction with distance from the surface was observed near the trailing edge except at the wing root and tip. The data collected at the transonic cruise condition show boundary-layer growth associated with shock-wave/boundary-layer interaction, followed by recovery of the boundary layer downstream of the shock. Measurements of fluctuating surface-pressure and wingtip acceleration were also obtained. The influence of flow-field unsteadiness on the boundary-layer data is discussed. Comparisons among these data and predictions from a variety of computational methods are presented. The computed predictions are in reasonable agreement with the experimental data in the outboard regions where three-dimensional effects are moderate and adverse pressure gradients are mild. In the more highly loaded mid-semispan region near the trailing edge, displacement-thickness growth was significantly underpredicted, except when unrealistically severe adverse pressure gradients associated with inviscid calculations were used to perform boundary-layer calculations.

INTRODUCTION

The predictions of methods for computing wing flow fields need to be evaluated by comparisons with experimental data, for accuracy and range of applicability (ref. 1). Detailed low-speed experiments in flows related to the flow about a swept wing are reported by van den Berg et al. (ref. 2) and Seetharam et al. (ref. 3), but the existing transonic investigations are limited in scope. Survey data describing the boundary layer and wake of a swept wing near its trailing edge at mid-semispan, obtained from flight tests of the F-111 transonic aircraft technology (TACT) aircraft, are reported by Lux (ref. 4). Boundary-layer measurements near mid-chord on the ONERA M-6 wing in transonic flow are reported by Schmitt et al. (ref. 5). Boundary-layer measurements on a low-aspect-ratio wing in transonic flow are reported by Keener (ref. 6); they include multiple-orifice probe surveys forward of mid-chord and laser velocimeter surveys near the trailing edge at mid-semispan. The present report describes efforts to provide experimental descriptions of the boundary layer on most of the upper surface of a typical transport wing in both subsonic and transonic flow. Data from this investigation are also presented in references 7–9. The experiment was limited to the measurement of mean velocity profiles; although turbulence measurements in three-dimensional boundary layers are needed, the practical difficulties associated with making turbulence measurements as part of the present experiment were excessive. This investigation is part of a cooperative program among McDonnell Douglas Research Laboratories (MDRL), Douglas Aircraft Company (DAC), and the Ames Research Center (ARC), and was supported in part under the McDonnell Douglas Independent Research and Development program.

FACILITIES AND EQUIPMENT

The experiments were conducted in the Ames 14-Foot Transonic Wind Tunnel. This facility is a continuous-flow tunnel; the stagnation pressure is atmospheric, and the stagnation temperature is controlled by exchanging air with the surrounding atmosphere. The semispan model of the wing and fuselage, with the probe traversing assembly, are shown in figure 1, installed in the test section of the wind tunnel. The test-section walls are slotted, but steel plates were used to cover the floor slots during this test.

The model was obtained from DAC, selected because it was the largest high-speed model available and had no leading- or trailing-edge devices. It has a 1.113-m semispan and a 0.359-m mean aerodynamic chord and is instrumented with 378 static-pressure orifices located at nine spanwise stations. Figure 2 is a drawing of the model and includes some geometric properties of the wing. The fuselage is one-half of a body of revolution, under which a 3.18-cm-thick uniform section was added. An auxiliary wing holding a probe traversing unit is attached to the fuselage downstream of the primary wing. The undisturbed tunnel-wall boundary layer is approximately 18-20 cm thick at the model station (ref. 10 and unpublished data), the displacement thickness is approximately 3.2 cm, and the ratio of the undisturbed velocity at the height of the wing root (16.5 cm above the tunnel floor) to the free-stream velocity is approximately 0.97. The model is small relative to the test section; the blockage ratio is 0.45%, and the ratio of semispan to tunnel height is 0.26.

For an associated experiment on transonic wing buffeting, several types of dynamic instrumentation were incorporated into the model (fig. 2). In addition to their primary function, these instruments indicated the degree of unsteadiness in the flow environment during the boundary-layer measurements. Three chordwise sets of high-frequency-response miniature pressure transducers were embedded in the upper surface of the model wing. The installation method, essentially identical to the one used earlier with two-dimensional airfoil models and described in reference 11, provided a fluctuating-pressure frequency response that was flat within 5% from dc to beyond 10 kHz. Other dynamic instrumentation included an accelerometer buried in the wingtip with its sensitive axis perpendicular to the wing plane, and strain gauge bridges at the wing root for dynamically monitoring wing bending and torsion loads. The primary results from the nonsteady portion of this study are reported separately (ref. 12), but nonsteady data pertinent to interpretation of the boundary-layer data are included here.

Good technique in obtaining three-dimensional boundary-layer data typically includes the use of miniature, multisensor pitot or hot-wire probes attached to the wing surface near the measuring station, and alignment of the tips with the local flow direction by a nulling technique. This approach minimizes probe interference effects and probe vibration, and allows accurate measurement of probe location. It also requires considerable test time to obtain a survey and make model changes between surveys. The high cost of operating large transonic wind tunnels and their limited availability for research investigations precluded that approach.

A two-degree-of-freedom traversing unit allowing remote streamwise positioning, and fixed-position probe tips for flow-direction measurements, were required to complete the experiment in

approximately one month of tunnel occupancy. Initially, a traversing unit was designed that would attach to the lower surface of the wing. The minimum dimensions of this unit were established by the 6.35-cm diameter of available stepper motors and position encoders. Panel-method calculations showed that the design would produce excessive flow-field interference, and it was therefore rejected.

The traversing mechanism used in this study was mounted on an auxiliary wing that was attached to the fuselage downstream of the primary wing (fig. 2). The constant-chord auxiliary wing is swept 20° and lies approximately in the mean chord plane of the primary wing. The auxiliary wing is mounted at −1.5° incidence relative to the fuselage centerline since panel-method calculations indicate that this alignment minimizes interference in the flow about the primary wing at subsonic conditions. The auxiliary wing has a remotely actuated trailing-edge flap for minimizing interference at test conditions other than the primary subsonic condition. The flap chord is 20% of the auxiliary wing chord. A strut connecting the two wingtips minimizes their relative unsteady motion. The strut is pinned to the primary wing and to the auxiliary wing near its leading edge. A remotely actuated pneumatic clamp is located near the auxiliary-wing trailing edge. The clamp is sized to resist forces associated with the anticipated unsteady relative deflections, but to allow movement under the much larger aerodynamic loads associated with static deflections.

A two-degree-of-freedom traversing unit was installed at each of nine spanwise stations on the auxiliary wing, allowing boundary-layer profiles to be obtained along each row of static-pressure orifices. The principal features of the traversing unit are shown in figure 3. Probe tips are attached to a rectangular probe shaft which moves through a housing containing the horizontal-drive stepper motor, horizontal-position encoder, and instrumentation-lead spool. A portion of each instrumentation lead (plastic tubing) lies alongside the probe shaft, from the downstream end of the shaft to the rewind spool. The tubing is covered by a windshield, so the leads are never exposed to the airstream. As the shaft is extended in the upstream direction, the tubing is transferred from the shaft to the spool; it is returned when the direction of motion reverses. Maximum streamwise travel is 48 cm, with a resolution of 0.0866 mm per encoder pulse.

The design of this traversing unit and auxiliary wing was a compromise between rigidity and flow-field interference. The initial configuration did not include the aft supporting structure connecting the probe shaft and horizontal motor-encoder assembly to the main structure attached to the auxiliary wing; however, excessive oscillations of the traversing unit were observed during the first tunnel occupancy period, and the aft supporting structure was added. During this experiment, the probe shaft could not be extended forward more than 28 cm without excessive motion parallel to the plane of the wing. Additional streamwise extension was made possible by installing a stiffener, which was attached to the streamwise motor-encoder housing and which provided a supporting channel for the probe shaft to extend an additional 17.8 cm upstream of the housing.

Motion and readout in the direction normal to the wing are provided by a similar motor-encoder assembly installed in the airfoil-shaped strut located below the auxiliary wing. Since the range of travel normal to the wing is only 7.6 cm, this motion can be accommodated by a coil of instrumentation leads within the strut. Position resolution is 0.0052 mm per encoder pulse. Play and backlash are eliminated in both directions by spring-loaded bearings and antibacklash gearing. Limit switches stop the stepper motors at the extremes of both ranges of travel.

Probe tips are small, flat, three-orifice yaw probes (fig. 4) similar to those described in reference 13. (Because of the viewing angle, only two orifices are visible in the tip detail of figure 4.) Calibration of these probes allowed determination of the flow speed and flow direction in the plane of the wing. Three probes with the same nominal tip geometry were used during this study. The initial experiments were conducted with probe 1, which was used for boundary-layer surveys at the five inboard stations, $0.165 \le \eta \le 0.650$, where η is the spanwise distance normalized by the semispan. This probe was subsequently damaged, and probe 2 was used for almost all remaining experiments, including surveys at spanwise stations 0.300, 0.450, and 0.650, where data had been obtained with the first probe. Probe 3 was used only at $\eta = 0.300$, $x/c \ge 0.5$, where x/c is the local streamwise distance from the leading edge normalized by the local chord. Probes 2 and 3 were recalibrated after the test; the post-test calibrations were in excellent agreement with the pre-test calibrations.

A number of boundary-layer profiles at inboard stations near the trailing edge were obtained outside the pitch angle range of $\pm 10°$, within which errors in measured stagnation pressure are negligible. Post-test calibration data appropriate to the actual pitch misalignment range were used to reduce the data obtained with probes 2 and 3. Errors in measured yaw angle caused by pitch misalignment were small, and no corrections to yaw angle for effects of pitch misalignment were made. Values of stagnation pressure at the boundary-layer edge in subsonic flow, obtained from probes 2 and 3, agreed with the free-stream values to within 0.5% for 85% of the profiles. Typical errors in data obtained with the first probe were larger, but the satisfactory agreement between data obtained with the first probe and with the second and third probes (to be presented later) indicates that effects of pitch misalignment in the data from the first probe are minor.

The probe tips were electrically insulated from the probe shaft to allow the wing surface to be located by an electrical contact during a test. The electrical connection from the probe tip to the relay controlling the contact warning light was made by an insulated wire connecting the probe tip to a spring-loaded pin at the opposite end of the probe shaft, which made a sliding contact with a conducting strip in the windshield. Contact of the probe tip with the wing surface caused a relay to interrupt power to the vertical stepper motor, to prevent probe tip damage.

Probe data and test-section conditions were recorded with the aid of a control unit and a microcomputer, and were stored on diskettes. The control unit was used in a manual mode to position the probe at the desired streamwise location and bring the tip into contact with the wing surface. A boundary-layer survey was performed by a preprogrammed sequence of probe motions and data acquisition cycles. A pressure transducer was connected to each probe orifice through a fluid switch wafer. This device allowed the transducer to be connected to the probe orifice, to a known reference pressure, or to atmosphere. The switch was cycled at the beginning and end of each boundary-layer survey, allowing data for a two-point calibration of each transducer to be obtained. Data on test-section conditions and primary-wing static pressures were acquired by the wind tunnel data system.

Boundary-layer transition trips were applied on both upper and lower surfaces at 6% local chord, following the recommendations of Braslow et al. (ref. 14). The roughness elements were spherical glass beads with a nominal diameter of 0.13 mm. This size corresponds to 1.5k–2k, where k is the minimum size of an element that will cause transition to occur at the trip. The effectiveness of the trip was verified by the fluorene sublimation technique.

RESULTS AND DISCUSSION

Plotted data from this investigation are presented in the following sections. Tabulated static-pressure and boundary-layer profile data are presented on microfiche, located in a pocket inside the back cover of this report. A guide to the tabulated data is presented in the appendix.

Static Pressures and Tuft Flow Visualization

Extensive upper-surface boundary-layer data were obtained at the following two test conditions: 1) Mach number, $M_\infty = 0.50$; Reynolds number based on mean aerodynamic chord, $Re_c = 3.4 \times 10^6$; angle of attack, $\alpha = 6°$; and wing lift coefficient, $C_L = 0.583$; and 2) $M_\infty = 0.825$, $Re_c = 4.5 \times 10^6$, $\alpha = 4°$, and $C_L = 0.523$. A limited quantity of data were also obtained at $M_\infty = 0.825$, $Re_c = 4.5 \times 10^6$, $\alpha = 6°$, and $C_L = 0.650$.

Static-pressure distributions obtained at all nine spanwise pressure-orifice stations at the subsonic test condition are superimposed on the wing planform in figure 5. The suction peaks in these pressure distributions are strongest at the mid-semispan stations; they decrease near the tip as a result of the wing twist. Interference of the auxiliary wing and traversing unit with the flow about the primary wing, as indicated by static-pressure data, was no greater than differences associated with run-to-run repeatability for this test condition.

Prior to each boundary-layer survey, a set of wing static-pressure data was obtained with the probe near the surface, in position to begin the survey. Static-pressure distributions obtained upstream of the probe tip are superimposed in figure 6 on the corresponding distributions obtained with the probe retracted. The probe tip interference effects are similar to, but smaller than, the effects observed in the airfoil experiments reported in reference 15. Where interference effects are present, they usually take the form of an additional adverse static-pressure gradient. Interference associated with the probe tip was negligible when the probe tip was aft of mid-chord, and interference at forward survey stations was minor.

Static-pressure data for the transonic test condition at which most boundary-layer data were obtained ($M_\infty = 0.825$, $\alpha = 4°$) are presented in figure 7 in the format of figure 5. The Mach number, angle of attack, and corresponding lift coefficient are the design cruise conditions for this wing. Data obtained with the wing alone and with the wing plus the auxiliary wing are superimposed. The data show an upper-surface shock wave near mid-chord over most of the span; near the tip, the shock wave weakens and moves forward as a result of the wing twist. The influence of the auxiliary wing on the primary wing flow field is moderate.

In the static-pressure distributions of figure 8, data obtained with the auxiliary wing and the traversing unit installed at the spanwise station of the particular sub-plot are superimposed on data obtained with the wing alone. Section lift coefficients, c_ℓ, obtained from the wing-alone data, are also included. The traversing apparatus makes the C_p values slightly more positive, primarily aft of mid-chord, and shifts the shock slightly forward. The effect on the shock location is maximum at $\eta = 0.725$. The disturbance caused by the strut connecting the wings is apparently limited to the

lower-surface pressure distributions for $\eta \geq 0.9$. For $0.15 \leq \eta \leq 0.8$, the presence of the auxiliary wing and the traversing unit decreases the local section lift coefficients by an average of 0.025 relative to the wing-alone data.

Interference in the static-pressure distributions caused by the probe tip at $M_\infty = 0.825$ is illustrated in figure 9. Probe tip interference is negligible for $x/c > 0.6$ and is small elsewhere, except near the wing tip, where the scale of the probe tip relative to the local chord is maximum. Results of an attempt to determine the effects of similar static-pressure perturbations on boundary-layer properties are summarized in reference 15, where it is tentatively concluded that these effects are small if the noninterference C_p is used to compute velocities from pitot-pressure data.

Static-pressure data obtained at $M_\infty = 0.825$, $\alpha = 6°$ are presented in figure 10 in the manner of figures 5 and 7. The test condition of figure 10 corresponds approximately to the break in the C_L vs. α curve at this Mach number. The character of the pressure distribution at this angle of attack is similar to that obtained at $\alpha = 4°$ (see fig. 7), except for negative values of C_p near the trailing edge at mid-semispan. These negative C_p imply the existence of a separated region; fluorescent minituft flow visualization, surface-pressure-fluctuation measurements, and boundary-layer surveys all indicate separation at mid-semispan, aft of mid-chord, at this test condition.

Fluorescent minituft flow visualization photographs, taken at the test conditions shown in figures 5, 7, and 10, are presented in figure 11. The tufts are 0.05-mm-diam monofilament nylon, dyed with fluorescent dye and cemented to the model surface. The rows of tufts lie in planes parallel to the plane of symmetry of the model. The tuft pattern was photographed during a run, using ultraviolet flash photography. The minituft technique was developed by Crowder (ref. 16).

Significant flow unsteadiness was evident throughout this set of experiments, under attached-flow conditions as well as during separated-flow runs. The region of missing tufts in the central portion of the planform in figures 11b and 11c was caused by flow unsteadiness before these photographs were taken; the wing and tufts had been subjected to runs at several test conditions, including higher Mach numbers and angles of attack, which were associated with extensive regions of flow separation on the central portion of the wing. Unsteady chordwise shock movement was appreciable, not only producing the tuftless area in figures 11b and 11c, but also contributing to the spreading of the measured shock-pressure rise that is evident in figure 7. Because the unsteadiness of the flow field about the wing model has several implications for the boundary-layer measurements, it will be discussed in detail in a later section of this report.

As indicated by the tufts, the flow at the wing root at each test condition is essentially unyawed. Deviation of the tufts from the streamwise direction is minor at the subcritical condition (fig. 11a) except near the trailing edge, where outboard flow is indicated. At the transonic condition (fig. 11b) a moderate inboard component of flow is indicated on the forward portion of the wing along most of the span, and the flow is outboard on most of the aft portion, particularly near the trailing edge. The qualitative characteristics of the tuft patterns for all test conditions are similar at the tip. The two rows of tufts nearest the tip are significantly different from each other. The row nearest the tip shows the inboard flow forward and outboard flow aft, but the next row inboard does not show an outboard component of flow near the trailing edge. Separation is evident in the aft portion of the mid-semispan region in figure 11c, as is an indication of shock-wave/boundary-layer interaction at the

more inboard and outboard locations. Limited boundary-layer data were obtained at this test condition at inboard stations.

Boundary-Layer Profiles at the Subsonic Test Condition

Velocity magnitude and flow-direction profiles obtained at the subsonic test condition are presented in figure 12. The ordinate, z/c, is the distance from the surface normalized by the local chord, and the velocity magnitude, u, is normalized by the free-stream velocity. The flow inclination angle, β, is defined relative to the free-stream flow direction, and positive values of β correspond to outboard flow. The use of the free-stream direction as the reference for β allows the variation in flow direction both through the boundary layer and along the chord to be presented in a single plot. Data obtained at the spanwise station nearest the wing root, $\eta = 0.165$, are plotted in figure 12a. The side of the fuselage is roughly planar above the wing, except for a small fillet at the wing-fuselage intersection, and is located at $\eta = 0.127$, 4.2 cm inboard of this spanwise survey station. Mechanical interference at this station limited the boundary-layer data acquisition to $x/c \geq 0.4$. The velocity magnitude profiles are moderately full and show some scatter resulting from unsteadiness. The direction profiles show nearly streamwise, collinear flow in the aft region, with moderate outboard inclination at mid-chord near the surface.

The data of figure 12b, at $\eta = 0.300$, are qualitatively different from the data obtained at the root station, and are typical of the mid-semispan stations. Approximately 40 data points were obtained on each profile; individual data points are omitted from the plots at the forward chordwise stations for clarity. The velocity magnitude profiles at $\eta = 0.300$ show greater boundary-layer growth than those at the root station, and the flow-direction profiles show greater three-dimensionality. The flow is inboard and nearly collinear at the forward stations. The magnitude of the edge inclination decreases with increasing x/c, becoming nearly aligned with the free-stream direction near the trailing edge. Profiles at the aft chordwise stations show the flow direction changing from slightly inboard at the edge to outboard near the surface, a trend which becomes more pronounced as the trailing edge is approached. Velocity magnitude data sets obtained with different probes at the same chordwise station are in good agreement with each other. At this spanwise station, data for each chordwise station were obtained with probe 1. Repeat runs were made with probe 2 at $x/c \leq 0.5$ and with probe 3 at $x/c \geq 0.5$. Agreement between corresponding flow-direction profiles is good for the data obtained with probes 1 and 2, but it is poorer between profiles obtained at the aft chordwise stations with probes 1 and 3; values of β obtained with probe 3 are slightly more positive than corresponding values obtained with the other probes (recall that probe 3 was used only at $\eta = 0.300$, $x/c \geq 0.5$). The tips of probes 1 and 2 more closely approximate the nominal geometry shown in figure 4 than does the tip of probe 3. As a result, the calibration characteristics of probe 3 are significantly more nonlinear than the calibration data of the other probes. Some data points obtained near the surface with probe 3 at the aft chordwise stations exceed the calibration range and have been omitted.

Data obtained with both probes 1 and 2 at the next outboard spanwise station, $\eta = 0.450$, are presented in figure 12c. These data are qualitatively similar to the data of figure 12b, also showing good agreement between the β-profiles obtained with the two probes. Some data obtained near the surface with probe 1 for $x/c \leq 0.98$ exceed the calibration range and have been omitted.

The qualitative characteristics of the boundary-layer velocity magnitude and flow-direction profiles obtained at the next three spanwise stations, $\eta = 0.575$, 0.650, and 0.725 (figs. 12d-12f), are similar to the characteristics of the profiles obtained at $\eta = 0.300$ and 0.450. The influence of the wing twist, and the associated reduction in section lift coefficient with increasing η near the tip, is evident in the data obtained at the outboard stations, $\eta = 0.800$, 0.900, and 0.950 (figs. 12g-12i). The variation of flow direction with chordwise location at the boundary-layer edge is qualitatively the same as at the inboard stations. Profiles at forward chordwise locations are approximately collinear. Both the growth in boundary-layer thickness with increasing chordwise distance and the variation in flow direction through the boundary layer near the trailing edge decrease abruptly as the tip is approached.

For two-dimensional turbulent boundary layers, a generally accepted near-wall similarity law is

$$\frac{u}{u_\tau} = \frac{1}{0.41} \ln\left(\frac{z u_\tau}{\nu}\right) + 5.0 \qquad (1)$$

where u_τ is the shear velocity, $\sqrt{\tau_w / \rho}$ (τ_w is the wall shear stress, ρ is the density, and ν is the kinematic viscosity). A limited range of values has been proposed for the constants in this equation; Pierce et al. (ref. 17) present a review of this situation. The incompressible law of the wall is usually extended to flows with moderate compressibility by evaluating the density and viscosity at the wall temperature. Prahlad (ref. 18) proposed that this similarity law be extended to three-dimensional flows by replacing the two-dimensional velocity in equation (1) with the velocity magnitude. Pierce et al. (ref. 17) reviewed a number of proposals, including Prahlad's, for near-wall similarity in three-dimensional turbulent boundary layers, using data which included direct measurement of the magnitude and direction of wall shear stress (ref. 19). They concluded that the magnitude of the wall shear stress could be determined by the Clauser chart technique (ref. 20) to within 5% to 10% if data in the range $10 \le z^+ \le 100$ ($z^+ = z u_\tau / \nu_w$) were used (ref. 21). This conclusion was limited to monotonically skewed boundary layers with an approximate maximum of 15° to 20° of skew.

Figure 13 illustrates the method by which the Clauser chart technique was applied to the present data. Velocity magnitudes obtained at $\eta = 0.165$, 0.450, and 0.950 are plotted in semilogarithmic coordinates. In these coordinates, equation (1) is represented by a family of straight lines with the skin friction coefficient, C_f, as a parameter. Since the straight lines in figure 13 were drawn for the range $10 \le z^+ \le 1000$, it is apparent that the sublayer and the inner portion of the logarithmic region are not resolved in these data. For this reason, most of the velocity magnitude profiles do not appear to approach zero with decreasing distance from the wall. In some cases in which a well-defined logarithmic region exists, the data obtained nearest the surface lie above the line corresponding to the law of the wall. This trend has been observed in airfoil boundary-layer measurements and is believed to be a surface proximity effect, probably also related to relative motion of the model and traversing unit. Note that the maximum skewing angles corresponding to many of the profiles of this investigation exceed the range of applicability of this method for estimating skin friction. Near the trailing edge at the mid-semispan stations, the difference in β between the boundary-layer edge and the surface sometimes exceeds 35°. For the more highly skewed profiles, it is likely that values of C_f estimated by this method represent the correct order of magnitude.

The behavior of the boundary-layer profiles obtained at the wing root, $\eta = 0.165$, is qualitatively different from that of the profiles at the other spanwise stations. Although these profiles do exhibit a logarithmic region near the surface, the slope is greater than that given by equation (1). The root-station boundary-layer profiles obtained at each of the three test conditions exhibited this feature.

Integral Properties, Skin Friction, and Edge Flow Angle Data at the Subsonic Test Condition

Values of streamwise displacement thickness, δ_1^*, for all profiles obtained at the subsonic test condition are presented in figure 14, normalized by the mean aerodynamic chord. The streamwise and crossflow displacement thicknesses, δ_1^* and δ_2^*, respectively, are defined as follows:

$$\delta_1^* = \int_0^\delta \left(1 - \frac{\rho u_s}{\rho_e u_e}\right) dz \tag{2}$$

and

$$\delta_2^* = -\int_0^\delta \frac{\rho w}{\rho_e u_e} dz \tag{3}$$

where the subscript e refers to conditions at the edge of the boundary layer, and the velocity components w and u_s are normal and parallel, respectively, to the flow direction at the boundary-layer edge. To facilitate presentation of the displacement-thickness data, the wing planform in figure 14 has been drawn to conform to the convention of left-to-right flow, resulting in a left-wing configuration. (Recall that the model is actually a right-wing configuration; see fig. 1.) Agreement between data sets obtained at the same location with different probes is generally good. The increase in δ_1^* with x/c is moderate near the trailing edge at the root station, but the larger values of c_ℓ in the mid-semispan region cause increased chordwise growth of δ_1^* with increasing x/c. This trend reverses near the tip, as a result of reduced tip loading. The trailing-edge streamwise displacement thickness normalized by the local chord varies by nearly a factor of two from mid-semispan to tip. Values of δ_1^* are more scattered near the tip than similar data obtained further inboard, probably because of vibration, since the boundary layer was thinnest at the tip where the relative motion was greatest.

The streamwise displacement-thickness data are presented in a more conventional format in figure 15, normalized by the local chord.

Values of the streamwise shape factor, H, are presented in figure 16. These data show the expected increase near the trailing edge at mid-semispan and have nearly constant values at the root and tip.

Values of skin friction obtained from the Clauser charts are presented in figure 17. The data show little variation at the root and have monotonically decreasing values of C_f with increasing x/c at the other spanwise stations. Data sets obtained with different probes at the same location are in good agreement with each other. The trends in the skin-friction data are consistent with trends observed in the δ_1^* and H plots.

Flow-direction measurements at the boundary-layer edge are presented in figure 18. Although all the previous comparisons show significant differences between trends observed at the wing root and at the other spanwise stations, the flow-direction results are the most dramatic in this respect. Additional data are needed for the transition region between the root and the mid-semispan stations.

The crossflow displacement thickness, δ_2^*, is probably the most clear-cut indicator of three-dimensionality. Distributions of crossflow displacement thickness are presented in figure 19. The trends in these data are consistent with the velocity magnitude and flow-direction profiles of figure 12; the most significant crossflow effects are present at mid-semispan, aft of mid-chord.

Boundary-Layer Profiles at the Transonic Test Conditions

Velocity magnitude and flow-direction profiles obtained at the transonic cruise condition $M_\infty = 0.825$, $\alpha = 4°$ are presented in figure 20. These data show most of the same qualitative features as the data obtained at the subsonic test condition, and also show the influence of the shock wave. At the root station (fig. 20a) the shock location indicated by the C_p distribution (fig. 7) is in the range $0.35 < x/c < 0.55$, and the flow inclination in the inner portion of the boundary layer is apparently influenced by the shock. The profile at $x/c = 0.4$ is aligned with the free-stream direction, except for a thin layer near the surface where the flow turns inboard. At $x/c = 0.5$ and 0.6, the flow direction is slightly inboard at the boundary-layer edge, turning continuously outboard with decreasing distance from the wall.

The data of figure 20b, obtained at $\eta = 0.300$, are typical of the mid-semispan stations. As in the subsonic test condition, these data show significant differences from data obtained at the root station. The flow direction at the boundary-layer edge is approximately 16° inboard at $x/c = 0.2$. The influence of the shock on the flow within the boundary layer is qualitatively similar to the trend observed at the wing root. At $x/c = 0.2$, upstream of the shock, the flow direction becomes increasingly inboard as the surface is approached; this trend is reversed at $x/c = 0.4$, downstream of the shock. All of the profiles obtained downstream of the shock at this spanwise station show the flow direction changing from slightly inboard at the edge to outboard near the surface. Velocity magnitude data sets obtained with different probes at the same chordwise station are in good agreement. The flow-direction profiles obtained with probes 1 and 2, $0.2 \le x/c \le 0.5$, are also in good agreement, but the agreement between profiles obtained with probes 1 and 3, $x/c \ge 0.5$, is poorer, as it is for the corresponding profiles at the subsonic test condition (fig. 12b). The data obtained with probe 3 for $x/c \ge 0.98$, $z/c < 0.003$ exceed the calibration range and have been omitted. The large angles indicated near the surface by probe 3 appear questionable, but no valid reason to discard these data has been identified.

Data obtained at the next outboard station, $\eta = 0.450$, are presented in figure 20c. Data sets obtained with probes 1 and 2 are in good agreement except in the vicinity of the shock, where the scatter is attributed to low-frequency shock-wave motion and the lack of repeatability to a shift in mean shock location.

Data obtained at $\eta = 0.575$ (fig. 20d) are qualitatively similar to the data shown in figures 20b and 20c, except for the substantial lack of repeatability at $x/c = 0.3$; where two different profiles were obtained consecutively, with the same probe. Examination of the profile data and the

displacement-thickness data indicates that the mean shock location may have shifted during the time between the acquisition of the two profiles.

The reduction in section lift coefficient with increasing η near the tip is evident in the boundary-layer data obtained at the more outboard stations (figs. 20e-20i). The growth in boundary-layer thickness with increasing chordwise distance, and the variation in flow direction through the boundary layer near the trailing edge, decrease abruptly as the tip is approached. Anomalies in the velocity magnitude data near the surface at the outboard stations are believed to be associated with relative motion of the model and traversing unit.

Velocity magnitude and flow-direction profiles obtained at $M_\infty = 0.825$, $\alpha = 6°$ are presented in figure 21. The data obtained at the root station (fig. 21a) are similar in character to the root-station data obtained at the transonic cruise condition (fig. 20a), except that the influence of the shock on the flow-direction profiles is more pronounced. At $\eta = 0.300$ (fig. 21b), relatively large values of velocity at the boundary-layer edge upstream of the shock are evident ($u_e/u_\infty = 1.73$ at $x/c = 0.20$), and large outboard components of velocity are present in the flow-direction profile at $x/c = 0.4$. At $\eta = 0.450$ (fig. 21c), the flow is attached at $x/c = 0.3$. The flow is probably intermittently separated at $x/c = 0.4$, and is clearly separated at $x/c = 0.5$ and 0.6. There is considerable scatter caused by unsteadiness in the profiles at $0.4 \le x/c \le 0.6$, but the data give an approximate indication of the extent of the viscous region. At $\eta = 0.575$ and 0.650 (figs. 21d, 21e), the flow appears to separate in the vicinity of $x/c = 0.4$, but the viscous region is thinner at mid-chord at $\eta = 0.650$. The trend toward increasingly positive values of trailing-edge C_p in the static-pressure distribution for this test condition (fig. 10) indicates that the flow was attached for $\eta \ge 0.80$.

Clauser plots of velocity magnitude profiles for three spanwise stations at the transonic cruise condition are presented in figure 22. These data are qualitatively similar to the corresponding data obtained at the subsonic test condition (fig. 13).

Integral Properties, Skin Friction, and Edge Flow Angle Data at the Transonic Test Conditions

Values of streamwise displacement thickness, δ_1^*, for all profiles obtained at the transonic test conditions are presented in figures 23 and 24. Although it was not possible to obtain many profiles that were clearly upstream of the influence of the shock, the increase in δ_1^* associated with the shock is apparent at the inboard stations. There is generally good agreement between data sets obtained at the same location with different probes; however, a lack of repeatability in the vicinity of the shock at $\eta = 0.450$ and 0.575 is evident. In the most extreme cases—$\eta = 0.450$, $x/c = 0.5$, and $\eta = 0.575$, $x/c = 0.3$—the large value of δ_1^* is consistent with values measured further downstream of the shock, and the smaller value appears to be a continuation of the upstream trend, indicating that a shift in mean shock location may have occurred during the time between the acquisition of the two profiles. The trends of spanwise variation in displacement thickness at this test condition are similar to the trends exhibited by the corresponding data for the subsonic test condition (figs. 14, 15).

Also included in figure 23 are data obtained at the two inboard stations at $M_\infty = 0.825$, $\alpha = 6°$. The displacement-thickness distributions at the root station, $\eta = 0.165$, are nearly identical. At the next outboard station, $\eta = 0.300$, a greater increase in displacement thickness at the shock is shown by the data for $\alpha = 6°$, but the distributions are similar near the trailing edge. Data obtained further

outboard at $\alpha = 6°$ show extensive separation aft of mid-chord (see fig. 21). The comparison of data from these two test conditions at $M_\infty = 0.825$ implies that boundary-layer characteristics at mid-semispan are determined primarily by local pressure gradients and are not influenced significantly by flow at the root or by the tunnel-wall boundary layer.

Values of streamwise shape factor and skin friction are presented in figures 25 and 26 for $M_\infty = 0.825$, $\alpha = 4°$. The influence of the shock is even more pronounced in these data than in the plots of δ_1^*. Large values of H occur in the vicinity of the shock, followed by decreases with increasing x/c as the boundary layer recovers from the interaction. The subsequent increases in H at mid-semispan near the trailing edge are moderate. Both the C_f and H data indicate that the trailing edge is not in a state of incipient separation.

Measurements of flow direction at the boundary-layer edge and of crossflow displacement thickness are presented in figures 27 and 28 for the transonic cruise condition. These data show the same characteristics as the corresponding data obtained at the subsonic test condition.

Integral-property, skin-friction, and edge flow angle data for the $M_\infty = 0.825$, $\alpha = 6°$ case are presented in figures 29-33. Characteristics of the streamwise displacement-thickness data at the two inboard stations were discussed previously. Values of C_f are presented for those profiles which exhibit a logarithmic region near the surface; integral properties are presented for those profiles which were judged to be attached or in a state of incipient separation, and edge flow angle data are presented for all profiles obtained at this test condition.

The influence of the shock wave at $\eta = 0.300$ is particularly evident in the distributions of shape factor and skin friction. The greater chordwise extent of nonzero values of skin friction at $\eta = 0.650$ than at $\eta = 0.450$ and 0.575 is consistent with the static-pressure data obtained at this test condition, indicating a trend toward attached flow at the outboard spanwise stations. The distributions of β_c at the two inboard stations (fig. 32) are similar to those observed at other test conditions.

Flow Unsteadiness

As noted earlier, flow unsteadiness was evident throughout the series of experiments. It is important, therefore, to consider the unsteady aspects of the flow when evaluating the boundary-layer data. The array of pressure transducers in the wing provided an overall picture of the unsteady pressure field on the wing upper surface. In coefficient form, the pressure fluctuation intensities at $M_\infty = 0.825$, $\alpha = 4°$ are shown in figure 34. A "baseline" $C_{p_{rms}}$ level, corresponding to a case of no net loading on the wing, is also indicated. The features are characteristic of attached transonic flow; relatively low fluctuation intensities are present up- and downstream of the shock, which produces intense pressure fluctuations as it "jiggles" chordwise. The shaded region indicates the chordwise extent of the overall shock pressure rise according to the section C_p distributions; this rise corresponds approximately to the range of unsteady shock movement. The pressure fluctuation intensity appears to be unusually high, especially upstream of the shock, where previous experiments in wind tunnels (refs. 22 and 23) and in flight (ref. 24) have indicated $C_{p_{rms}} \approx 0.01$ or less.

A further indication of the extent of unsteady chordwise shock movement on the model wing is given in figure 35, which shows an oscillograph record of simultaneous pressure signals from

$x/c = 0.25$ and $x/c = 0.40$, $\eta = 0.420$ for the transonic test condition. Passage of the shock back and forth over the transducer at 40% chord produces the large pressure jumps. Although the shock is completely downstream of the 40% chord station during some periods (the steady, low-pressure portions of the signal), it occasionally moves sufficiently far forward to produce positive-pressure jumps in the output of the transducer at 25% chord. This range of unsteady shock motion was unusually extensive, particularly for a conventional airfoil section with fully attached flow. Earlier experience with two-dimensional airfoil models had indicated unsteady shock movement over only a few percent of the chord.

Another important aspect of figure 35 is the indication that unsteady shock motion occurs with a wide range of time scales, from a few milliseconds to the order of seconds. The response characteristics of the pressure-measuring systems used to take wing C_p and boundary-layer profile data were such that the pressure variations produced by the lowest frequency shock movements were detected while the higher frequency fluctuations were attenuated, so that only the average value of the pressure was recorded. The low-frequency response is illustrated by figure 36, which presents the envelope of C_p values obtained from a number of sequential data-acquisition cycles at spanwise station $\eta = 0.45$ for a constant flow condition; these data imply that the shock moved through a range of about 20% chord to nearly 50% chord. The one set of individually plotted data points shows an obvious case of the shock shifting position during the time taken by the data system to record the pressures at two adjacent chordwise stations. Although the recorded Mach number varied between 0.820 and 0.826 over these sets of C_p data, no correlation existed between the indicated Mach number and the shock position variations, nor was the recorded Mach number variation correlated with section c_ℓ variation (which amounted to 8%).

The pressure-measurement, frequency-response problem produces uncertainty in the boundary-layer measurements in the vicinity of the shock. The irregularity of some of the boundary-layer profiles near the shock was a direct result of low-frequency shock motion past the boundary-layer probe. Another important point is that an "averaged" boundary-layer profile measured in the immediate vicinity of an unsteadily moving shock is not likely to be a physically real profile. A velocity profile measured directly beneath the mean position of the shock is actually an average of the upstream profile and the downstream profile, both of which the probe sees as the shock moves back and forth; this "averaged" profile is different from the profile that actually exists beneath a stationary shock.

The lowest frequencies associated with the shock motion correspond to disturbance scales too large to be characteristic of the model flow field, and are apparently produced by disturbances in the tunnel flow. During continuous monitoring of the boundary-layer probe output while the tests were under way, very low frequency oscillations (< 1 Hz) were occasionally observed. Such low frequencies are generally ignored in studies of wind tunnel flow quality and background disturbance level. For example, the study of flow disturbances in various NASA Ames tunnels by Dods and Hanly (ref. 25) considered only frequencies above 10 Hz. However, evidence does exist that large-scale, long-period disturbances are present in transonic wind tunnel flows. Rose (ref. 26) observed flow disturbances in the Ames 14-foot tunnel (the tunnel used for these tests) that had streamwise length scales of at least 50 m; in the present case, this would translate into a time period of over 200 ms. Another indication comes from a static-pressure probe used in the present tests to monitor

test-section pressure fluctuations. Data from this probe indicate considerable energy in the low-frequency end of the spectrum (below 10 Hz), as figure 37 shows.

A further example of the influence of low-frequency disturbances appears in figure 38, which shows low-frequency-filtered (1-Hz cutoff) pressure fluctuations measured at 25% chord for two different span stations at a subsonic test condition ($M_\infty = 0.499$, $\alpha = 5.0°$) that was free of shock or separation unsteadiness. Negative as well as positive correlations are apparent. (Negative correlations are defined by similar time dependence but opposite signs.) Because slow variation of the test-section static pressure affects all wing static pressures similarly, static pressure changes alone cannot explain the periods of negative correlation. Since flow velocity variations affect wing pressures in two ways, either by varying the Mach number (streamwise velocity variation) or by varying the angle of attack (velocity variation perpendicular to the mean stream direction), $\partial C_p / \partial M$ and $\partial C_p / \partial \alpha$ were evaluated at the wing stations in question (x/c = 0.25 at $\eta = 0.420$ and 0.640) to define the local pressure responses at those stations to flow velocity in general. It was found that $\partial C_p / \partial M > 0$ and $\partial C_p / \partial \alpha < 0$ at both stations, meaning that a large-scale flow-velocity perturbation would produce pressure variations of the same sign at both stations. To produce the occasional negative C_p correlation, some flow disturbances must have included large-scale velocity variations that changed sign between $\eta = 0.420$ and $\eta = 0.640$, suggesting that large-scale swirling motions were present in the tunnel flow.

COMPARISONS AMONG MEASURED AND COMPUTED BOUNDARY-LAYER PROPERTIES

Measured and computed flow-field properties will be compared at two spanwise locations, one at mid-semispan and another near the tip (fig. 39). The experimental data will be compared with the predictions of two- and three-dimensional computational methods for $\eta = 0.450$ and $\eta = 0.900$. However, comparisons involving computations with an infinite-swept-wing boundary-layer code use sections normal to the quarter-chord line and their corresponding intersections with the quarter-chord line, at $\eta = 0.554$ and $\eta = 0.870$.

Results at Mach 0.50

Surface static-pressure distributions obtained at $M_\infty = 0.50$ at the spanwise stations chosen for the comparisons are shown in figure 40. The experimental values of the section lift coefficient, c_ℓ, are also included. Conditions at $\eta = 0.450$ are representative of the relatively highly loaded mid-semispan region, and conditions at $\eta = 0.900$ are typical of the more lightly loaded tip region.

Static-pressure distributions calculated by two of the Jameson-Caughey FLO-codes (refs. 27 and 28) are included for comparison. Both codes are based on the transonic full potential equation. FLO-30 is a wing-body code in which a finite-volume scheme in conservative form is used; the results presented do not include a boundary-layer correction. FLO-22NM is a finite-difference, nonconservative, wing-alone code coupled by Henne et al. (ref. 29) with the two-dimensional Nash-Macdonald integral turbulent boundary-layer method (ref. 30). It also includes an adjustment to M_∞ to correct for the influence of the fuselage on the wing flow field. Both FLO codes have been used

extensively for several years; their strengths and weaknesses are well known. Results of the inviscid calculations are incidental to comparisons between computed and experimental viscous flow properties. Agreement between the measured and calculated pressure distributions is generally good at $\eta = 0.900$ and somewhat poorer at $\eta = 0.450$. The calculated results are nearly identical except near the trailing edge, where the effect of including the boundary layer in FLO-22NM is evident. A comparison between the inviscid FLO-30 result and the experimental data shows the trend, commonly observed in the trailing-edge region, of calculated static-pressure levels that are higher than those experimentally observed. The boundary-layer correction in FLO-22NM brings the calculated pressures closer to the experimental values, although the increment is too small at the inboard station. The excellent agreement between the two calculated results at the more forward chordwise locations indicates that the correction for fuselage effects in FLO-22NM is adequate for this situation.

Measured and computed upper-surface boundary-layer displacement-thickness distributions are compared in figure 41 for the subsonic case. The computations are two-dimensional. The FLO-22NM results correspond to the computed static-pressure distributions of figure 40, and the remaining computations were performed using the experimental static-pressure distributions. Agreement is generally good at $\eta = 0.900$, but the computed displacement thicknesses are less than the measured values at $\eta = 0.450$.

There are significant differences between the predictions of FLO-22NM and the Cebeci-Smith finite-difference method (ref. 31) in the leading-edge region. In the FLO-22NM calculation, the values of streamwise distance from the leading edge to the transition location normalized by the local chord, $(x/c)_t$, were 0.008 and 0.013 at $\eta = 0.450$ and 0.900, respectively. The Nash-Macdonald computations (ref. 30), based on the experimental pressures, started downstream of the transition location predicted by the Cebeci-Smith method, and used initial conditions derived from the Cebeci-Smith method. Although the instantaneous transition option was used in the Cebeci-Smith code, the boundary-layer profiles computed by this code required two to three mesh points to change from laminar to turbulent characteristics. The beginning of transition for these test conditions was predicted by the Cebeci-Smith code to be $(x/c)_t = 0.025$ and 0.05 at $\eta = 0.450$ and 0.900, respectively. These locations correspond to points just downstream of the suction peaks in the local pressure distributions. At $\eta = 0.900$, the experimental and computed static-pressure distributions are nearly identical; the differences between the two sets of Nash-Macdonald calculations are clearly associated with differences in transition locations. At $\eta = 0.450$ the situation is less clear, but comparisons of both sets of Nash-Macdonald calculations implies that the primary cause of differences in the calculated distributions at $\eta = 0.45$ and $x/c < 0.7$ is the difference in transition location; for $x/c > 0.7$, differences in the static-pressure distributions near the trailing edge are clearly important. Since the trailing-edge static-pressure distribution resulting from the FLO-22NM calculation at $\eta = 0.450$ is not in agreement with the measurements, the better agreement of the FLO-22NM displacement-thickness distribution with the experimental results, relative to the computations based on the experimental pressures, is fortuitous. Improved agreement of experimental and computed trailing-edge static-pressure distributions would be associated with poorer agreement of the displacement-thickness distributions, and vice versa.

Computed displacement-thickness distributions using the FLO-30 pressure distribution shown in figure 40 are compared with the same experimental data in figure 42. Computed results are included from the three-dimensional integral method of Smith (ref. 32) and the Cebeci-Smith

two-dimensional finite-difference method. Agreement between measurements and computed results is closer for $\eta = 0.900$ than for $\eta = 0.450$, and the three-dimensional predictions are closer to the data than the two-dimensional predictions at both spanwise locations. The FLO-30 code and the three-dimensional boundary-layer code used for these calculations are part of a coupled viscous-inviscid interaction scheme (ref. 33). It has not yet been possible to achieve a solution with this coupled scheme beyond the initial inviscid and boundary-layer calculations. This inability to achieve a viscous-inviscid solution is surprising, since wings having little aft camber, such as the wing used in the present study, usually present fewer difficulties for computation methods than more recent designs having significant aft camber.

Experimental data, the predictions of a three-dimensional finite-difference method, and the predictions of an infinite-swept-wing method developed by Cebeci and his coworkers (refs. 34 and 35) are compared in figure 43. Experimental static-pressure distributions were used in these computations. For the three-dimensional computations, starting conditions along the span at $x/c = 0.2$ were obtained from experimental data, and starting conditions at the wing root were obtained from results generated internally by the code at $\eta = 0.300$.

For the infinite-swept-wing computations, airfoil-section data were obtained in planes normal to the quarter-chord line (see figure 39). Static-pressure distributions were interpolated to these planes normal to the quarter-chord lines from the adjacent pressure-orifice stations.

Experimental values of δ_1^* at $\eta = 0.450, 0.575, 0.800$, and 0.900 are included in figure 43. Results from the three-dimensional computations correspond to $\eta = 0.450$ and 0.900, but results from the infinite-swept-wing computations correspond to diagonal sections between the two pairs of adjacent stations. Substantially better agreement between measurements and results of calculations is again shown in the tip region. The three-dimensional computations of δ_1^* agree, within plotting accuracy, with the infinite-swept-wing values calculated with a quarter-chord sweep angle of $\Lambda = 35°$; the solid line in figure 43 represents both calculations. Reducing the sweep angle in the infinite-swept-wing calculation to the trailing-edge value of 25° produces a moderate reduction in the predicted displacement-thickness distribution near the trailing edge.

In figure 44, the experimental spanwise variation of displacement thickness is compared with the results of three-dimensional computations by the method of reference 34. Starting conditions at the wing root were obtained both from results generated internally by the code and from boundary-layer measurements at $\eta = 0.300$. The two sets of starting conditions agree at the forward chordwise stations, but differ substantially near the trailing edge. The results of the computation that started with experimental data rapidly approach the computed results that started with the internally generated solution; the span station at which the results of the two computations agree depends on the magnitude of the initial discrepancy. It is clear that the discrepancies between measured and computed displacement-thickness distributions near the trailing edge in the mid-semispan region are not a result of inaccurate inboard starting conditions for the code, because the predictions of the code rapidly adjust to the same values with increasing η for both computations.

Computational and experimental values of β_c and δ_2^* are compared in figures 45 and 46, respectively. Since β_c is a property of the inviscid flow, and is a boundary condition for the viscous flow in a conventional boundary-layer calculation, figure 45 gives an indication of the degree to

which the inviscid and viscous regions are consistent. In the three-dimensional calculations, the local yaw-plane angles at the edge of the boundary layer are closely matched to the experimental values. In the infinite-swept-wing calculations, the component of velocity along the span is fixed and the velocity magnitude is controlled by the local static pressure, so that the computed local yaw-plane angle is a function of the assumed effective sweep angle and the pressure distribution. The directions of boundary-layer edge flow predicted by the infinite-swept-wing calculations are considerably more outboard at the mid-semispan station than the measured values; this discrepancy is qualitatively similar but smaller in magnitude near the tip. The differences among the yaw-plane angles predicted by the infinite-swept-wing calculation and the measured values are indications of the degree to which the the infinite-swept-wing approximation is valid for this flow field.

The crossflow displacement thicknesses are small at the outboard station, and the measured and predicted values are roughly similar. At the inboard station, the measured values exceed the computed values near the trailing edge, and the three-dimensional calculation predicts less crossflow than either of the infinite-swept-wing calculations. Differences in the boundary-layer edge conditions may be responsible for most of the differences among the computations. Variation of the assumed sweep angle has a first-order influence on the computed crossflow at both spanwise stations.

Measured and computed values of local skin-friction magnitudes at the subsonic test condition are compared in figure 47. The computed values were obtained from the three-dimensional calculations. Agreement is generally good, with the largest discrepancies occurring inboard, near the trailing edge.

Results at Mach 0.825

Two-dimensional boundary-layer computations were performed using the experimental pressure distributions obtained at selected spanwise stations at $M_\infty = 0.825$, $\alpha = 4°$. The computed displacement-thickness distributions are compared with experimental data in figure 48. Perturbations in the static-pressure distributions, caused by the auxiliary wing and traversing unit, have little effect on the computed displacement-thickness distributions, but the computed values are substantially less than the measured values for $\eta = 0.450$, aft of mid-chord. Since the measured static-pressure rise associated with the shock wave extends over a considerable chordwise distance, primarily because of shock motion caused by test-section flow unsteadiness, an additional calculation was performed for a pressure distribution in which the pressure rise caused by the shock was limited to a chordwise extent of approximately eight times the upstream boundary-layer thickness. The resulting chordwise extent of the interaction is in better agreement with shock/boundary-layer interaction experiments. This modification of the static-pressure distribution had little effect on the computed displacement-thickness distribution at the inboard station, as did the results of several other numerical experiments (not shown) on the influence of mesh spacing in the leading-edge region, the assumed length of the transition region, and the smoothing of the input static-pressure distribution. A more definitive evaluation of the effect of the auxiliary wing and traversing unit on the boundary-layer growth would be to perform three-dimensional boundary-layer calculations for edge conditions corresponding both to the wing alone and to the wing plus the auxiliary wing and traversing unit. The difficulty of performing three-dimensional boundary-layer calculations has precluded this approach.

The experimental static-pressure distributions obtained with the auxiliary wing and traversing unit are compared in figure 49 with results of calculations from the FLO-22NM and FLO-30 codes. The experimental data and the FLO-22NM results correspond to $\alpha = 4°$. The angle of attack for the FLO-30 computation was adjusted to achieve good agreement between the calculated and experimental values of upper-surface pressure distribution for $x/c < 0.5$, $\eta = 0.450$. The resulting angle of attack for the FLO-30 computation was 4.2°. The more aft location of the upper-surface shock at $\eta = 0.450$ obtained from the FLO-30 solution, relative to the FLO-22NM solution, is consistent with both the slightly higher angle of attack of the FLO-30 calculation and the conservative formulation of FLO-30. However, the upper-surface pressure distribution forward of the shock obtained from the FLO-22NM solution indicates that the angle of attack for this calculation may have been slightly low. Increasing the angle of attack for the FLO-22NM calculation would cause the C_p distribution forward of the shock to become more negative and to move the shock aft, thus improving the agreement with the experimental data and the FLO-30 solution. There is a degree of arbitrariness in the manner in which the Kutta condition and the trailing vortex sheet are treated in potential flow calculations which can lead to discrepancies between computed and measured angles of zero lift. The unusually small size of this model relative to the test-section size, and the slotted-wall test-section configuration, tends to rule out the possibility of significant wind tunnel wall-interference effects in the experiment.

The differences among the computed and the experimental pressure distributions near the trailing edge are similar to the results shown in figure 40 for $M_\infty = 0.50$; the computed static-pressure levels are higher than the measured values near the trailing edge, except for the FLO-22NM computations at $\eta = 0.900$. At $\eta = 0.900$, neither calculation satisfactorily models the shock and expansion on the upper surface for $x/c < 0.5$. These discrepancies may be the result of meshes which are too coarse.

Boundary-layer computations using the static-pressure distributions shown in figure 49 are compared with experimental data in figure 50. The transition locations were $(x/c)_t = 0.04$ for the three-dimensional integral method of Smith (ref. 32) at both spanwise stations, and $(x/c)_t = 0.022$ and 0.10 at $\eta = 0.450$ and 0.900, respectively, for FLO-22NM. The influence of the difference in shock location between the two computations is evident in the mid-chord displacement-thickness distributions at $\eta = 0.450$. The differences between the two calculated trailing-edge displacement-thickness distributions at $\eta = 0.450$ probably result from the significant differences in the corresponding static-pressure distributions near the trailing edge, but differences in strength and location of the shock may also be partly responsible. Separation is predicted in the three-dimensional calculation at $x/c = 0.97$, $\eta = 0.450$; downstream of separation, a constant shape factor is used to continue the calculation. The large differences between the computed displacement-thickness distributions at $\eta = 0.900$, $x/c > 0.7$ may be a result of the slightly greater overall pressure gradient in the FLO-30 pressure distribution, and the more aft location of transition in the FLO-22NM calculation.

Results of computations with the infinite-swept-wing code are compared with experimental data for streamwise and crossflow displacement-thickness distributions (figs. 51,52) and yaw-plane flow direction angles at the boundary-layer edge (fig. 53), for both the mid-semispan and tip stations. Computed results are included for assumed sweep angles of 25° and 35°, and for pressure distributions obtained with the wing alone and with the wing in the presence of the traversing unit. These results show a much greater sensitivity of the computed streamwise and crossflow displacement-thickness distributions to the assumed sweep angle than the corresponding results for $M_\infty = 0.50$,

presented in figures 43 and 45. Because the influence of the assumed sweep angle is so large and the computed inviscid yaw-plane flow-direction angles near the trailing edge are in poor agreement with the experimental values, the geometry of this wing is such that the infinite-swept-wing approximation is inadequate.

CONCLUDING REMARKS

Boundary-layer survey data were obtained over most of the upper surface of a transport wing model at subsonic and transonic cruise conditions. A less extensive set of data was also obtained at a transonic test condition for which a separated region was present at mid-semispan, aft of mid-chord. The data were obtained with miniature three-orifice yaw probes that allowed determination of the flow speed and flow direction in the plane of the wing. In addition to the boundary-layer data, surface static-pressure distributions and fluorescent minituft flow-visualization photographs were obtained. Dynamic instrumentation, primarily high-frequency-response pressure transducers, were installed in the model; nonsteady data pertinent to interpretation of the boundary-layer results are presented.

Significant variation in flow direction with distance from the surface was observed near the trailing edge at both the subsonic and transonic cruise conditions, except at the wing root and tip. The transonic data show boundary-layer growth associated with shock-wave/boundary-layer interaction, followed by recovery of the boundary layer downstream of the shock.

Compromises in the design of the data acquisition equipment, related to flow interference and rigidity, were necessary to permit acquisition of an extensive set of data in a reasonable wind tunnel occupancy period. The influence of the traversing unit on the wing static-pressure distributions was negligible at the subsonic condition and moderate at the transonic conditions. Low-frequency test-section flow unsteadiness also had an adverse influence on this experiment. However, the internal consistency of the data, including generally good repeatability, indicates that the data should provide useful test cases for three-dimensional, turbulent, boundary-layer computation methods.

The boundary-layer and surface static-pressure data are compared with computed predictions obtained from inviscid wing and wing/body codes based on the transonic full potential equation, and from two- and three-dimensional boundary-layer codes. Good agreement was generally obtained between measured and computed static-pressure distributions; the primary discrepancies occurred between experimental data and inviscid calculations in the trailing-edge region, and at the shock near the tip at the transonic test condition. Results of the inviscid computations and comparisons with experimental static-pressure distributions are incidental to the comparisons of computed and measured boundary-layer properties.

The boundary-layer computation methods used in this limited set of comparisons gave reasonable results in the outboard regions where three-dimensional effects are at a minimum and adverse pressure gradients are moderate. In the more highly loaded mid-semispan region near the trailing edge, displacement-thickness growth was significantly underpredicted, except when the unrealistically severe adverse pressure gradients associated with inviscid calculations were used to perform

the boundary-layer calculations. Questions associated with the experimental data imply a need for additional data to corroborate the present results.

APPENDIX

Tabulated static-pressure and boundary-layer profile data are contained on microfiche pages located in an envelope in the back cover of this report. The following is a list of these tables with brief descriptions of their contents.

Table A1. Run summary of wing static-pressure data for which boundary-layer surveys were obtained. This table contains a run summary of wing static-pressure data obtained at test conditions corresponding to the boundary-layer surveys. Data are presented corresponding to the wing alone, the wing plus the auxiliary wing, and the wing plus the auxiliary wing with the traversing unit mounted at a survey station, with the probe tip retracted. Definitions of terms used in the static-pressure tabulations are also included.

Table A2. Wing static-pressure data for which boundary-layer surveys were obtained. This table contains test-section conditions and wing surface-pressure coefficients as a function of percent local chord and fraction of semispan.

Table A3. Run summary of boundary-layer profile data. This table contains run numbers, edge conditions, integral properties, and skin friction coefficients for the boundary-layer surveys. Definitions of terminology used in this table are also included.

Table A4. Detailed profile data, $M_\infty = 0.50$, $\alpha = 6°$, probe 1. The terminology used in presenting the detailed profile data is defined at the beginning of this table.

Table A5. Detailed profile data, $M_\infty = 0.50$, $\alpha = 6°$, probes 2 and 3.

Table A6. Detailed profile data, $M_\infty = 0.825$, $\alpha = 4°$, probe 1.

Table A7. Detailed profile data, $M_\infty = 0.825$, $\alpha = 4°$, probes 2 and 3.

Table A8. Detailed profile data, $M_\infty = 0.825$, $\alpha = 6°$, probe 1.

REFERENCES

1. Nixon, D. ed: Transonic Aerodynamics. Progress in Astronautics and Aeronautics, vol. 81, AIAA, New York, 1982.

2. van den Berg, B.; Elsenaar, A.; Lindhout, J. P. F.; and Wesseling, P.: Measurements in an Incompressible Three-Dimensional Turbulent Boundary Layer Under Infinite Swept-Wing Conditions, and Comparison with Theory. J. Fluid Mech., vol. 70, part 1, 1975, pp. 127-148.

3. Seetharam, H. C.; Pfeiffer, N. J.; Ohmura, M.; and McLean, J. D.: Experimental and Theoretical Studies of Three-Dimensional Turbulent Boundary Layers on an Empennage of a Typical Transport Airplane. Proceedings of the 13th Congress of ICAS, 1982, pp. 784-795.

4. Lux, D. P.: In-Flight Three-Dimensional Boundary Layer and Wake Measurements from a Swept Supercritical Wing. NASA CP-2045, vol. 1, part 2, Mar. 1978, pp. 643-655.

5. Schmitt, V.; Destarac, D.; and Chaumet, B.: Viscous Effects on a Swept Wing in Transonic Flow. AIAA Paper No. 83-1804, July 1983.

6. Keener, Earl R.: Boundary-Layer Measurements on a Transonic Low-Aspect Ratio Wing. NASA TM-88214, 1986.

7. Spaid, Frank W.; and Roos, Frederick W.: An Experimental Study of the Turbulent Boundary Layer on a Transport Wing in Transonic Flow. AIAA Paper No. 83-1687, July 1983.

8. Spaid, Frank W.: Transonic Airfoil and Wing flow field Measurements. AIAA Paper No. 84-0100, Jan. 1984.

9. Spaid, Frank W.: Comparisons Among Measured and Computed Boundary-Layer Properties on a Transport Wing. AIAA Paper No. 87-2555-CP, Aug. 1987.

10. Haney, H. P.; Waggoner, E. G.; and Ballhaus, W. F.: Computational Transonic Wing Optimization and Wind Tunnel Test of a Semi-Span Wing Model. AIAA Paper No. 78-102, Jan. 1978.

11. Roos, F. W.; and Riddle, D. W.: Measurements of Surface-Pressure and Wake-Flow Fluctuations in the Flow Field of a Whitcomb Supercritical Airfoil. NASA TN D-8443, 1977.

12. Roos, F. W.: The Buffeting Pressure Field of a High-Aspect-Ratio Swept Wing. AIAA Paper No. 85-1609, July 1985.

13. Dudzinski, T. J.; and Krause, L. N.: Flow-Direction Measurement with Fixed-Position Probes. NASA TM X-1904, 1969.

14. Braslow, A. L.; Hicks, R. M.; and Harris, R. V., Jr.: Use of Grit-Type Boundary-Layer-Transition Trips on Wind-Tunnel Models. NASA TN D-3579, 1966.

15. Spaid, F. W.; and Stivers, L. S., Jr.: Supercritical Airfoil Boundary Layer Measurements. AIAA Paper No. 79-1501, July 1979.

16. Crowder, J. P.: Fluorescent Minitufts for Non-Intrusive Flow Visualization. McDonnell Douglas Corp., Long Beach, CA, MDC J7374, Feb. 1977.

17. Pierce, F. J.; McAllister, J. E.; and Tennant, M. H.: Near-Wall Similarity in Three-Dimensional Turbulent Boundary Layers, Part I: Model Review. Three-Dimensional Turbulent Shear Flows, The American Society of Mechanical Engineers, New York, 1982, pp. 85-95.

18. Prahlad, T. S.: Wall Similarity in Three-Dimensional Turbulent Boundary Layers. AIAA J., vol. 6, no. 9, Sept. 1968, pp. 1772-1774.

19. McAllister, J. E.; Pierce, F. J.; and Tennant, M. H.: Direct Force Wall Shear Measurements in Pressure-Driven Three-Dimensional Turbulent Boundary Layers. Three-Dimensional Turbulent Shear Flows, The American Society of Mechanical Engineers, New York, 1982, pp. 53-59.

20. Clauser, F. H.: Turbulent Boundary Layers in Adverse Pressure Gradients. J. Aeronaut. Sci., vol. 21, Feb. 1954, pp. 91-108.

21. Pierce, F. J.; McAllister, J. E.; and Tennant, M. H.: Near-Wall Similarity in Three-Dimensional Turbulent Boundary Layers, Part II: Pressure-Driven Flow Results. Three-Dimensional Turbulent Shear Flows, The American Society of Mechanical Engineers, New York, 1982, pp. 96-103.

22. Roos, F. W.: Some Features of the Unsteady Pressure Field in Transonic Airfoil Buffeting. J. Aircraft, vol. 17, Nov. 1980, pp. 781-788.

23. Coe, C. F.; Riddle, S. W.; and Hwang, C.: Separated-Flow Unsteady Pressures and Forces on Elastically Responding Structures. Unsteady Airloads in Separated and Transonic Flows, AGARD CP-226, 1977, pp. (2-1)-(2-25).

24. Coe, C. F.; and Riddle, D. W.: Pressure Fluctuations Associated with Buffeting. Symposium on Transonic Aircraft Technology, Air Force Flight Dynamics Laboratory Report AFFDL-TR-78-100, 1978, pp. 315-352.

25. Dods, J. B., Jr.; and Hanly, R. D.: Evaluation of Transonic and Supersonic Wind-Tunnel Background Noise and Effects of Surface Pressure Fluctuation Measurements. AIAA Paper No. 72-1004, 1972.

26. Rose, W. C.: Free-Stream Turbulence Measurements in the NASA-Ames 14- Foot Wind Tunnel. Rose Engineering and Research, REAR TR-79-1, 1979.

27. Jameson, A.; and Caughey, D. A.: Numerical Calculation of the Transonic Flow Past a Swept Wing. New York University ERDA Report C00 3077-140, 1977.

28. Caughey, D. A.; and Jameson, A.: Recent Progress in Finite Volume Calculations for Wing-Fuselage Combinations. AIAA Paper No. 79-1513, July 1979.

29. Henne, P. A.; Dahlin, J. A.; and Peavey, C. C.: Applied Computational Transonics—Capabilities and Limitations. Douglas Paper 7025, Transonic Perspective Symposium, NASA Ames Research Center, 18-20 Feb. 1981.

30. Nash, J. F.; and Macdonald, A. G. J.: The Calculation of Momentum Thickness in a Turbulent Boundary Layer at Mach Numbers up to Unity. British Aeronautical Research Council, C.P. No. 963, 1967.

31. Cebeci, T.; and Smith, A. M. O.: Analysis of Turbulent Boundary Layers. Academic Press, New York, 1974, p. 258.

32. Smith, P. D.: An Integral Prediction Method for Three-Dimensional Compressible Turbulent Boundary Layers. British Aeronautical Research Council, R. & M. No. 3739, 1974.

33. Melson, N. Duane; and Streett, C. L.: TAWFIVE: A Users' Guide. NASA TM-84619, 1983.

34. Cebeci, T.; Kaups, K.; and Ramsey, J. A.: A General Method for Calculating Three-Dimensional Compressible Laminar and Turbulent Boundary Layers on Arbitrary Wings. NASA CR-2777, 1977.

35. Cebeci, T.; Kaups, K.; Ramsey, J. A.; and Schimke, S. M.: A Two-Point Finite-Difference Boundary-Layer Method for Incompressible and Compressible Two-Dimensional and Axisymmetric Laminar and Turbulent Flows Including Infinite-Swept Wings. Douglas Aircraft Company Report, MDC J7986, 1978.

ORIGINAL PAGE
BLACK AND WHITE PHOTOGRAPH

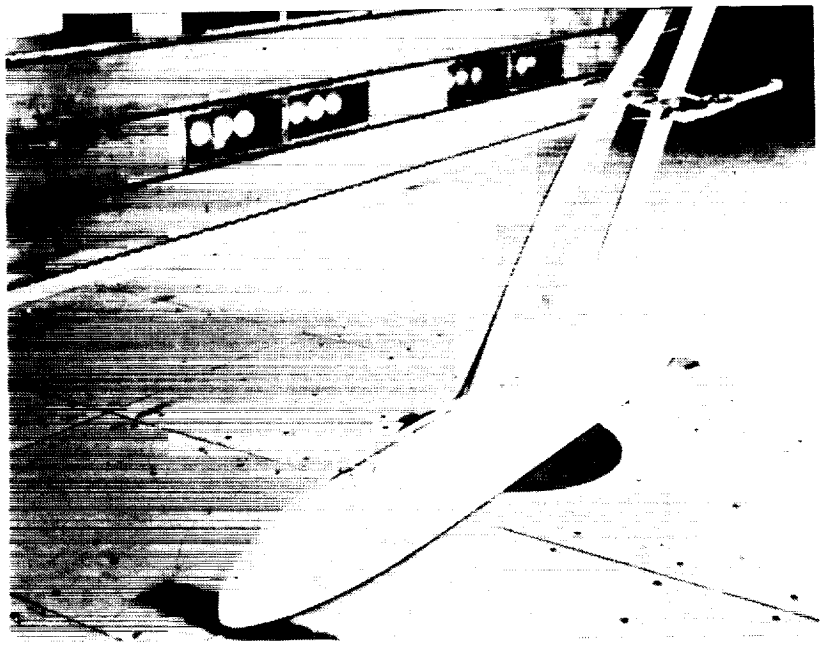

Figure 1. Transport wing-fuselage model with traversing unit in NASA Ames 14-Foot Transonic Wind Tunnel.

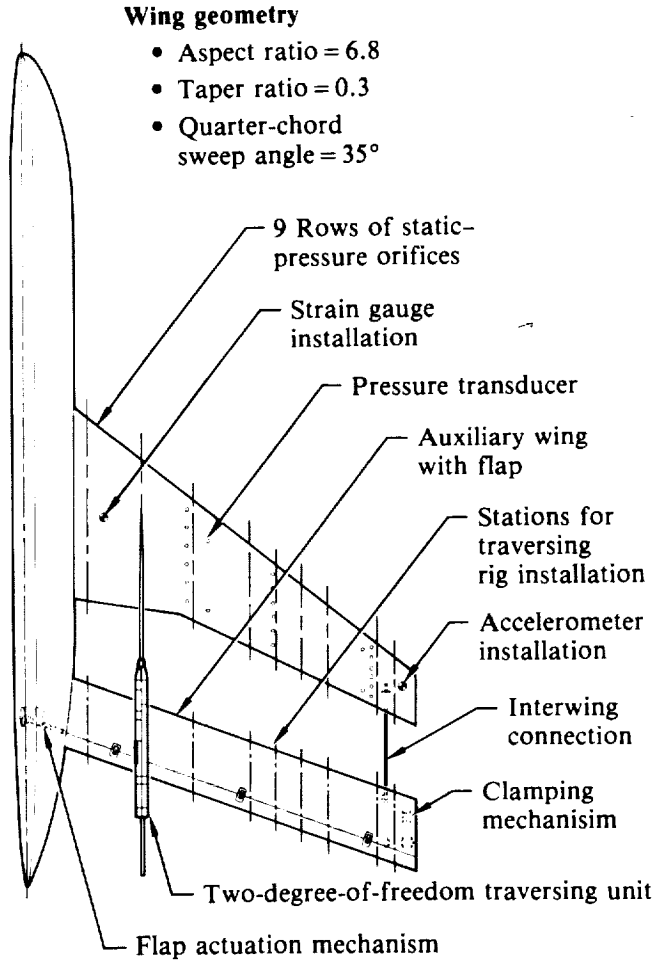

ORIGINAL PAGE IS
OF POOR QUALITY

Figure 2. Wing, fuselage, and boundary-layer traversing unit.

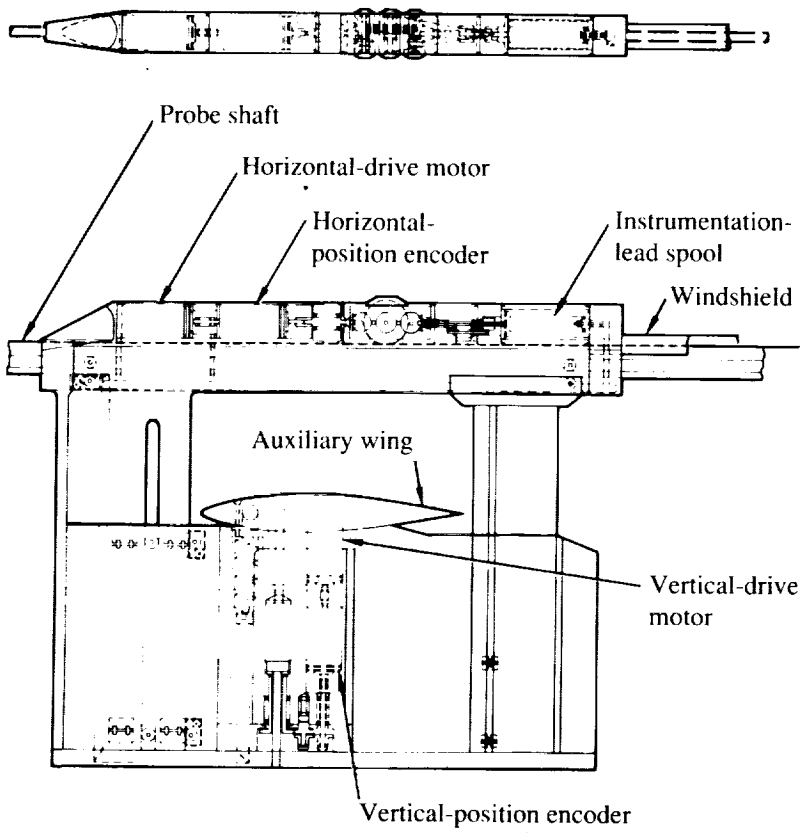

Figure 3. Details of traversing unit.

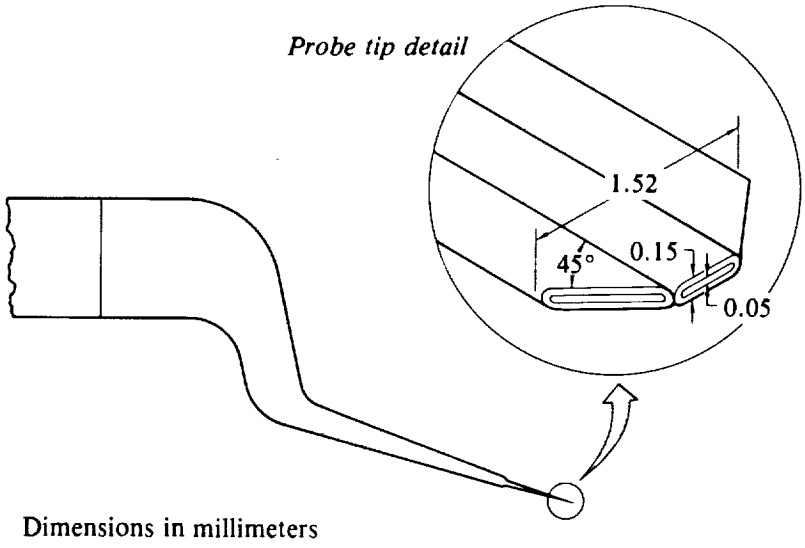

Figure 4. Probe geometry.

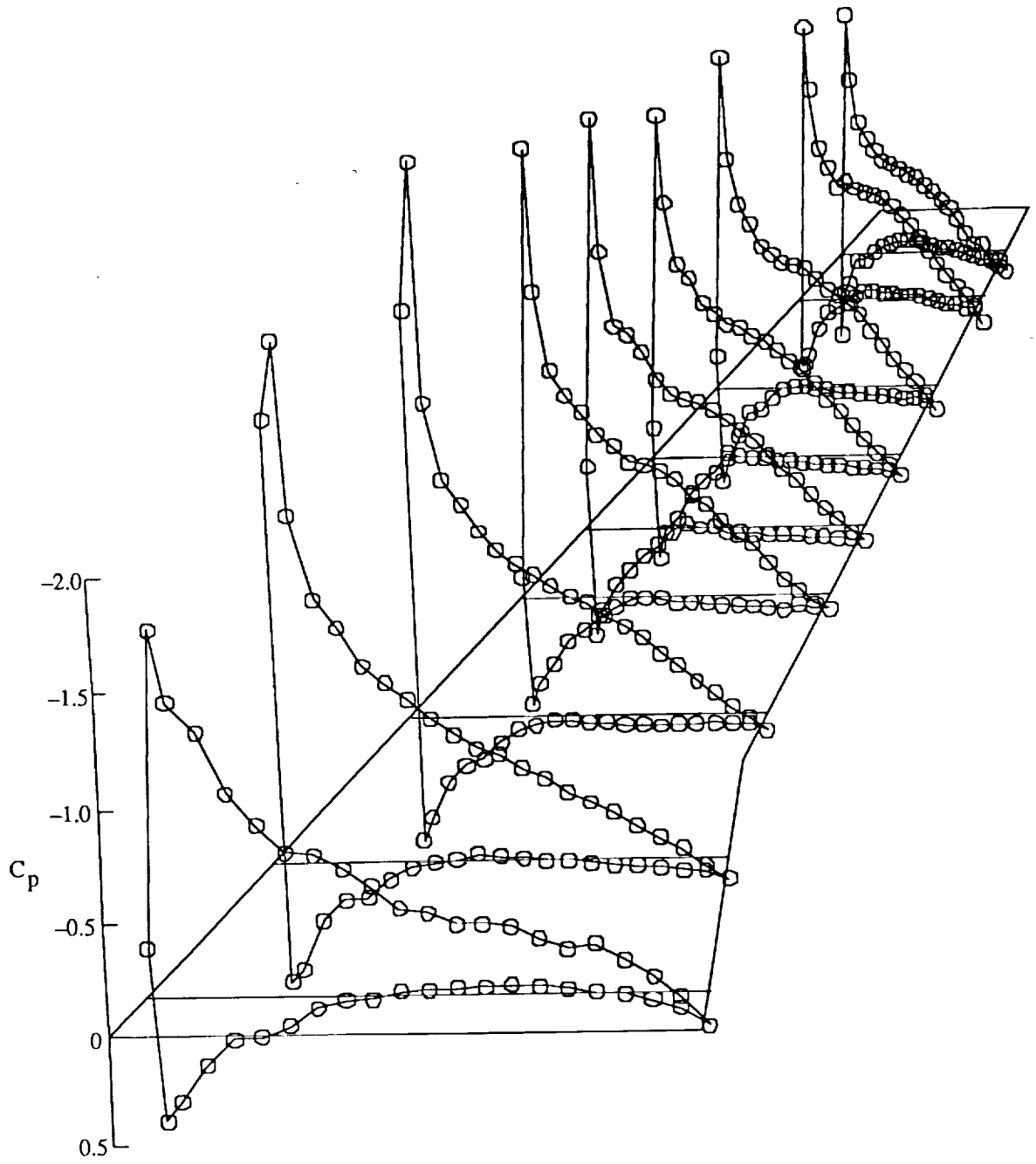

Figure 5. Wing static-pressure distributions; subsonic test condition, $M_\infty = 0.50$, $\alpha = 6°$.

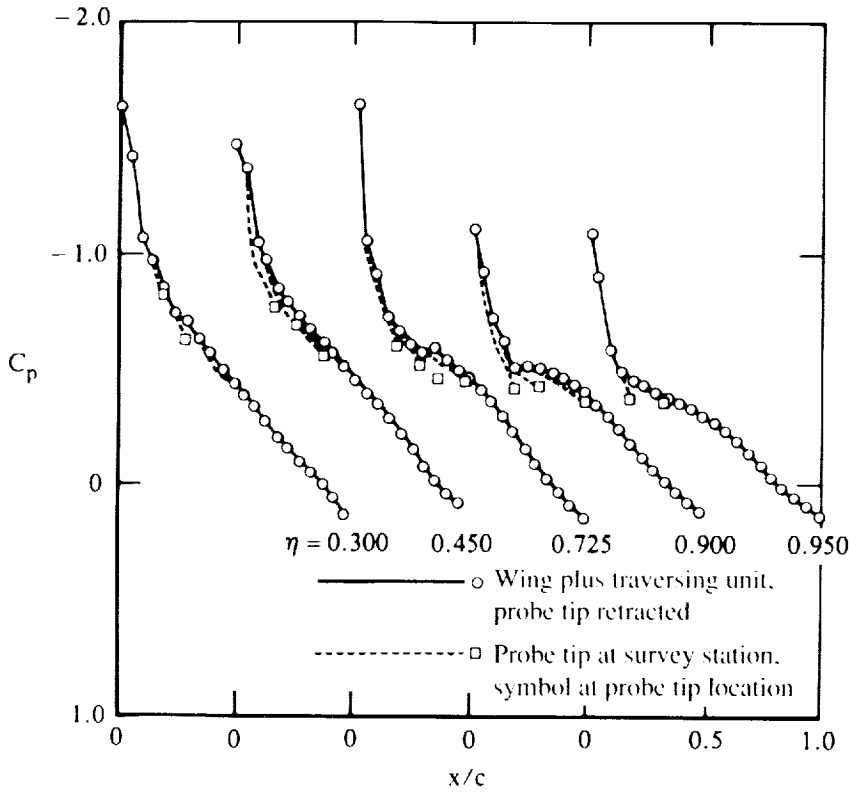

Figure 6. Effect of probe tip on wing static-pressure distributions upstream of survey station; $M_\infty = 0.50$, $\alpha = 6°$.

ORIGINAL PAGE IS
OF POOR QUALITY

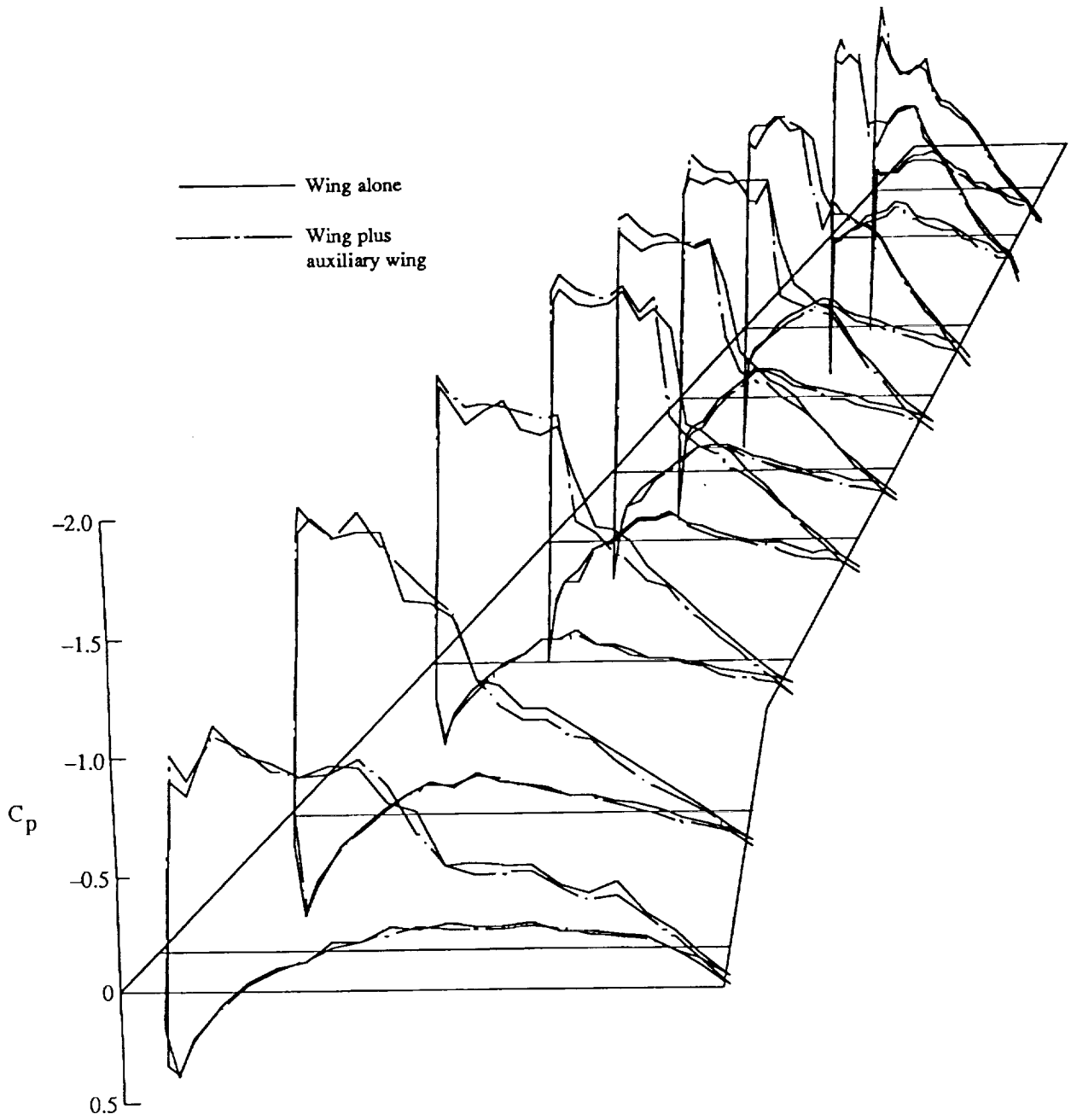

Figure 7. Wing static-pressure distributions; transonic test condition, $M_\infty = 0.825$, $\alpha = 4°$.

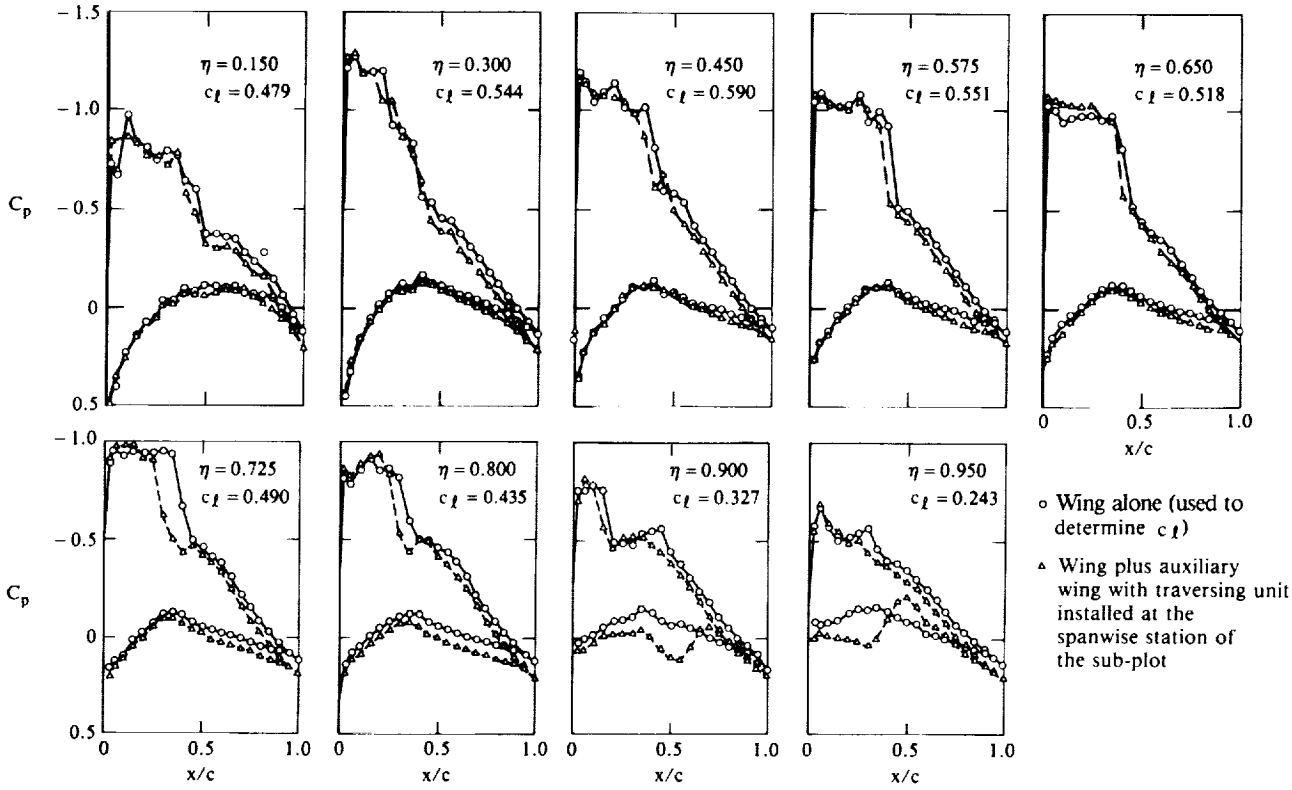

Figure 8. Effect of auxiliary wing and traversing unit on wing static-pressure distributions; $M_\infty = 0.825$, $\alpha = 4°$.

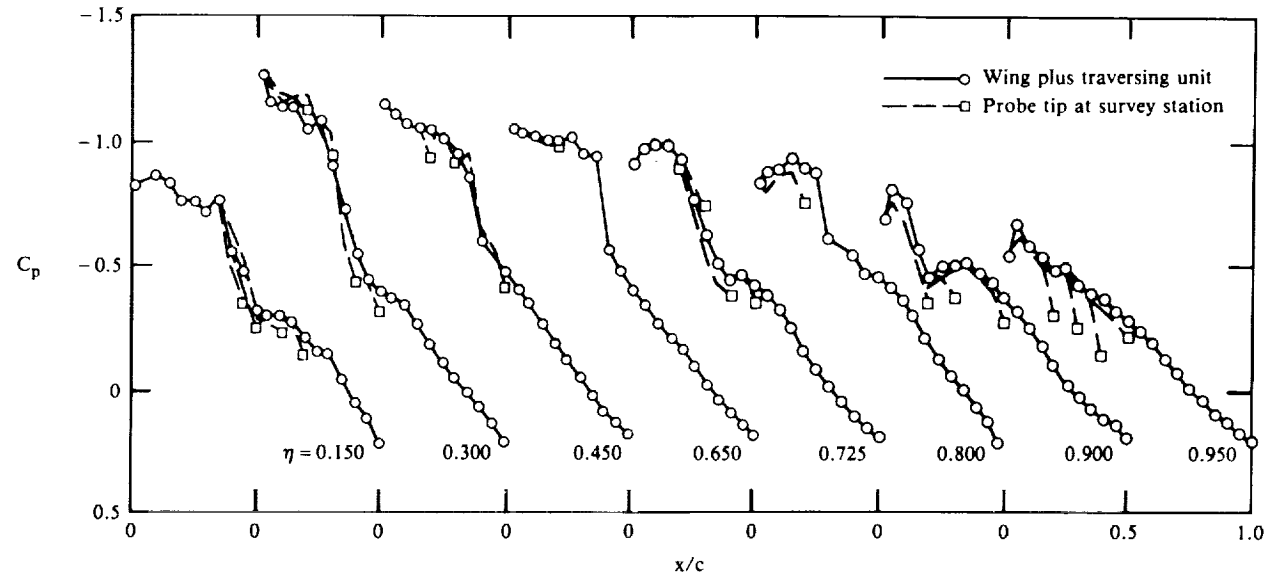

Figure 9. Effect of probe tip on static-pressure distributions upstream of the survey station; $M_\infty = 0.825$, $\alpha = 4°$.

ORIGINAL PAGE IS
OF POOR QUALITY

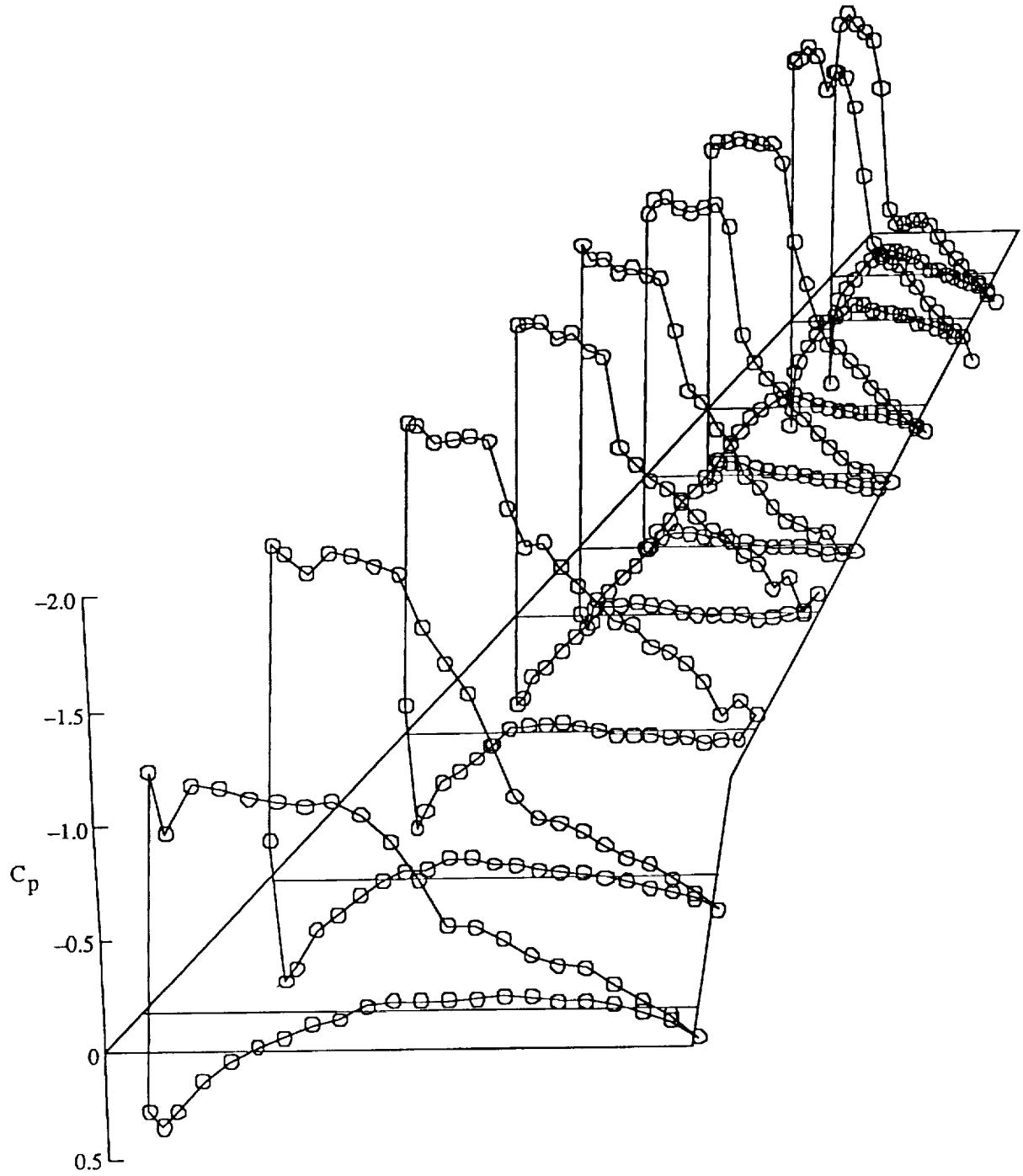

Figure 10. Wing static-pressure distributions including effect of auxiliary wing; $M_\infty = 0.825$, $\alpha = 6°$.

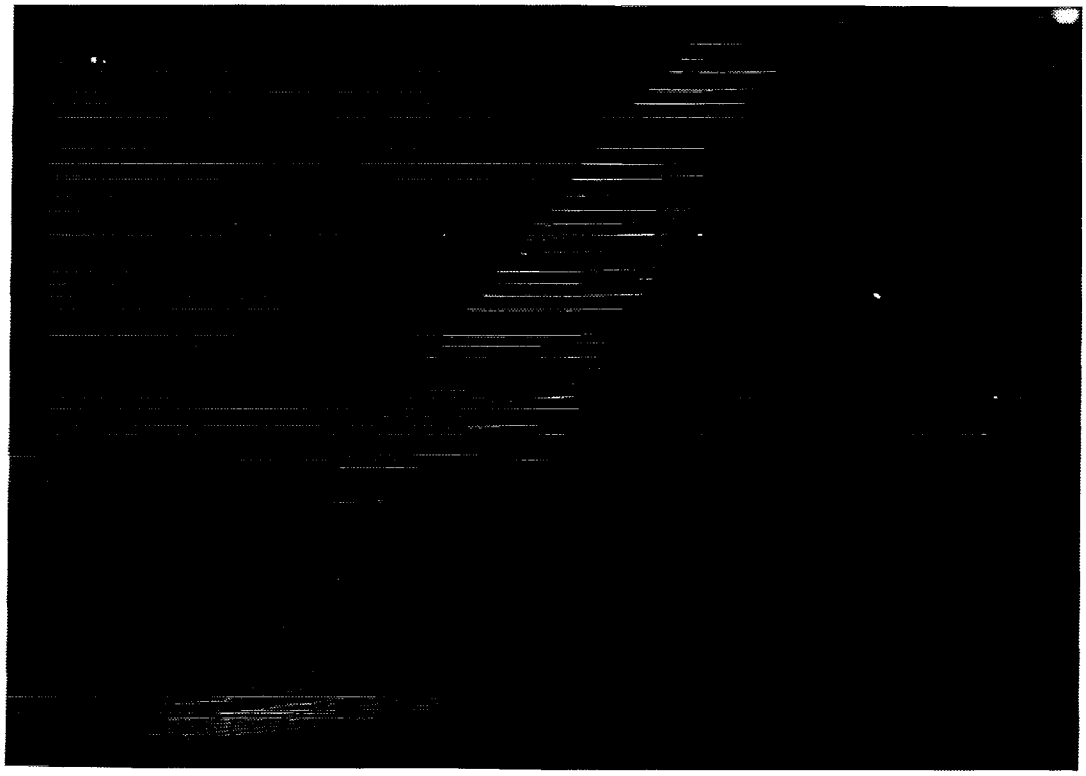

(a) $M_\infty = 0.50$, $\alpha = 6°$.

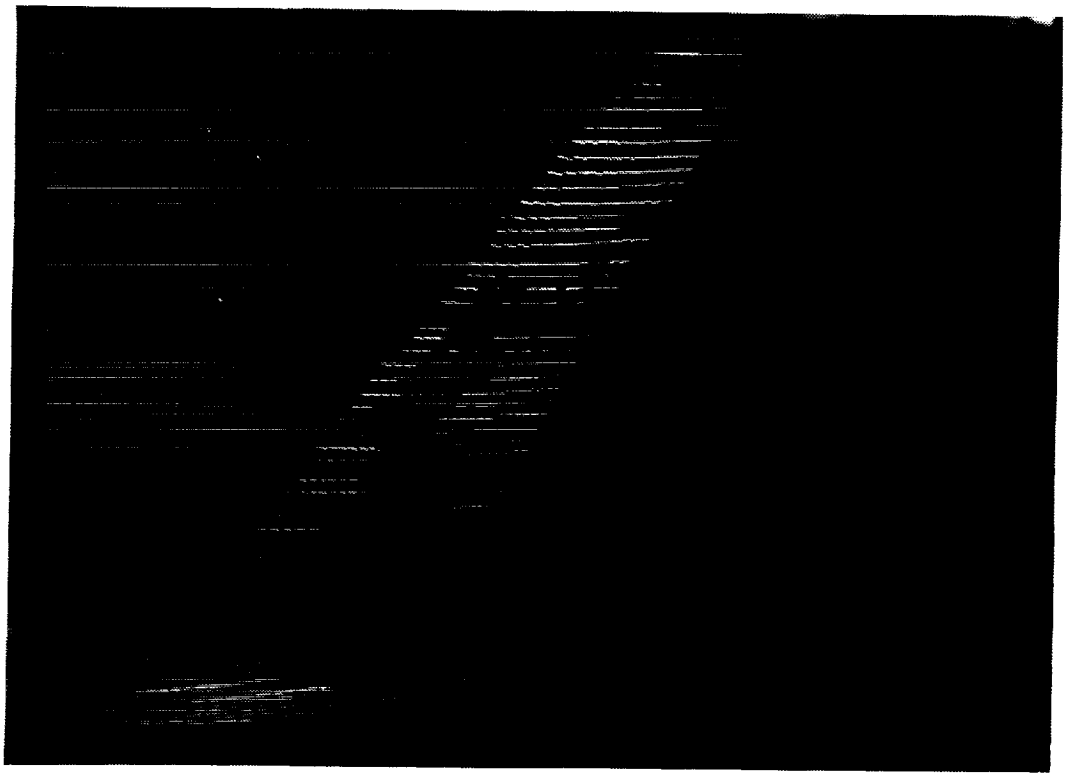

(b) $M_\infty = 0.825$, $\alpha = 4°$.

Figure 11. Fluorescent minituft flow visualization.

ORIGINAL PAGE IS
OF POOR QUALITY

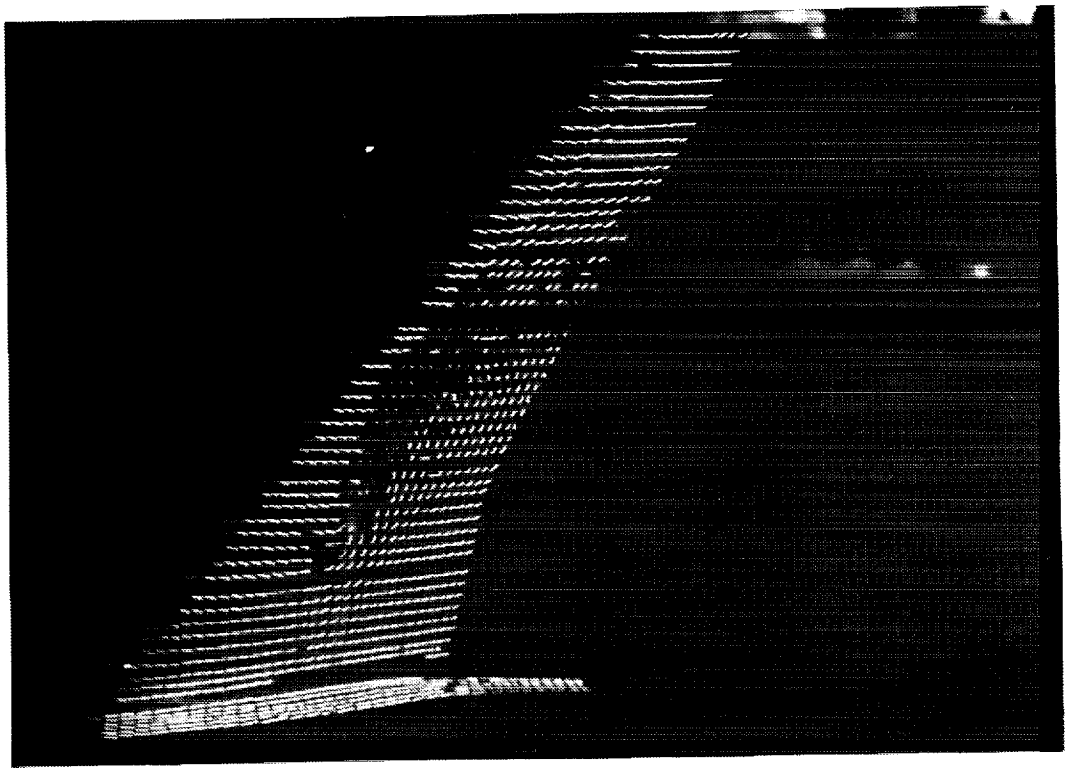

(c) $M_\infty = 0.825$, $\alpha = 6°$.

Figure 11. Concluded.

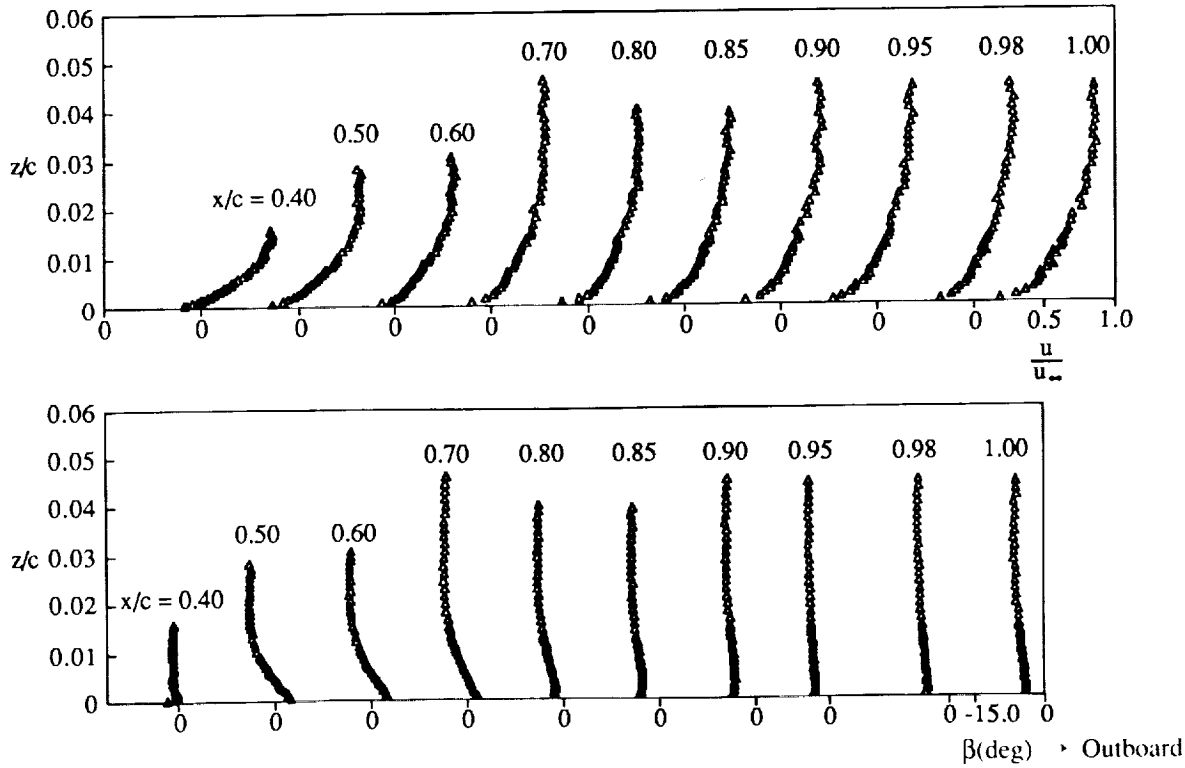

(a) $\eta = 0.165$, probe 1

Figure 12. Boundary-layer profiles; $M_\infty = 0.50$, $\alpha = 6°$.

ORIGINAL PAGE IS
OF POOR QUALITY

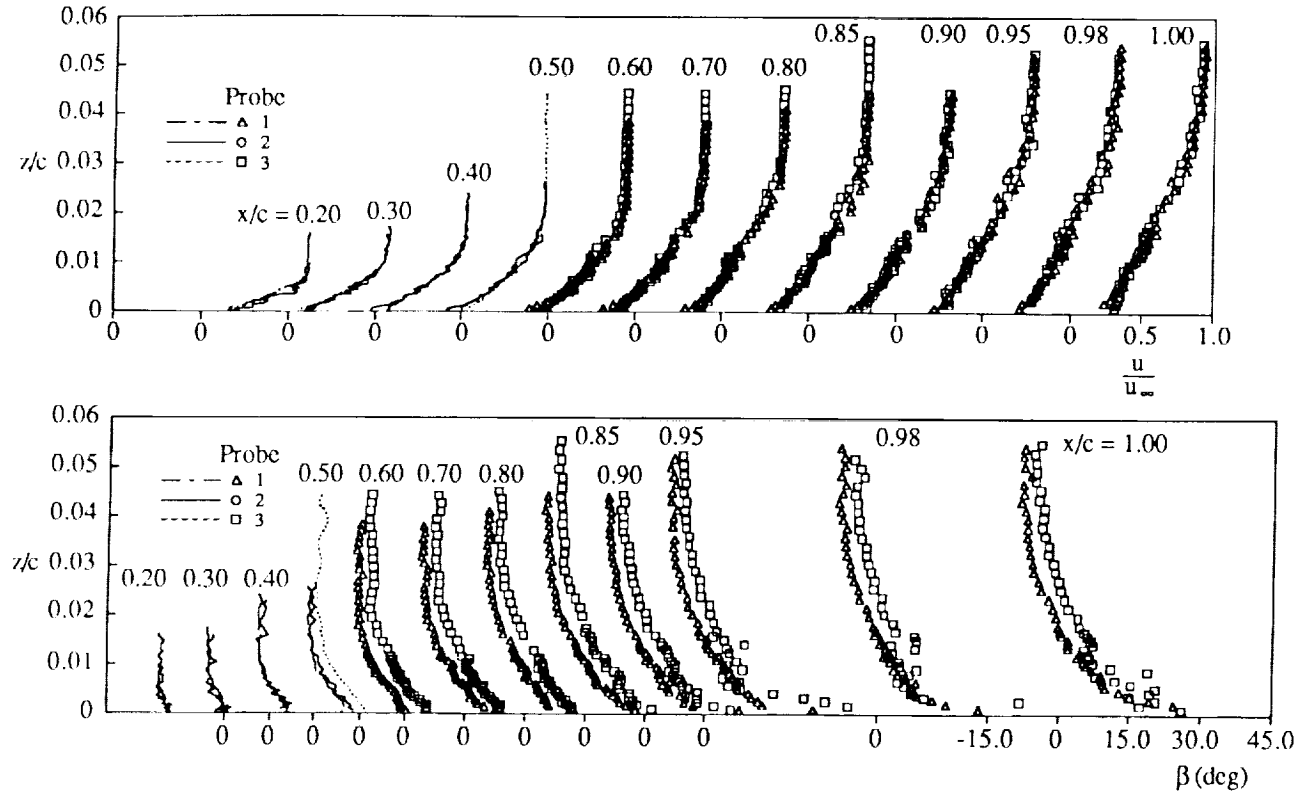

(b) $\eta = 0.300$

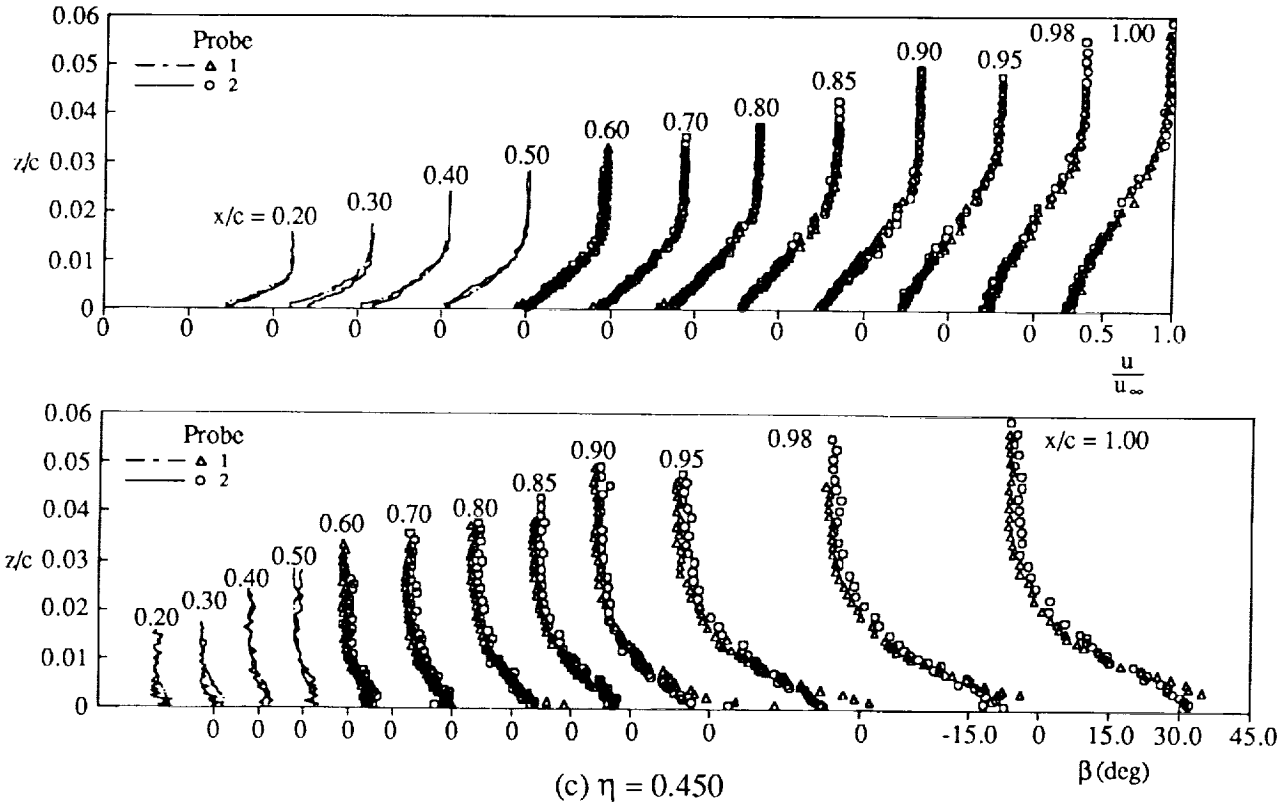

(c) $\eta = 0.450$

Figure 12. Continued.

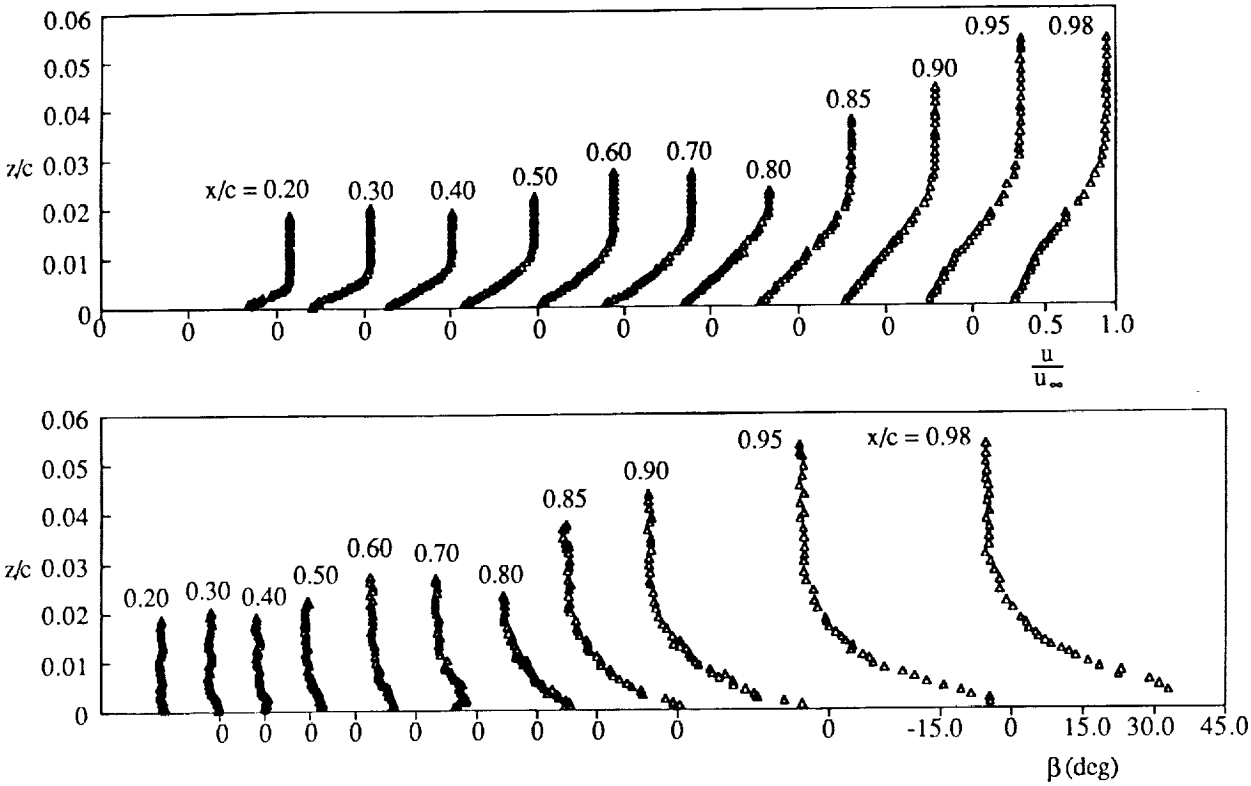

(d) $\eta = 0.575$, probe 1

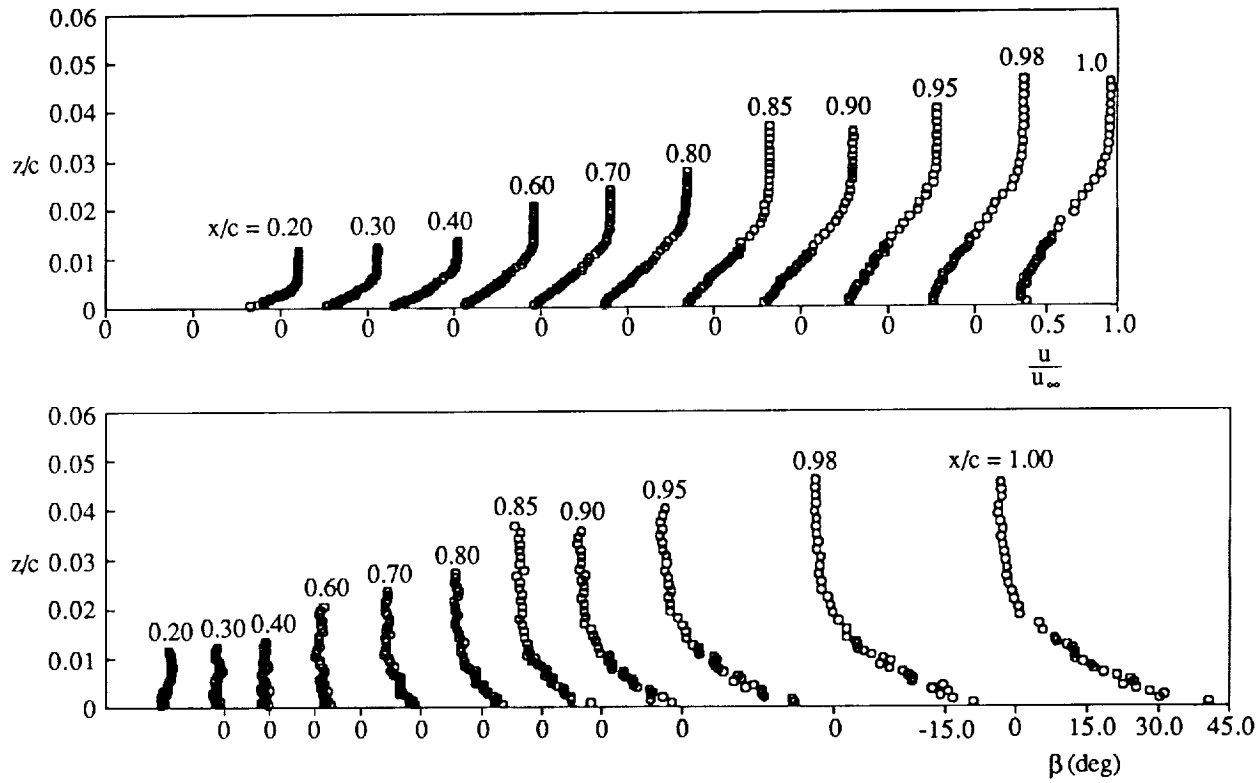

(e) $\eta = 0.650$, probe 2

Figure 12. Continued.

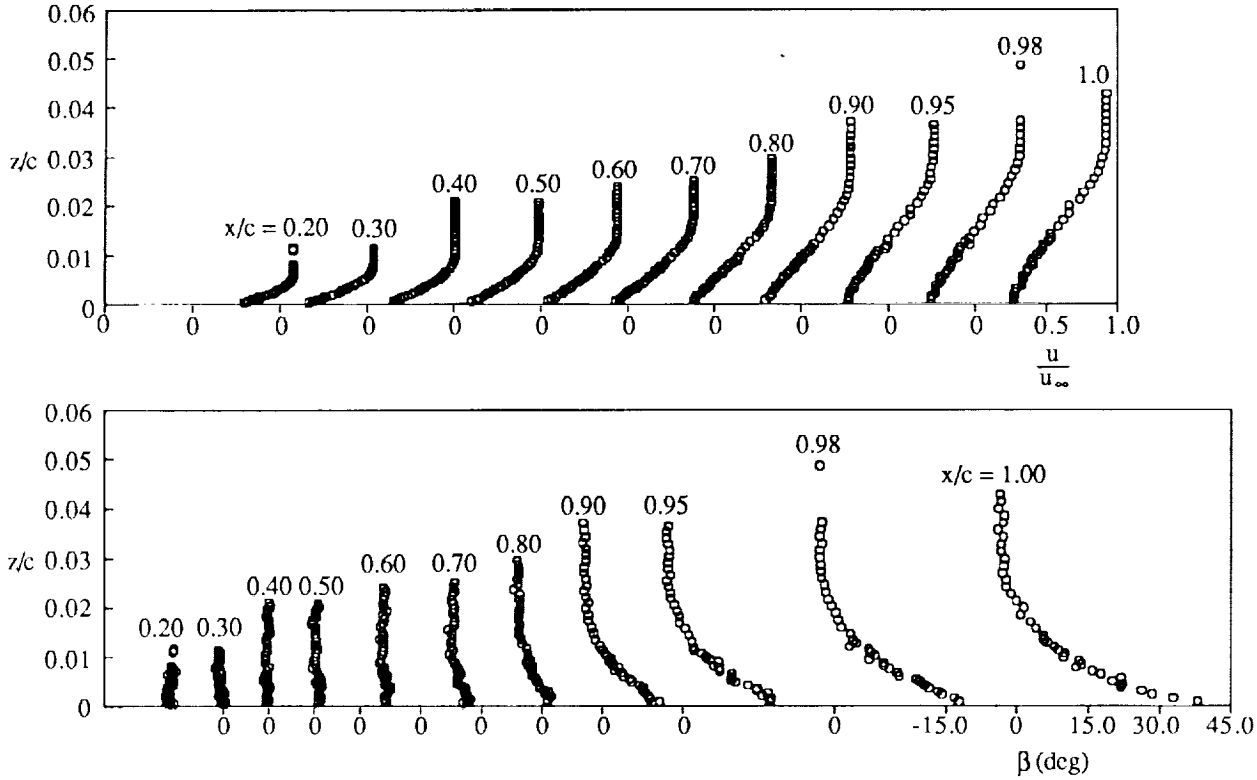

(f) $\eta = 0.725$, probe 2

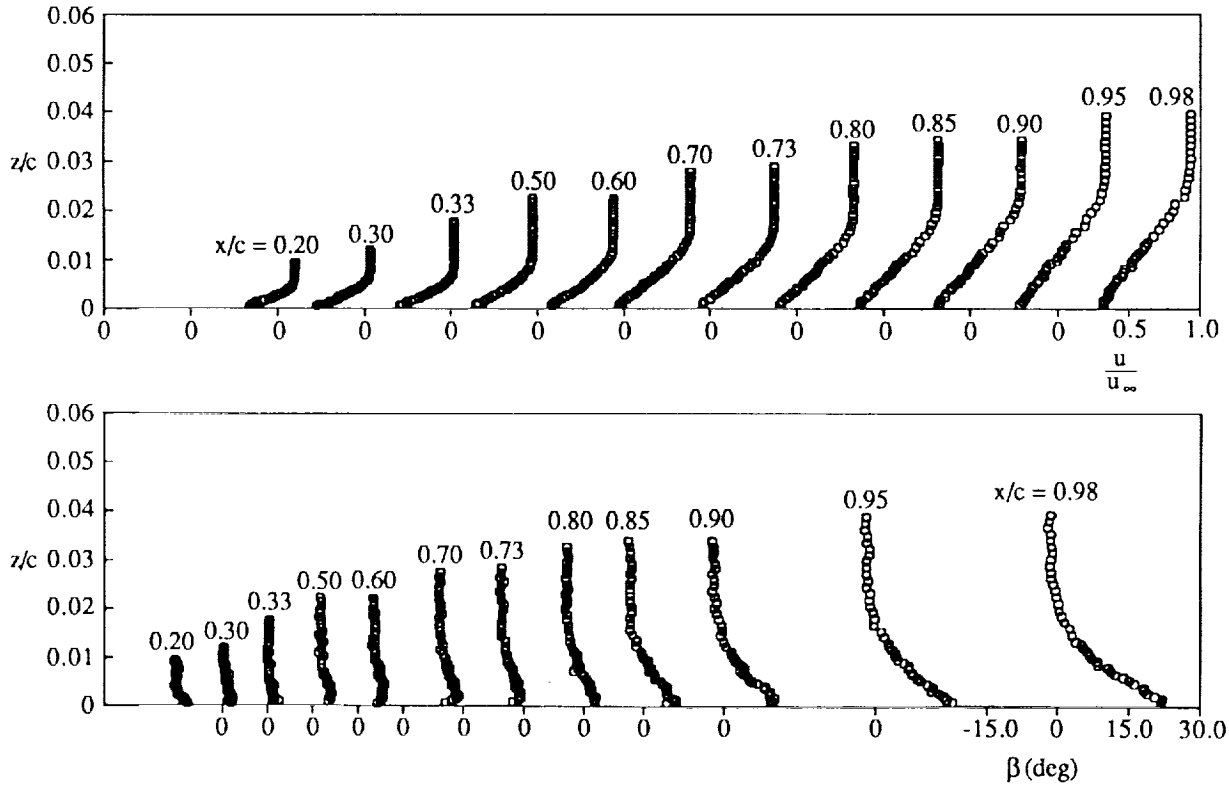

(g) $\eta = 0.800$, probe 2

Figure 12. Continued.

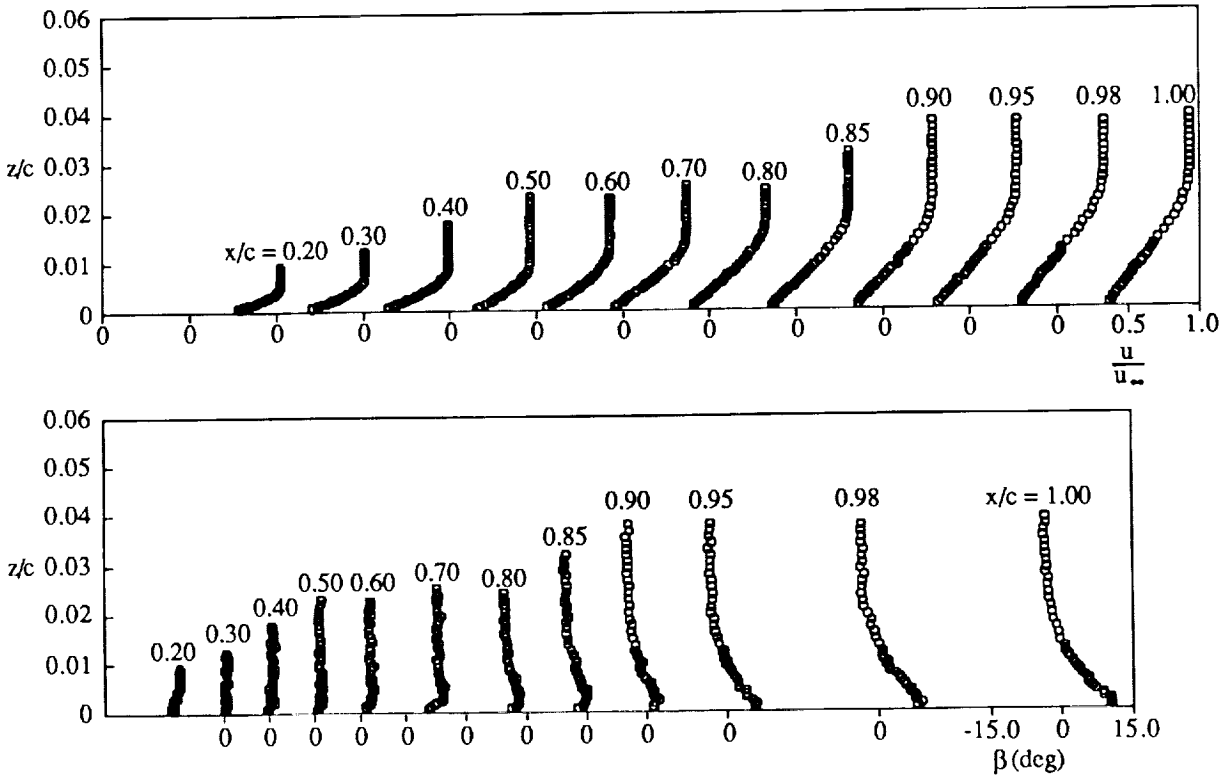

(h) $\eta = 0.900$, probe 2

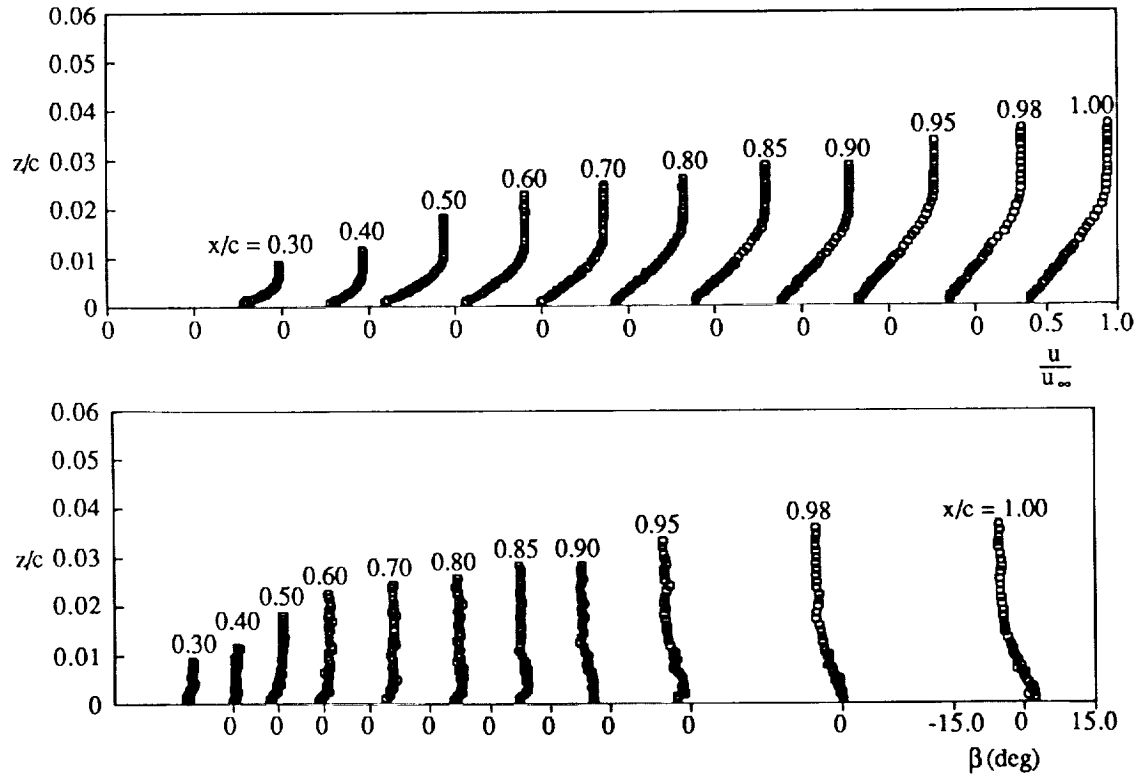

(i) $\eta = 0.950$, probe 2

Figure 12. Concluded.

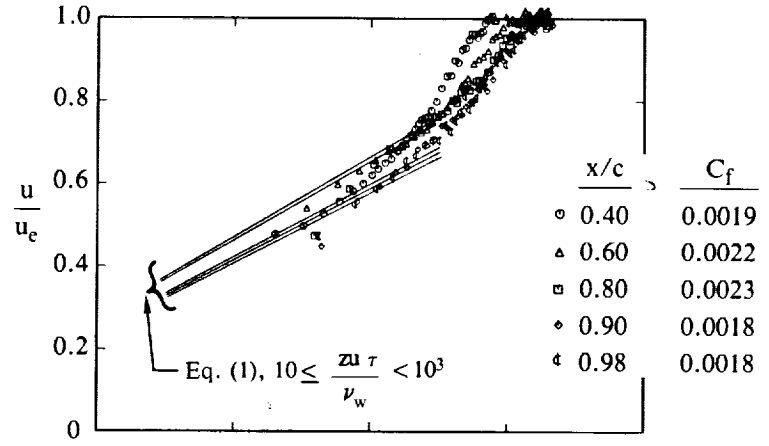

(a) $\eta = 0.165$, probe 1

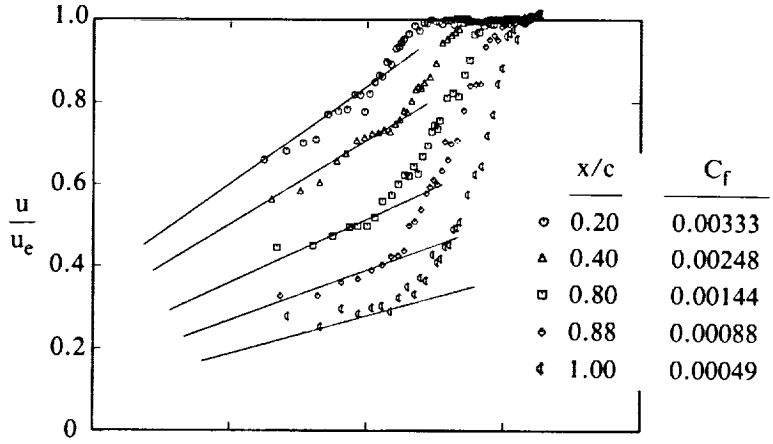

(b) $\eta = 0.450$, probe 2

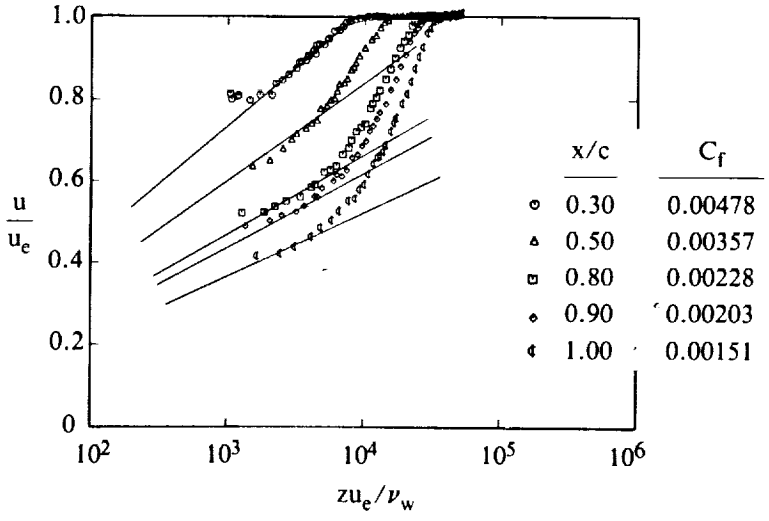

(c) $\eta = 0.950$, probe 2

Figure 13. Velocity magnitude profiles in semilog coordinates; $M_\infty = 0.50$, $\alpha = 6°$.

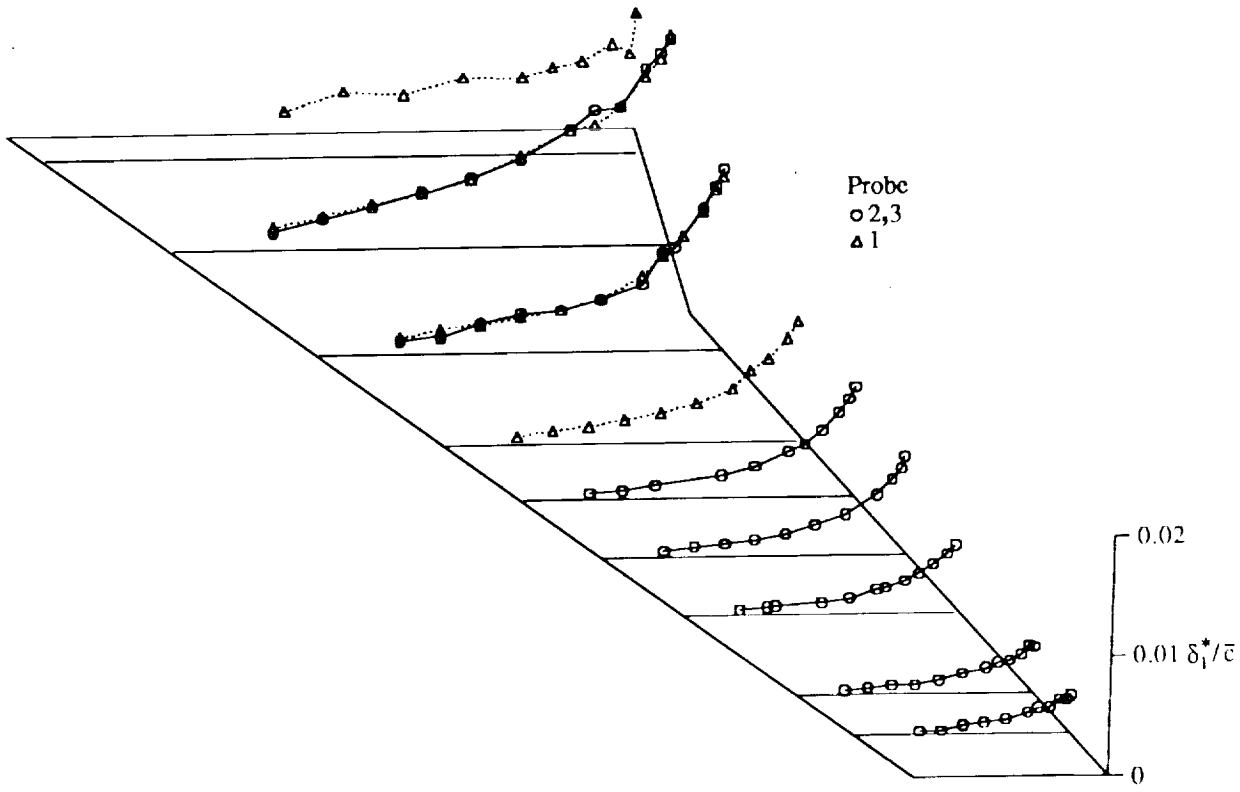

Figure 14. Projections on a wing planform of streamwise displacement-thickness distributions; $M_\infty = 0.50$, $\alpha = 6°$.

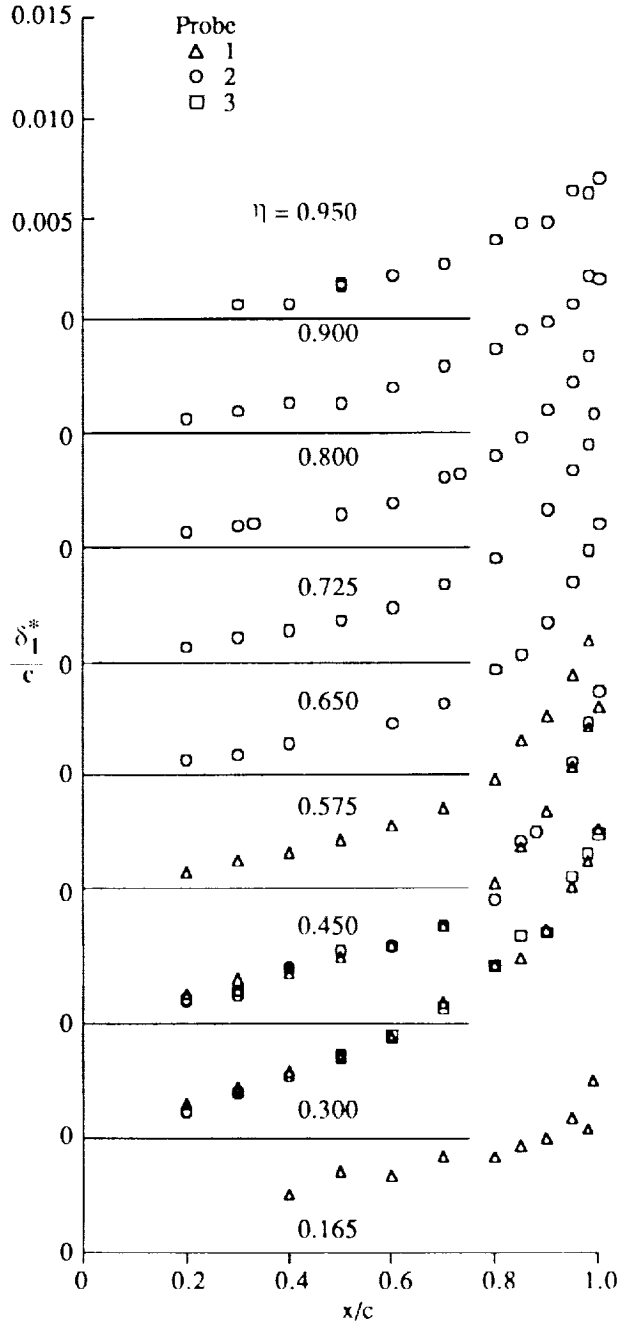

Figure 15. Streamwise displacement-thickness distributions; $M_\infty = 0.50$, $\alpha = 6°$.

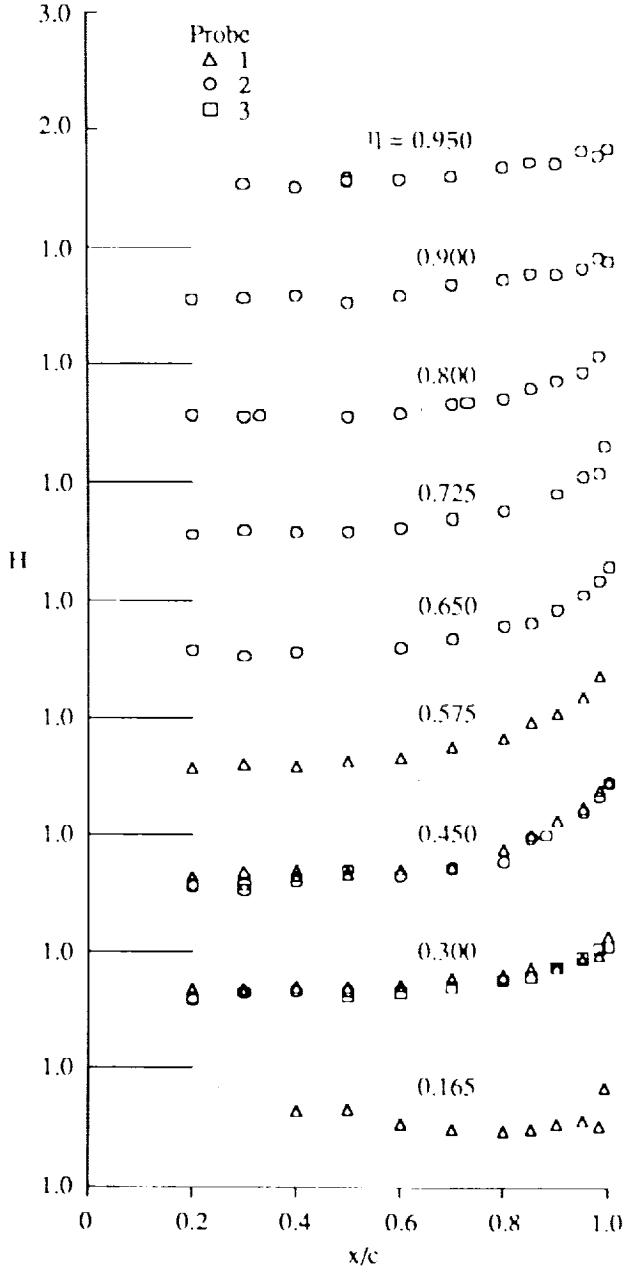

Figure 16. Shape factor distributions; $M_\infty = 0.50$, $\alpha = 6°$.

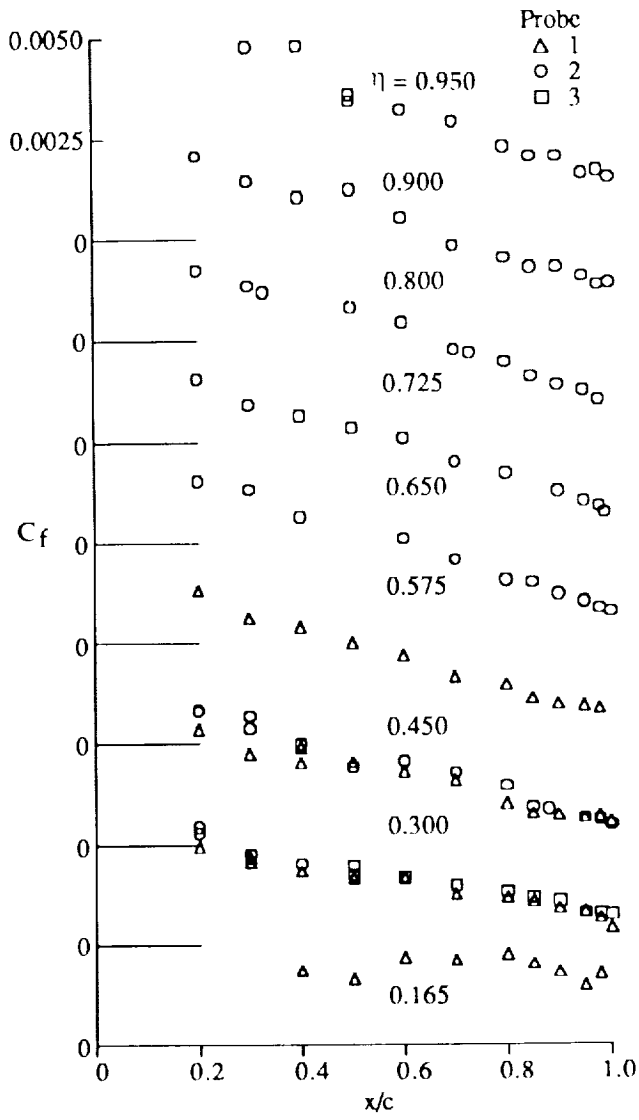

Figure 17. Skin friction distributions; $M_\infty = 0.50$, $\alpha = 6°$.

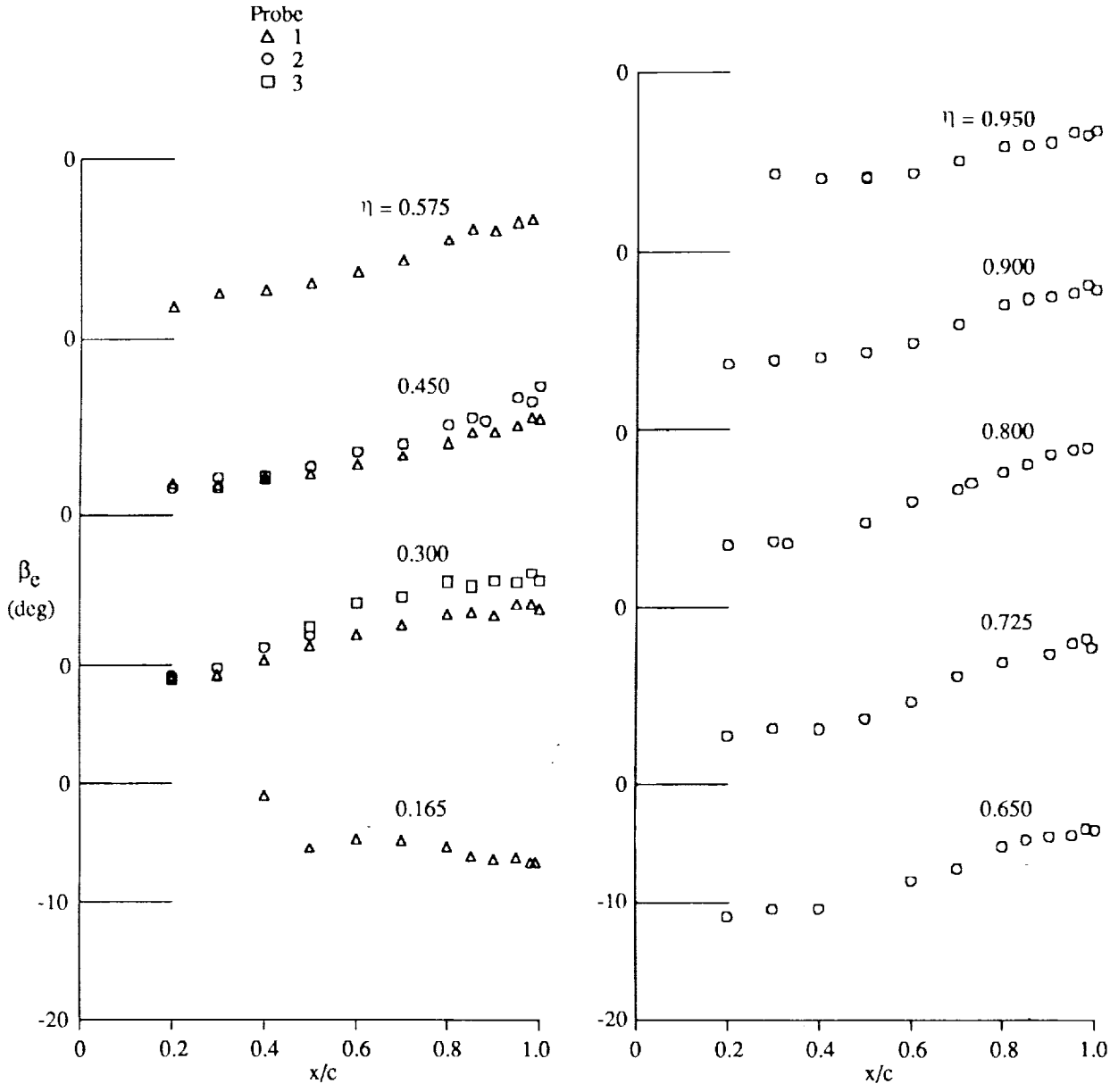

Figure 18. Distributions of yaw-plane flow direction at the boundary-layer edge (β is positive outboard); $M_\infty = 0.50$, $\alpha = 6°$.

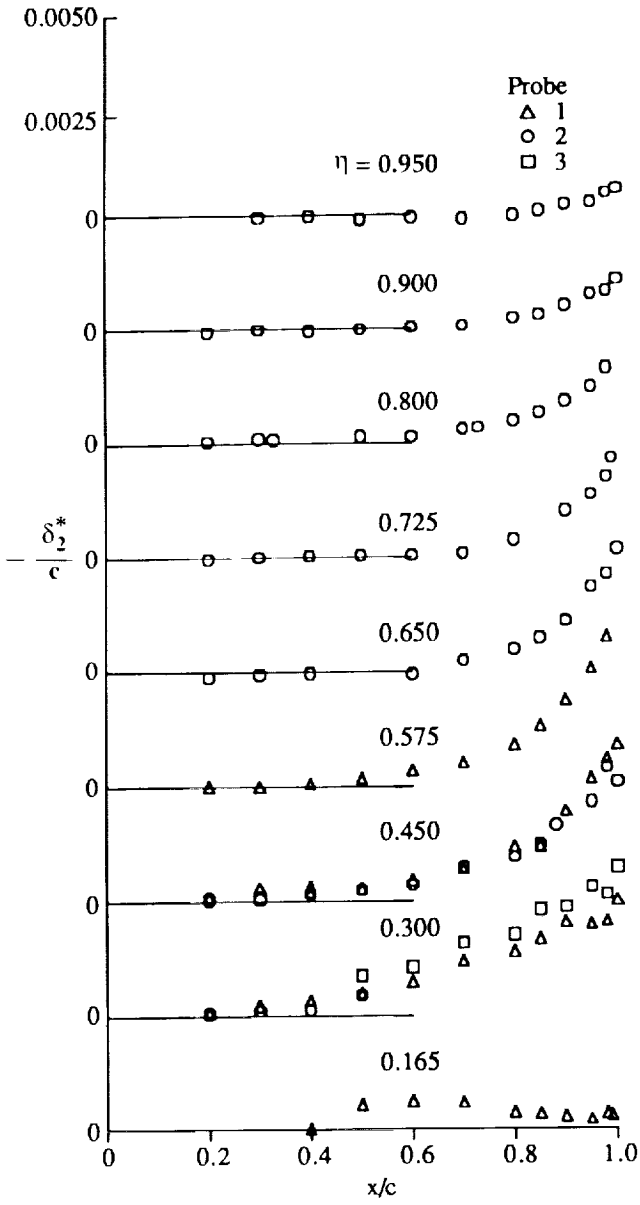

Figure 19. Crossflow displacement-thickness distributions; $M_\infty = 0.50$, $\alpha = 6°$.

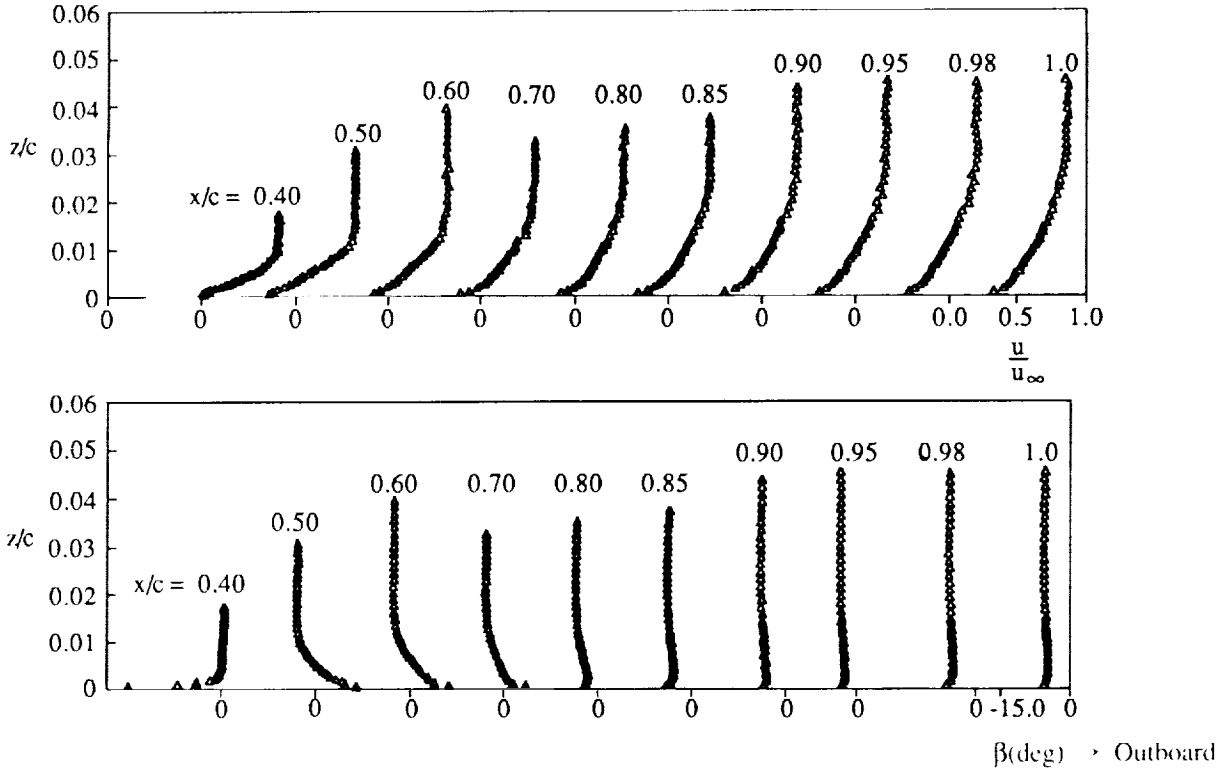

(a) $\eta = 0.165$, probe 1

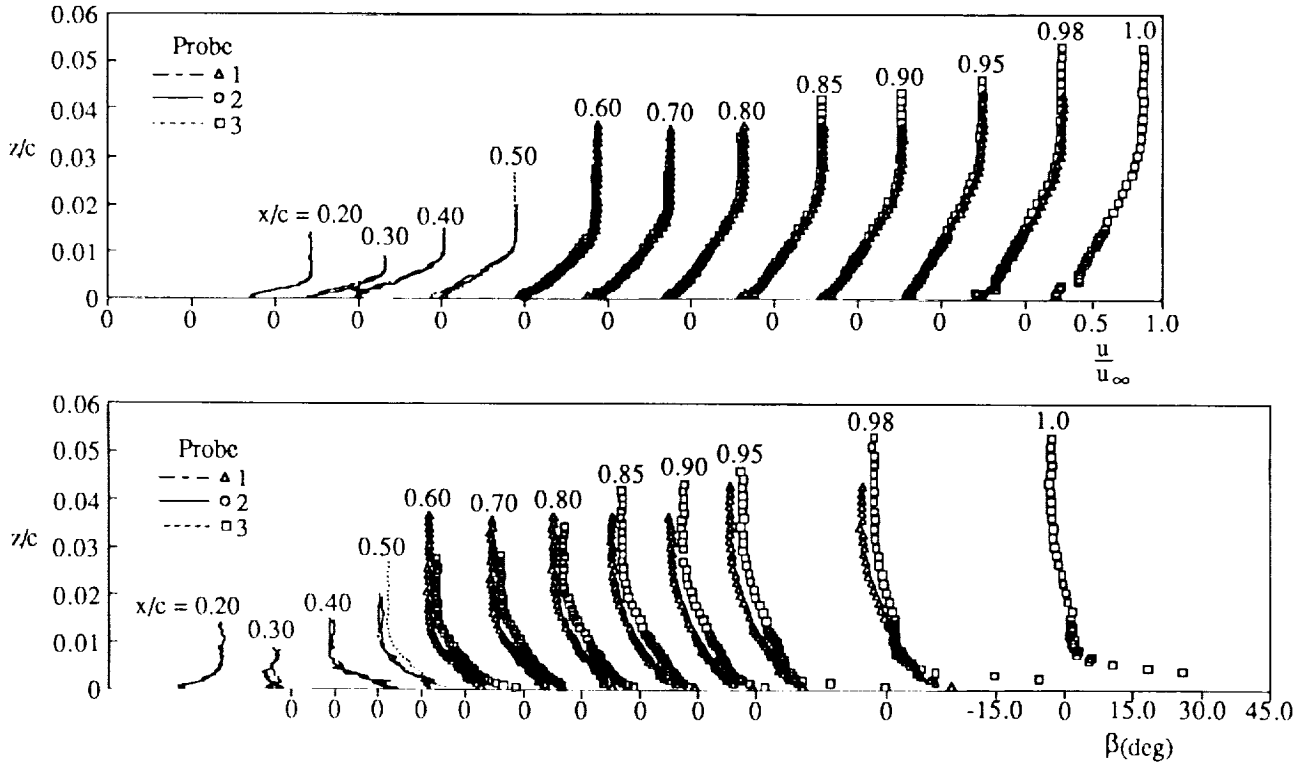

(b) $\eta = 0.300$

Figure 20. Boundary-layer profiles; $M_\infty = 0.825$, $\alpha = 4°$.

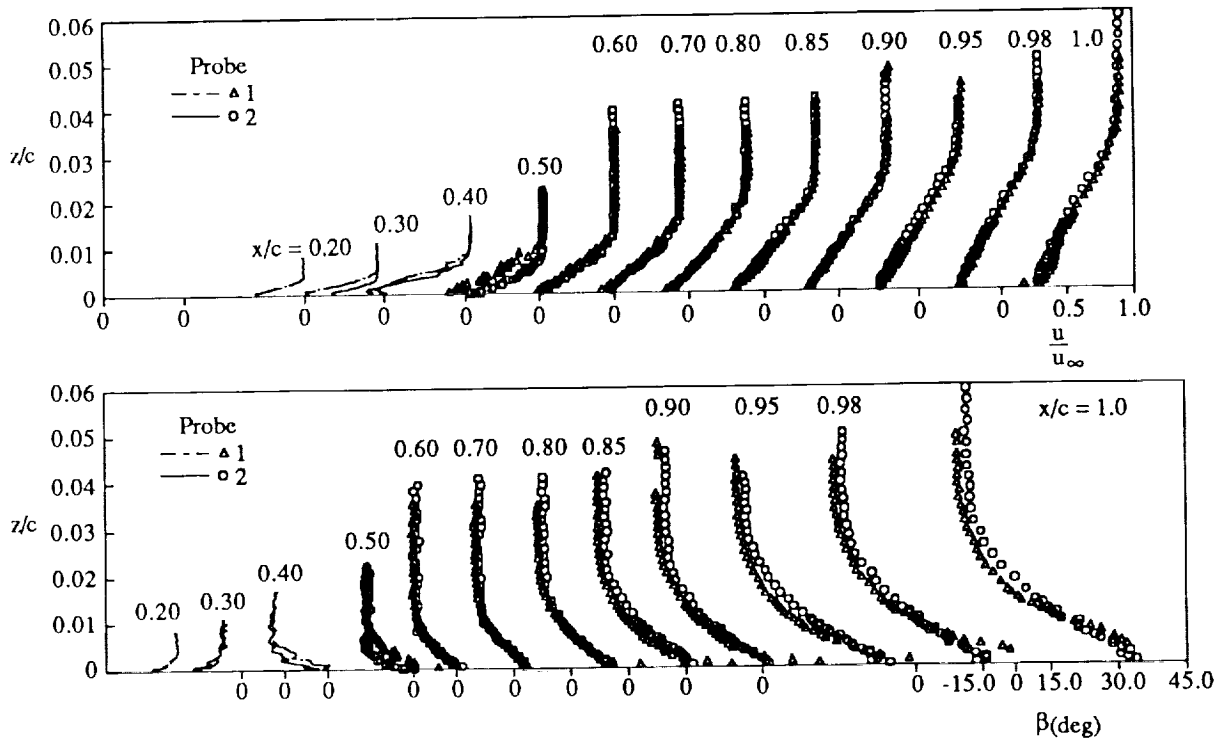

(c) $\eta = 0.450$

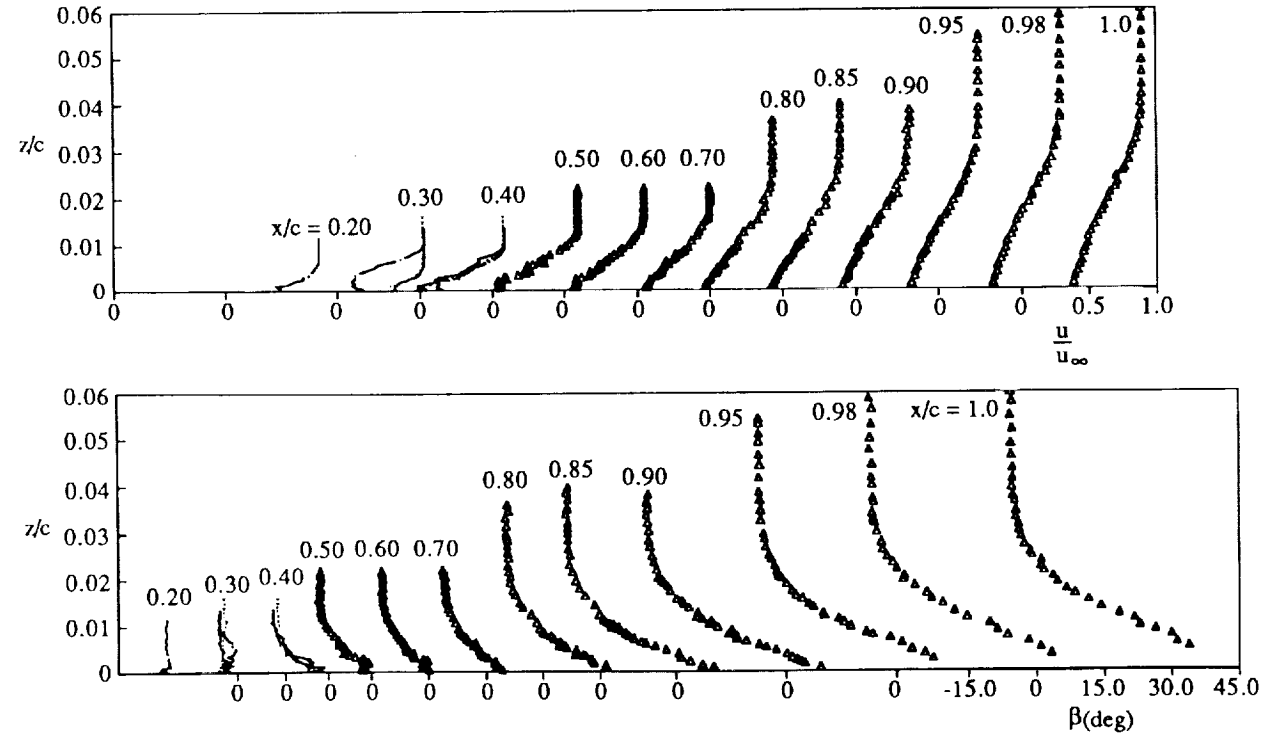

(d) $\eta = 0.575$, probe 1

Figure 20. Continued.

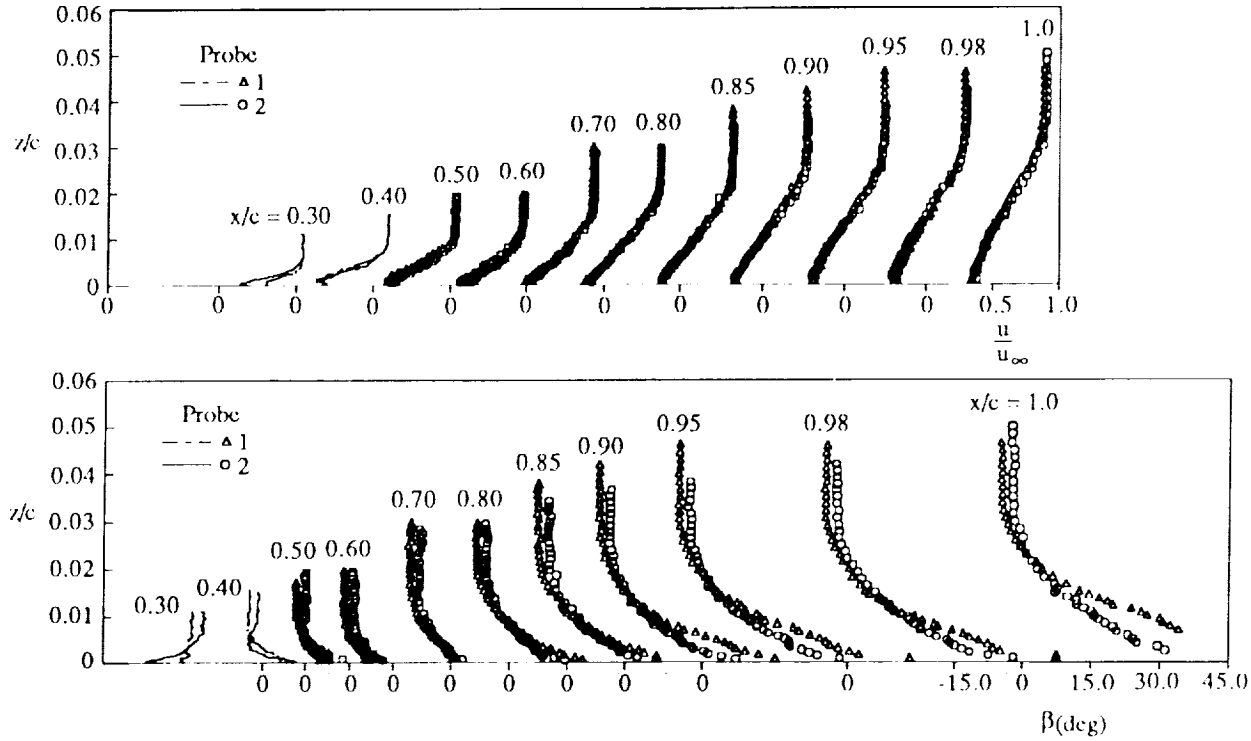

(e) $\eta = 0.650$

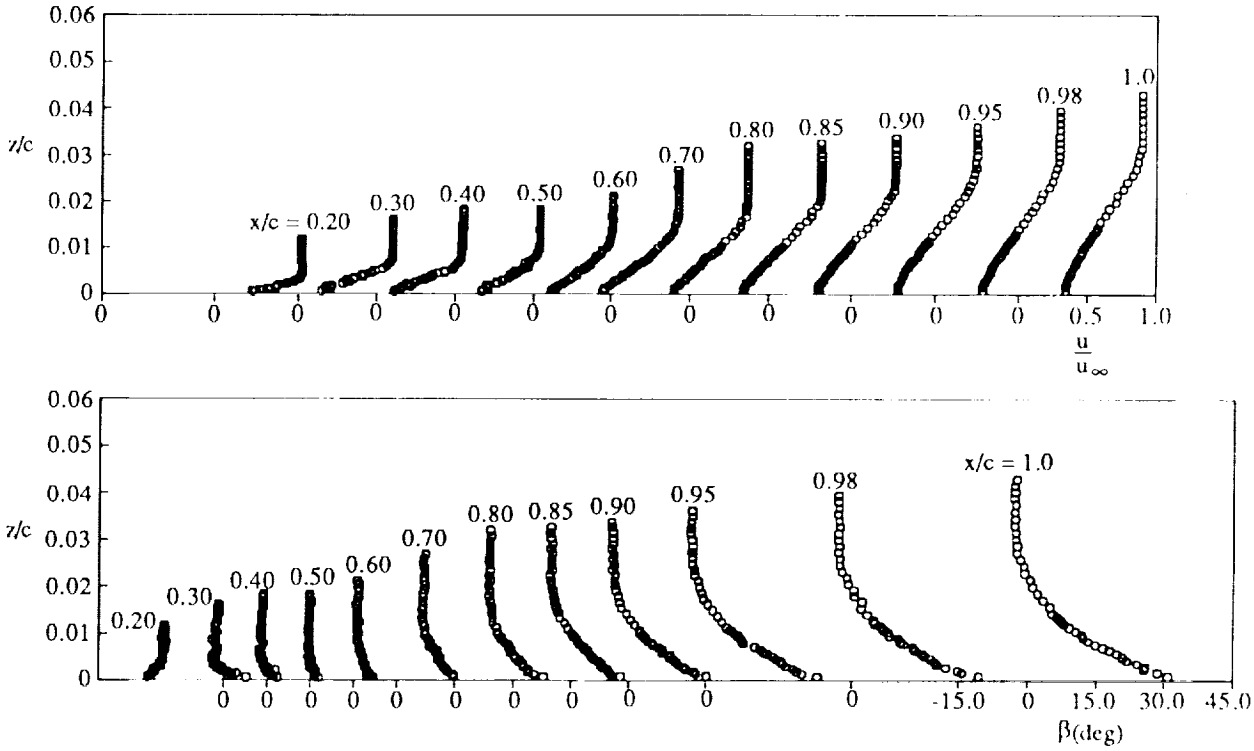

(f) $\eta = 0.725$, probe 2

Figure 20. Continued.

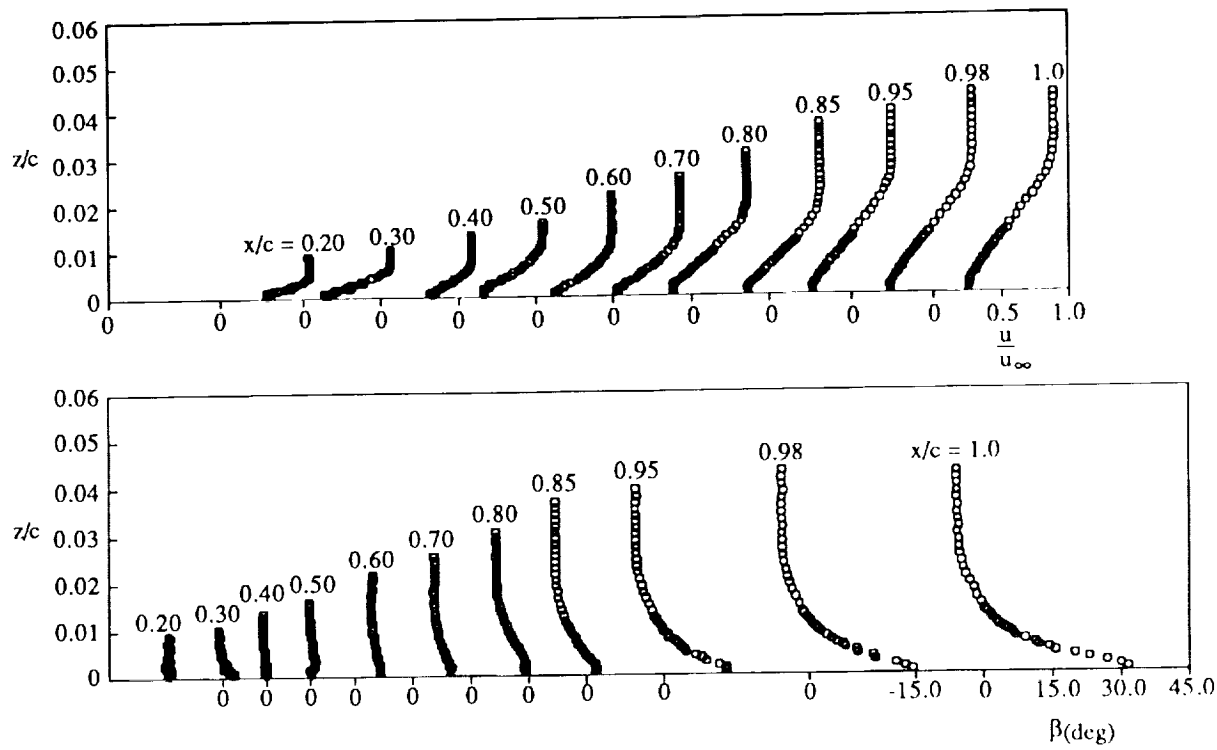

(g) $\eta = 0.800$, probe 2

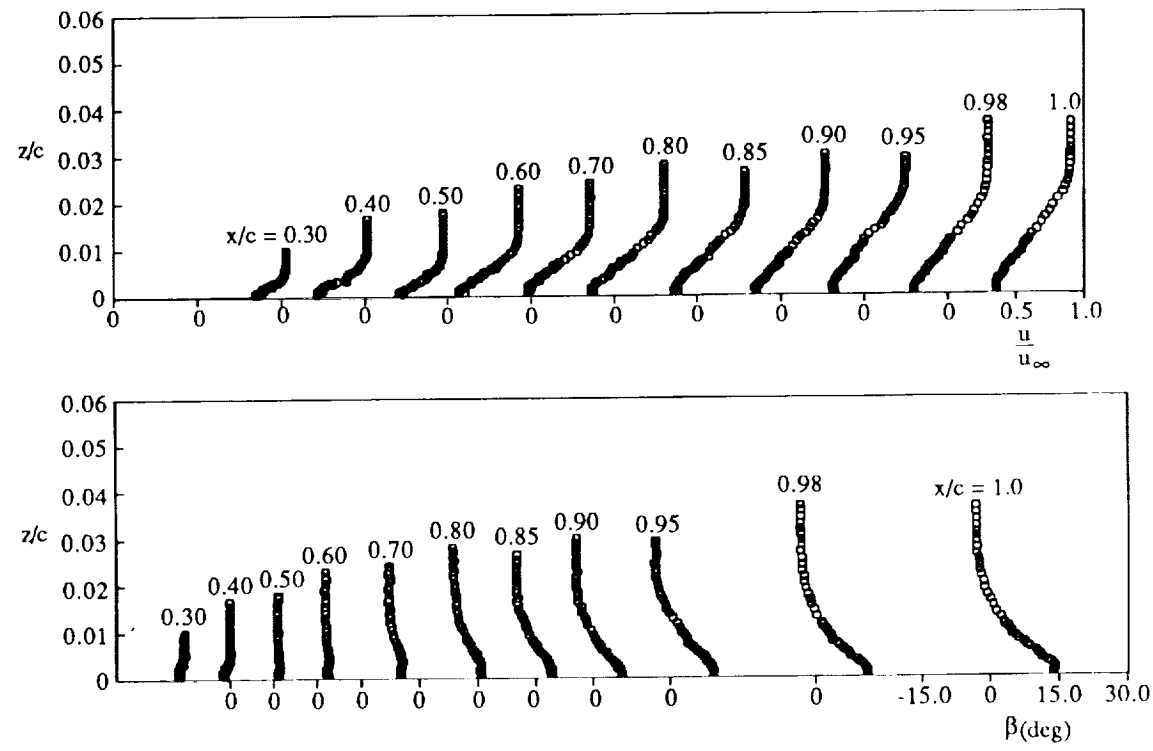

(h) $\eta = 0.900$, probe 2

Figure 20. Continued.

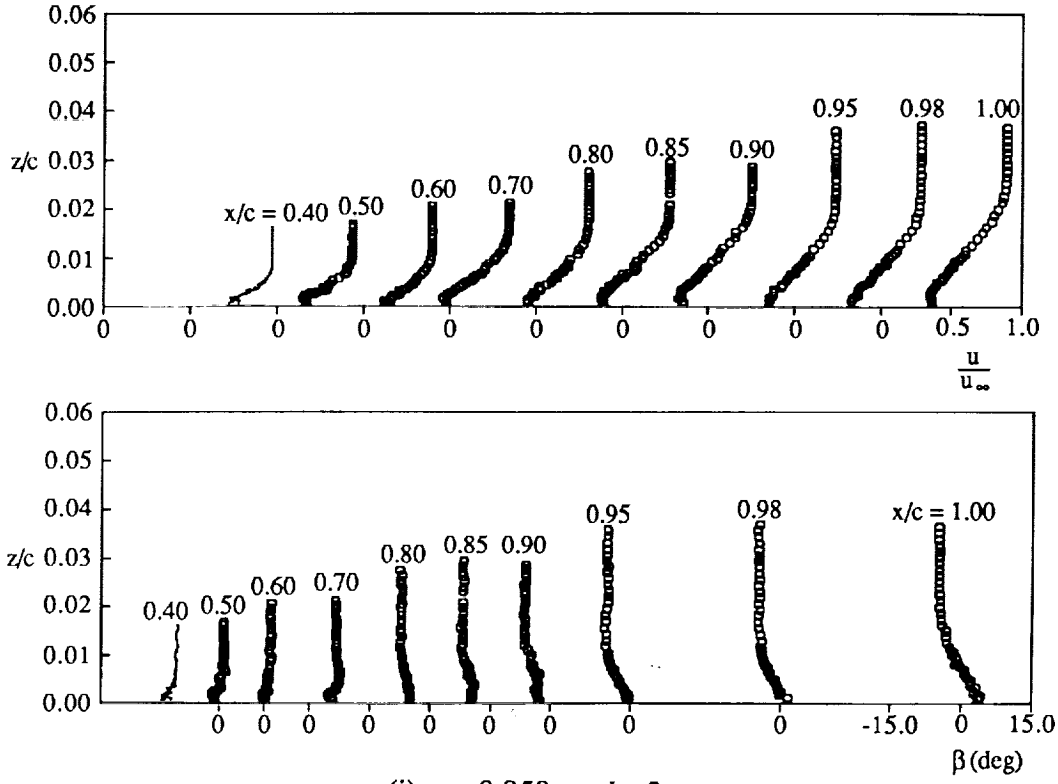

(i) $\eta = 0.950$, probe 2

Figure 20. Concluded.

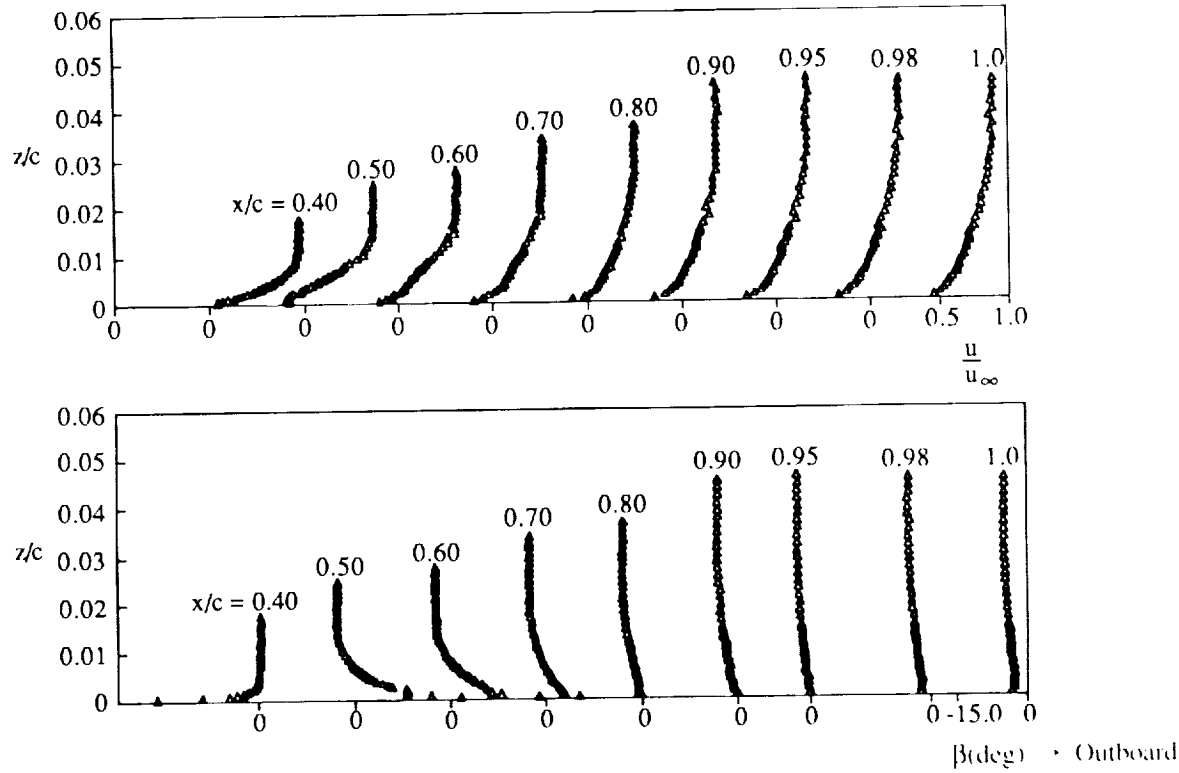

(a) $\eta = 0.165$

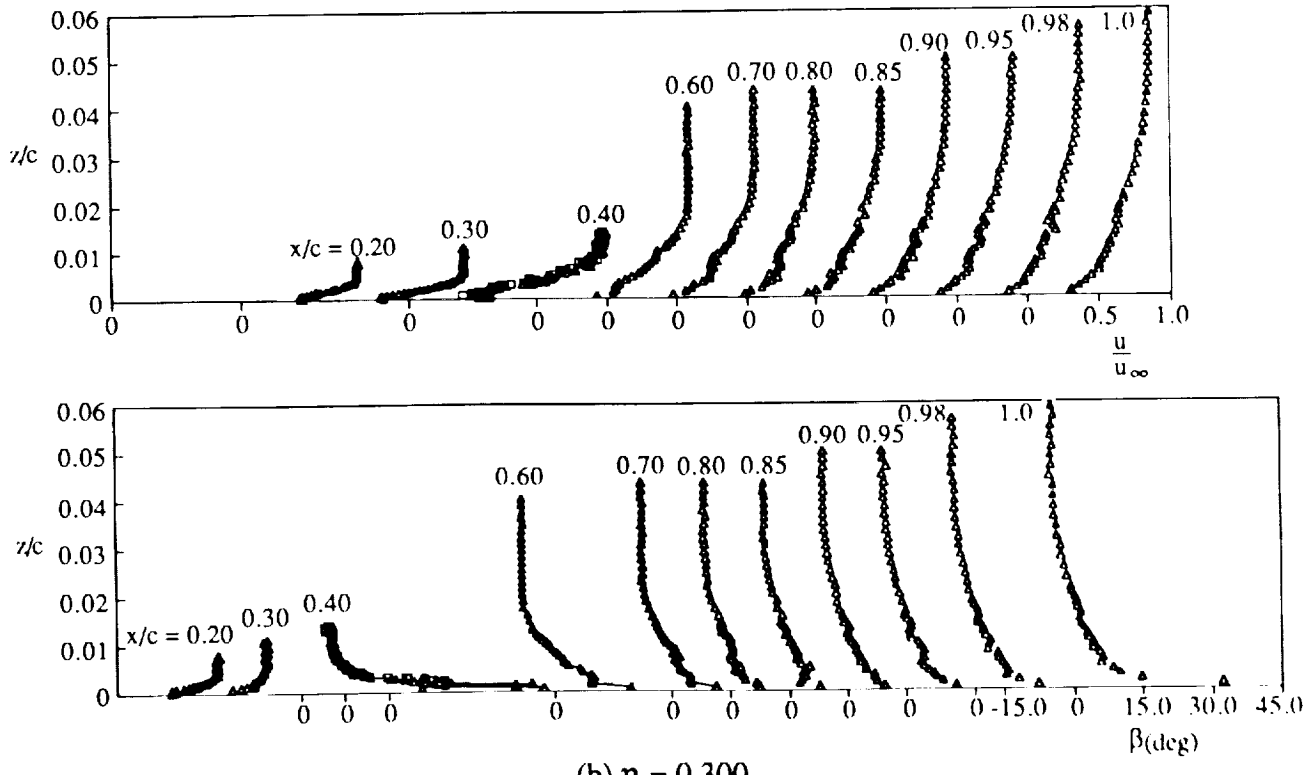

(b) $\eta = 0.300$

Figure 21. Boundary-layer profiles; $M_\infty = 0.825$, $\alpha = 6°$, probe 1.

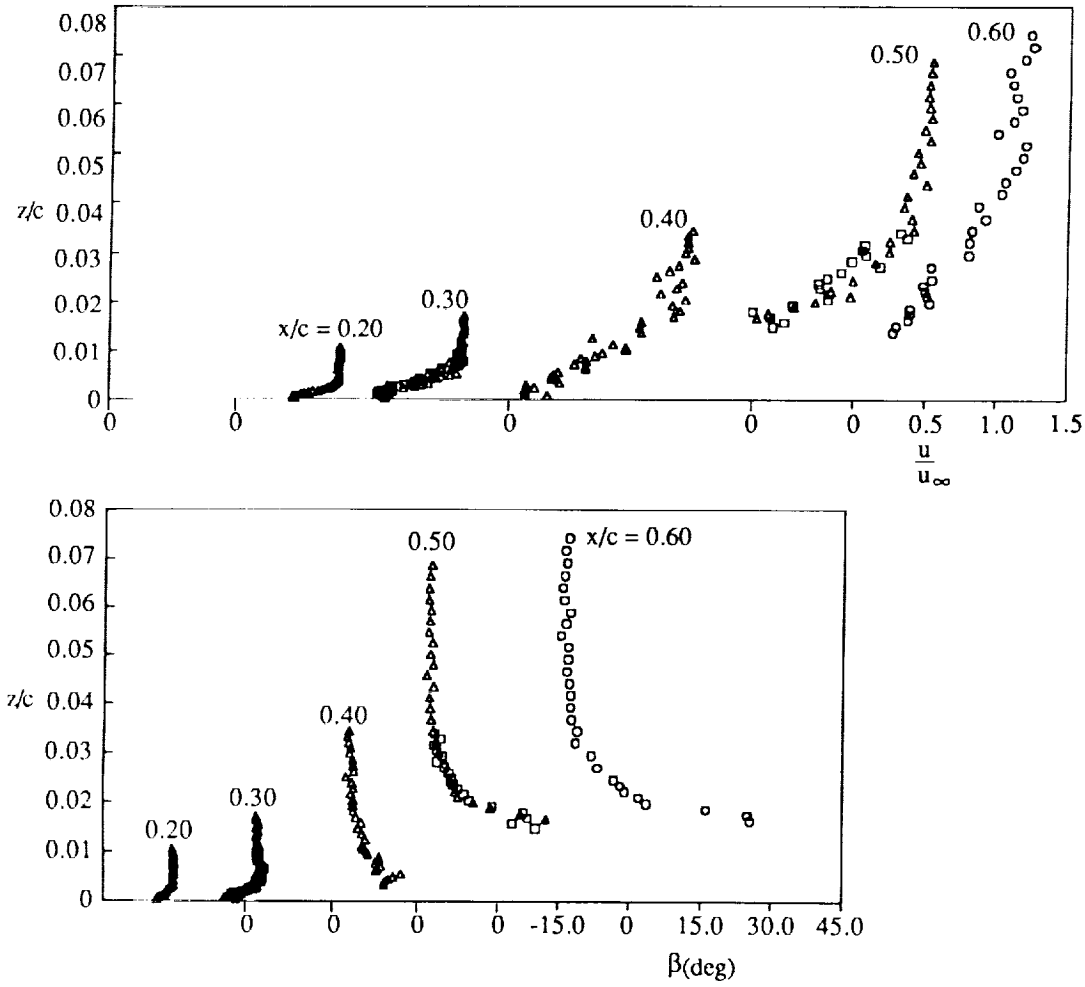

(c) $\eta = 0.450$

Figure 21. Continued.

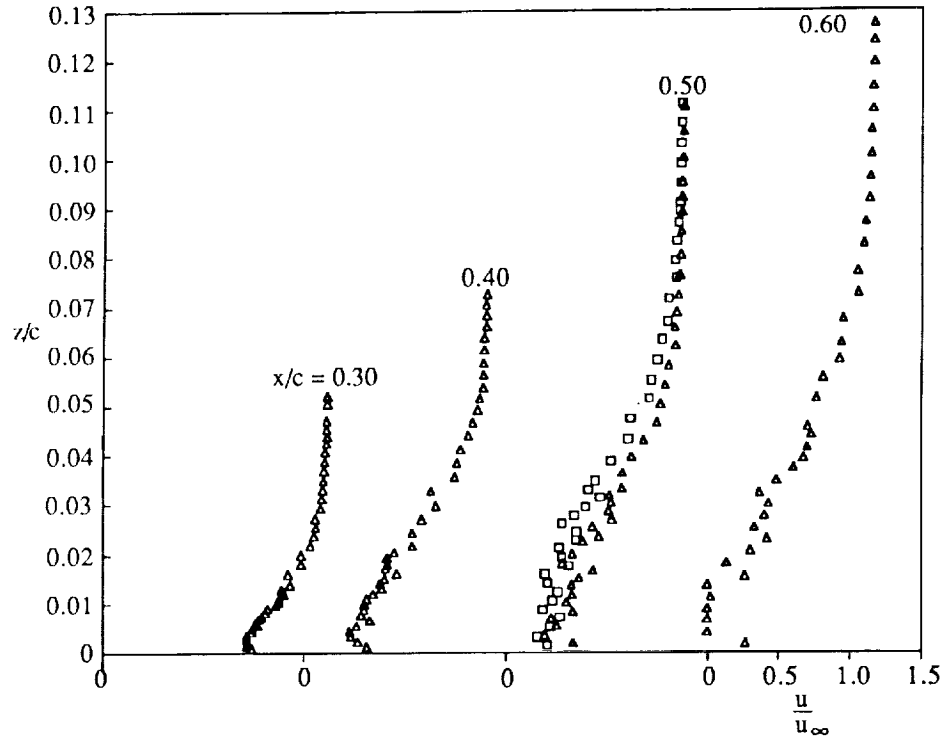

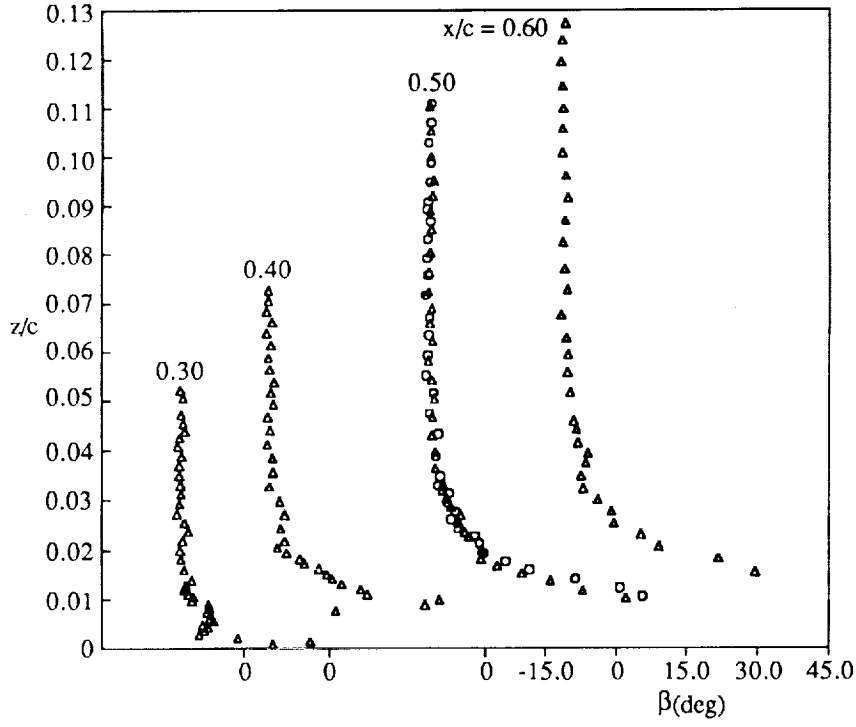

(d) $\eta = 0.575$

Figure 21. Continued.

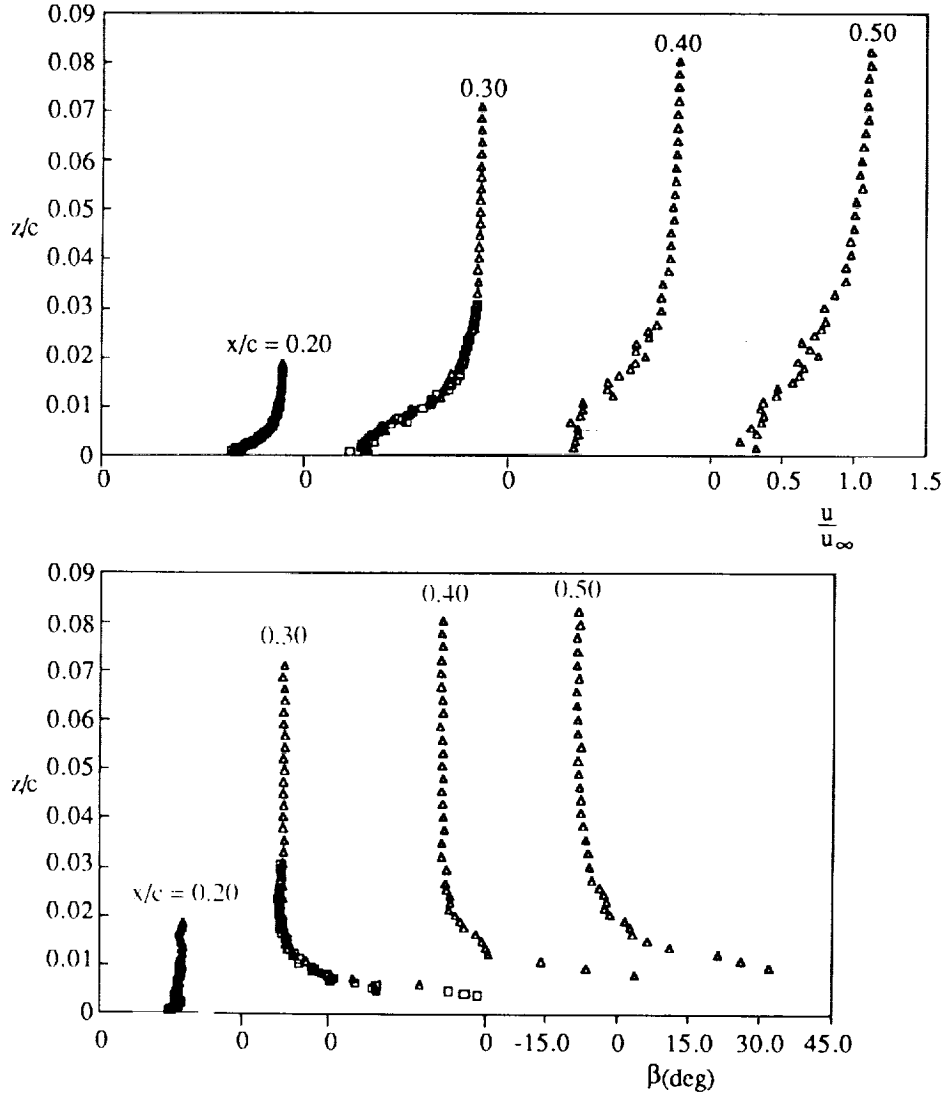

(e) $\eta = 0.650$

Figure 21. Concluded.

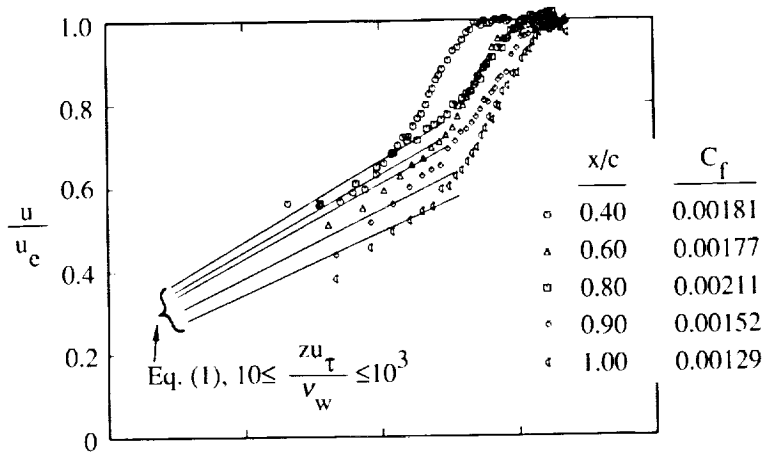

(a) $\eta = 0.165$, probe 1

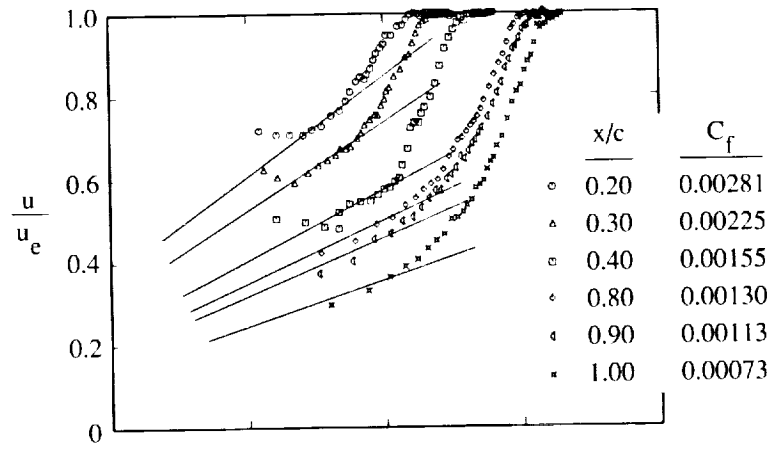

(b) $\eta = 0.300$, probe 2

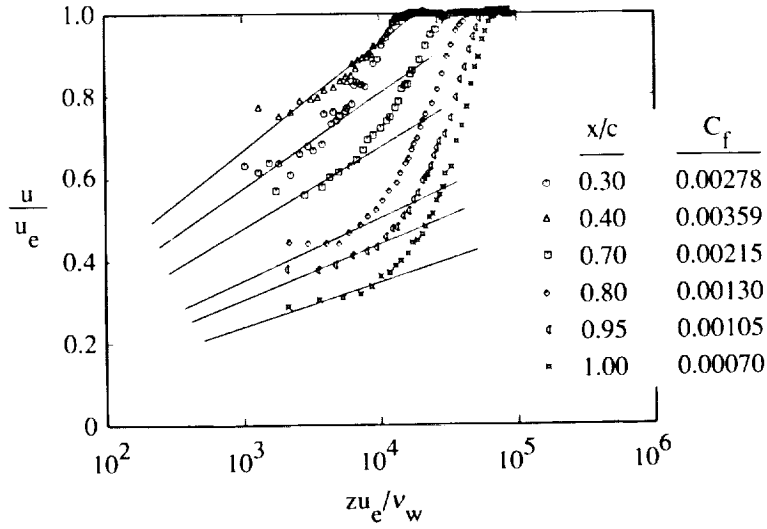

(c) $\eta = 0.800$, probe 2

Figure 22. Velocity magnitude profiles in semilog coordinates; $M_\infty = 0.825$, $\alpha = 4°$.

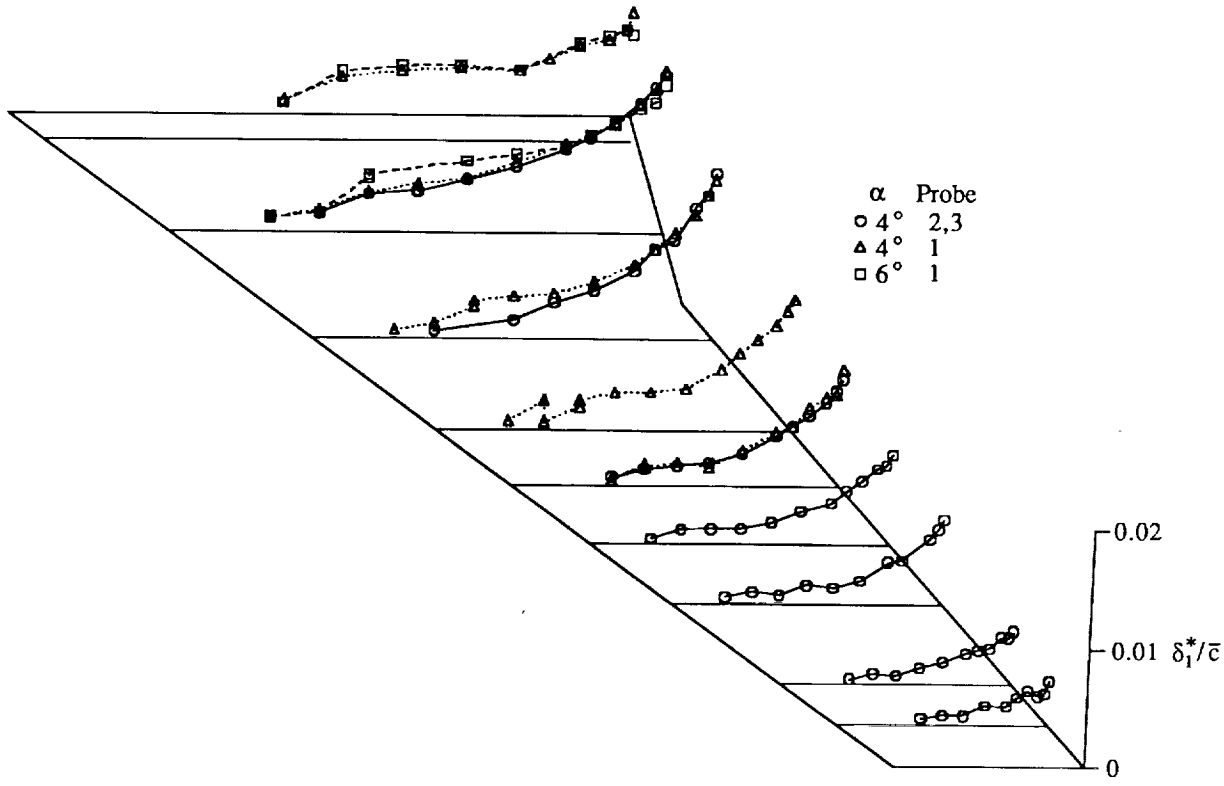

Figure 23. Projections on a wing planform of streamwise displacement-thickness distributions; $M_\infty = 0.825$.

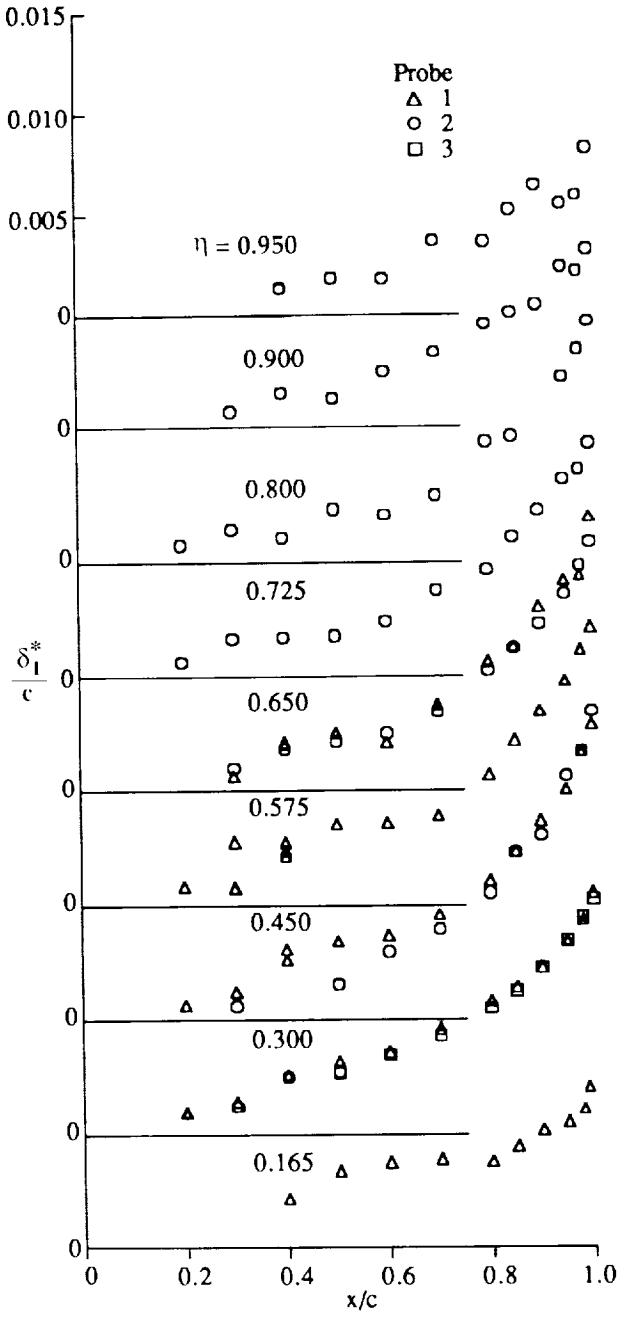

Figure 24. Streamwise displacement-thickness distributions; $M_\infty = 0.825$, $\alpha = 4°$.

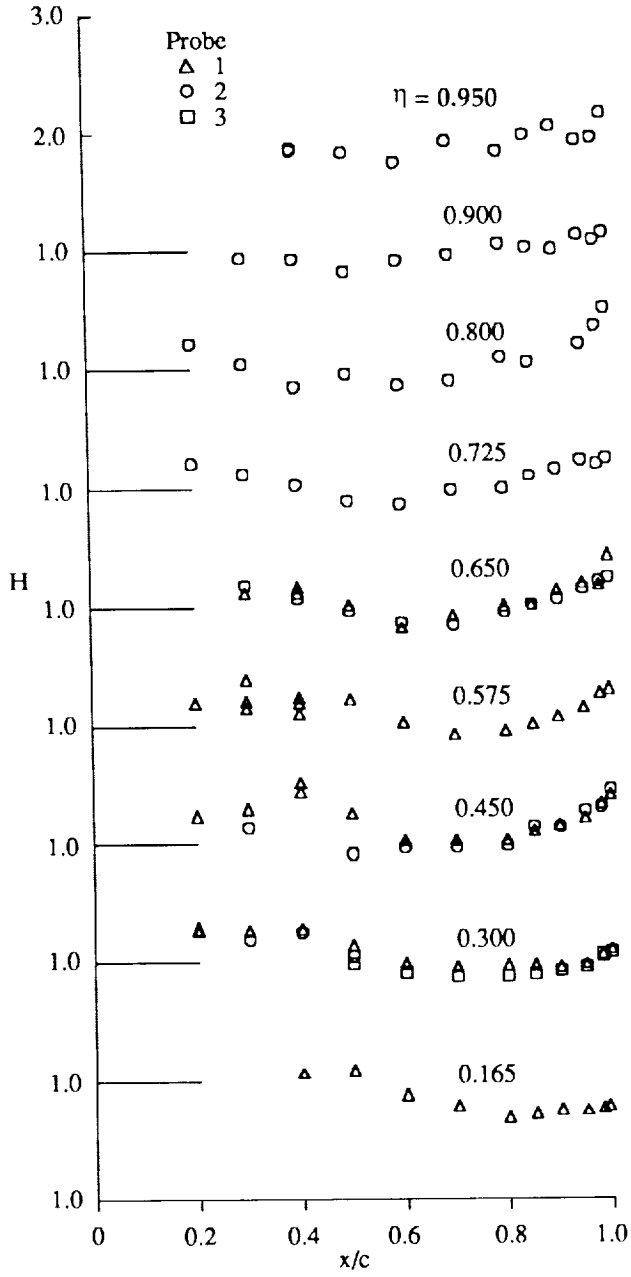

Figure 25. Shape factor distributions; $M_\infty = 0.825$, $\alpha = 4°$.

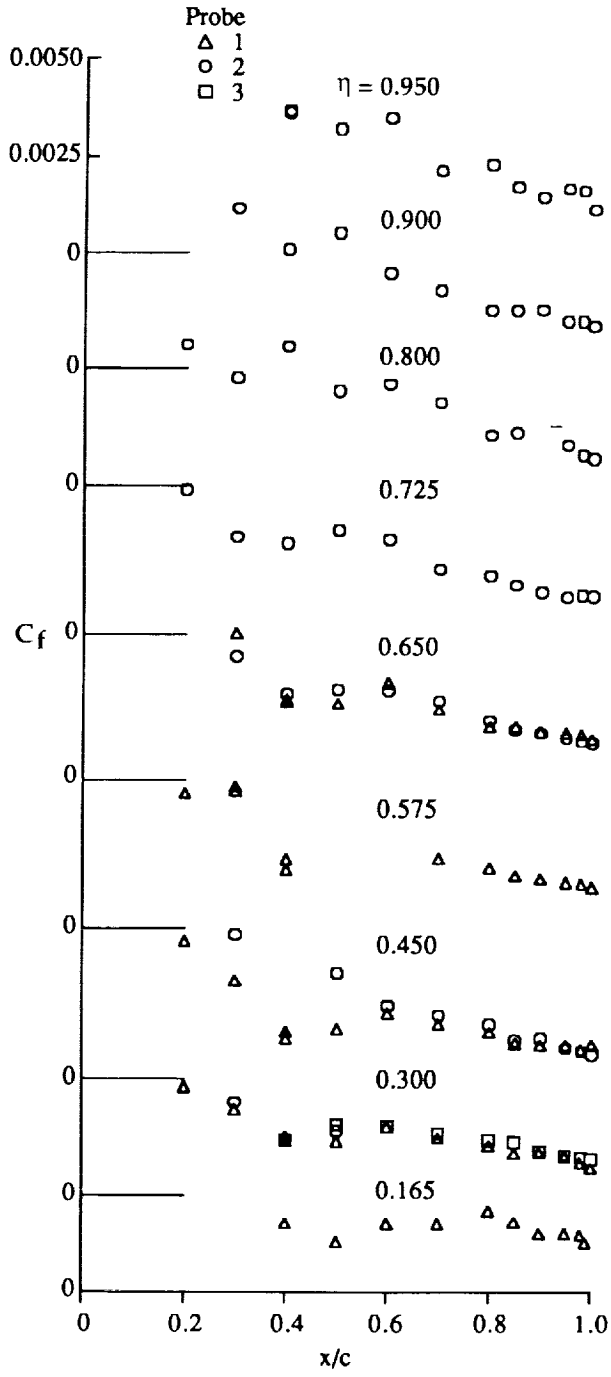

Figure 26. Skin friction distributions; $M_\infty = 0.825$, $\alpha = 4°$.

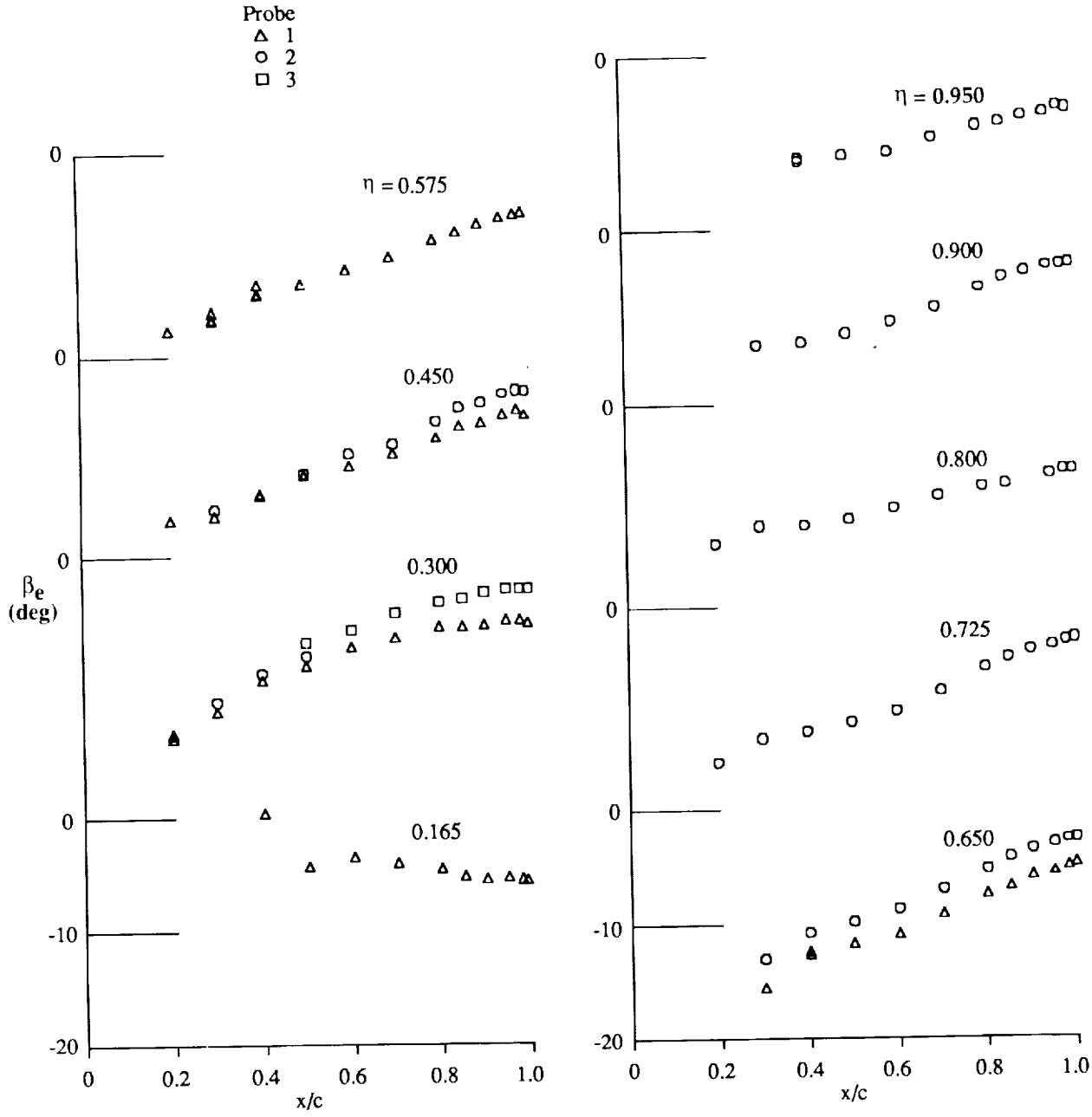

Figure 27. Distributions of yaw-plane flow direction at the boundary-layer edge (β is positive outboard); $M_\infty = 0.825$, $\alpha = 4°$.

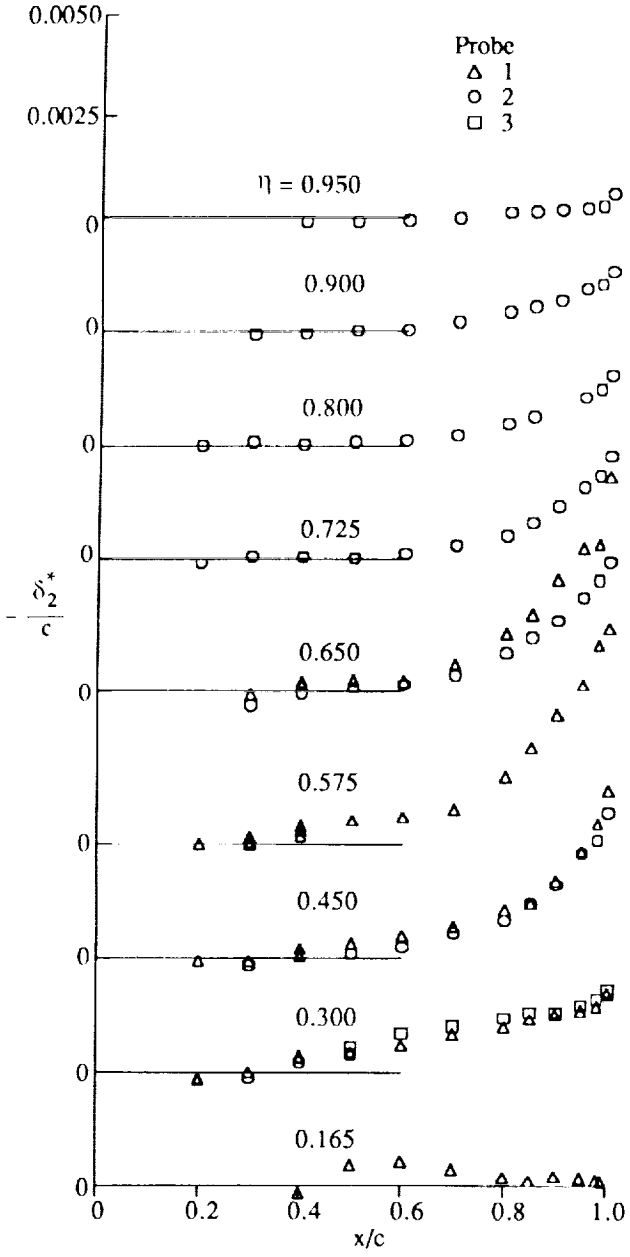

Figure 28. Crossflow displacement-thickness distribution; $M_\infty = 0.825$, $\alpha = 4°$.

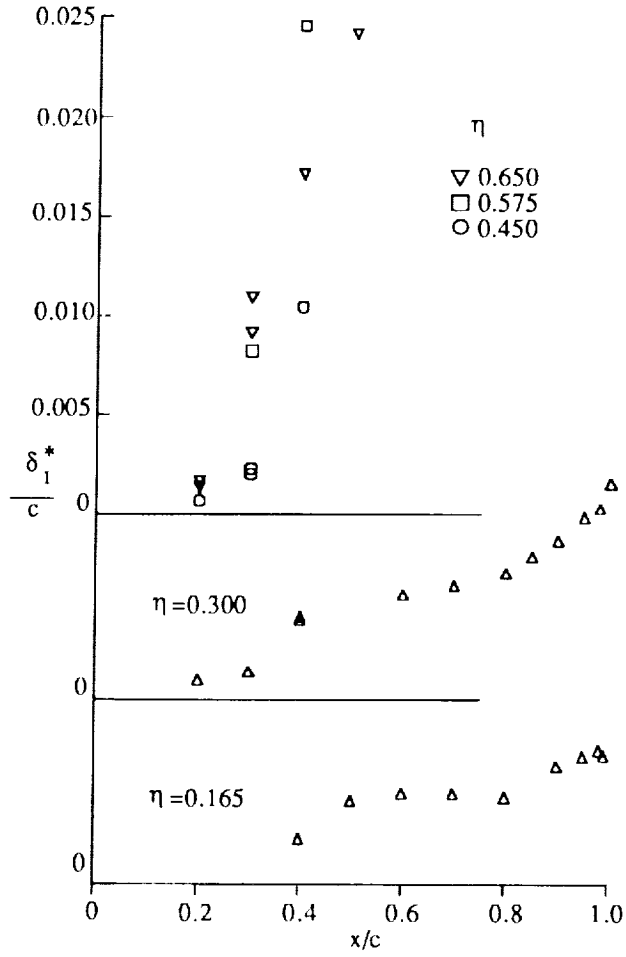

Figure 29. Streamwise displacement-thickness distributions; $M_\infty = 0.825$, $\alpha = 6°$, probe 1.

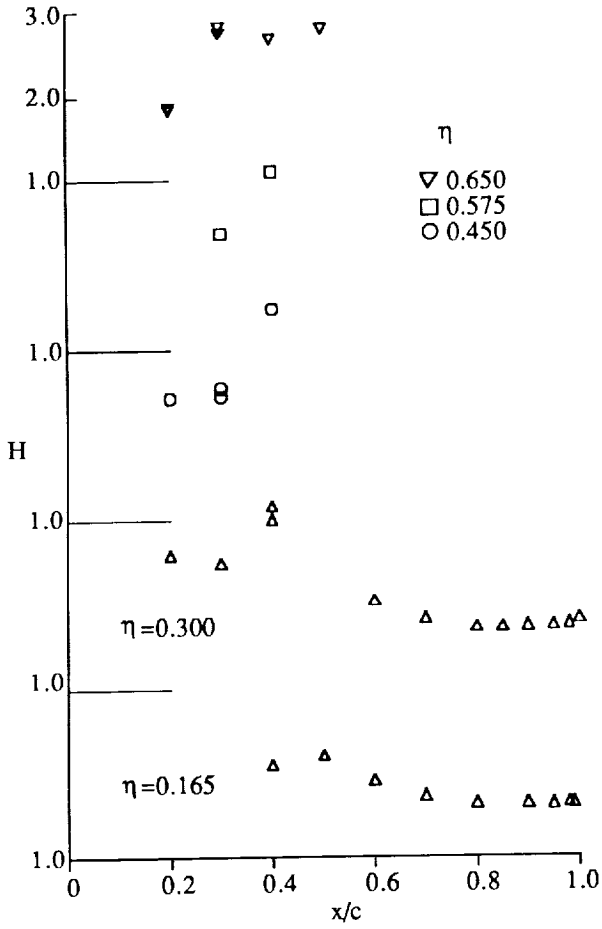

Figure 30. Shape factor distributions;
$M_\infty = 0.825$, $\alpha = 6°$, probe 1.

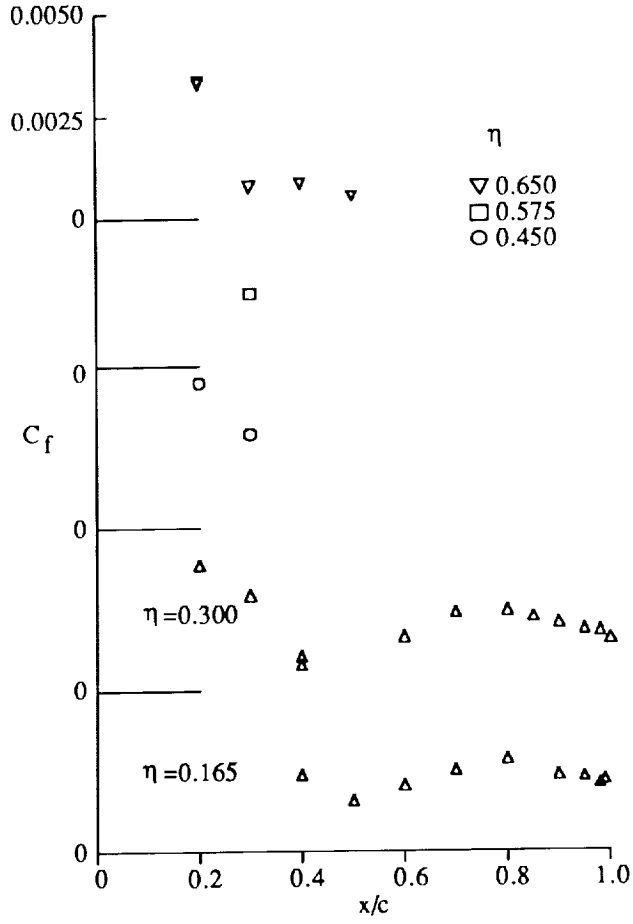

Figure 31. Skin friction distributions;
$M_\infty = 0.825$, $\alpha = 6°$, probe 1.

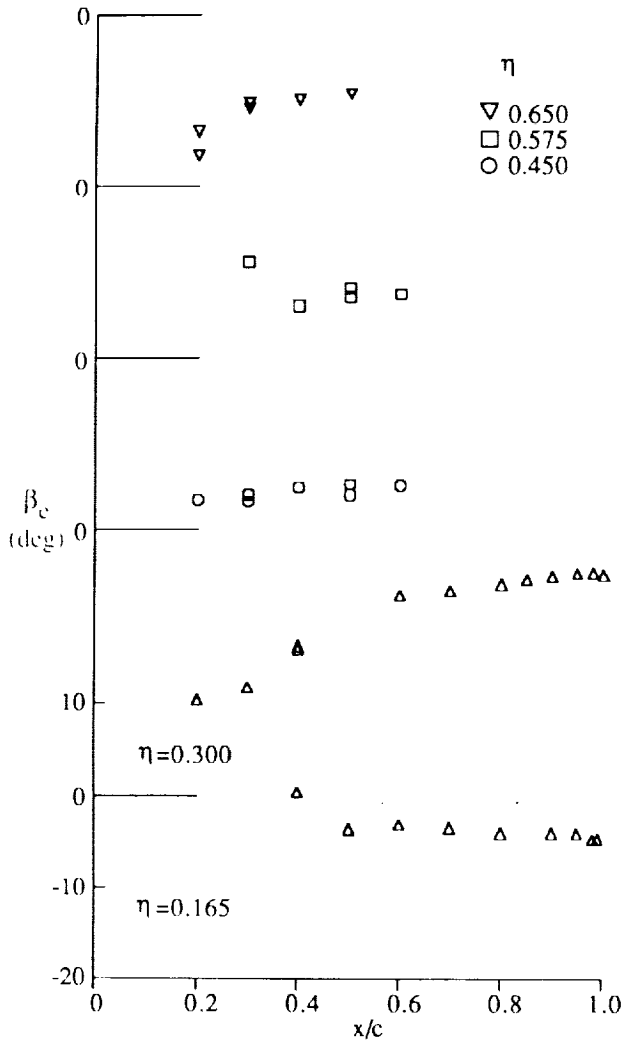

Figure 32. Distributions of yaw-plane flow direction at the boundary-layer edge (β is positive outboard); $M_\infty = 0.825$, $\alpha = 6°$, probe 1.

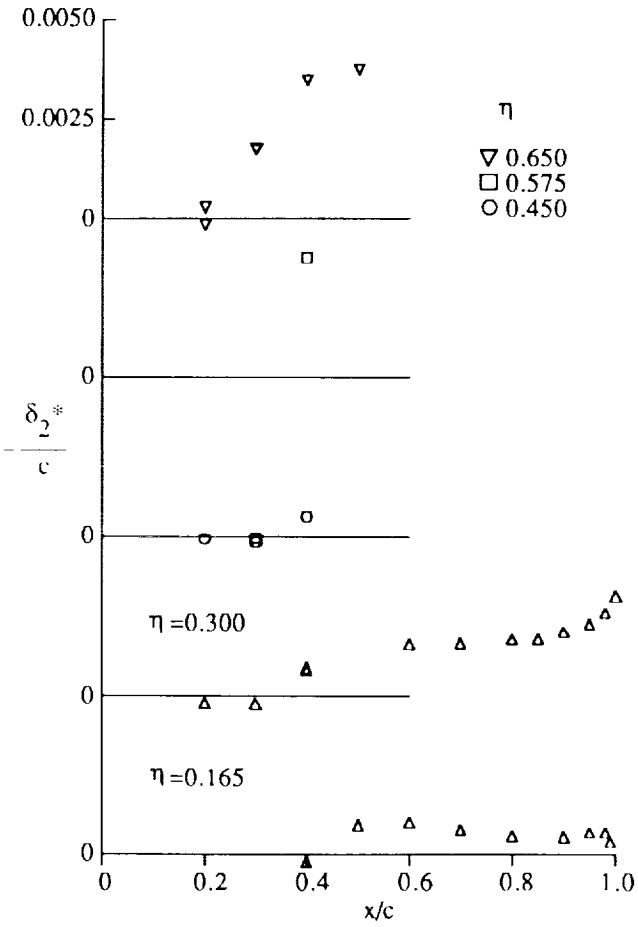

Figure 33. Crossflow displacement-thickness distributions; $M_\infty = 0.825$, $\alpha = 6°$, probe 1.

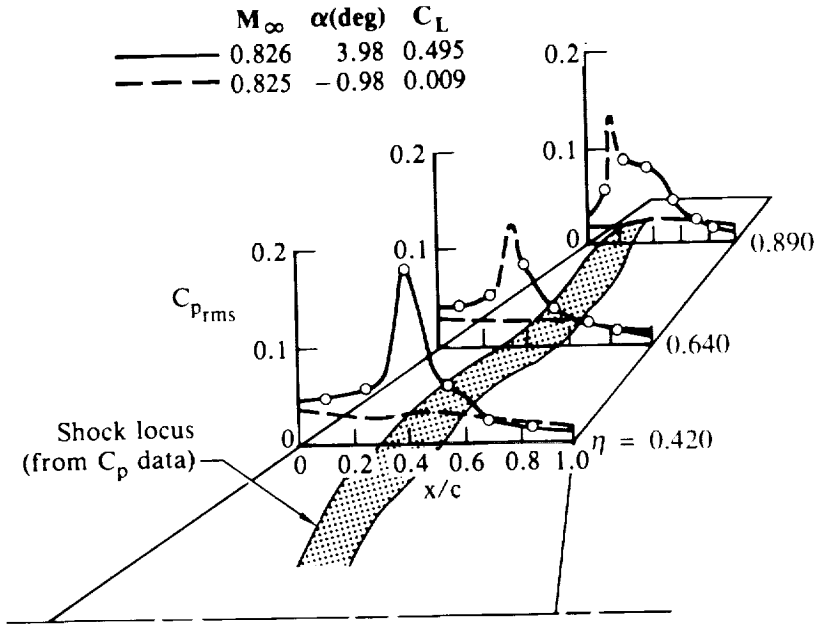

Figure 34. Pressure fluctuation intensities on wing upper surface.

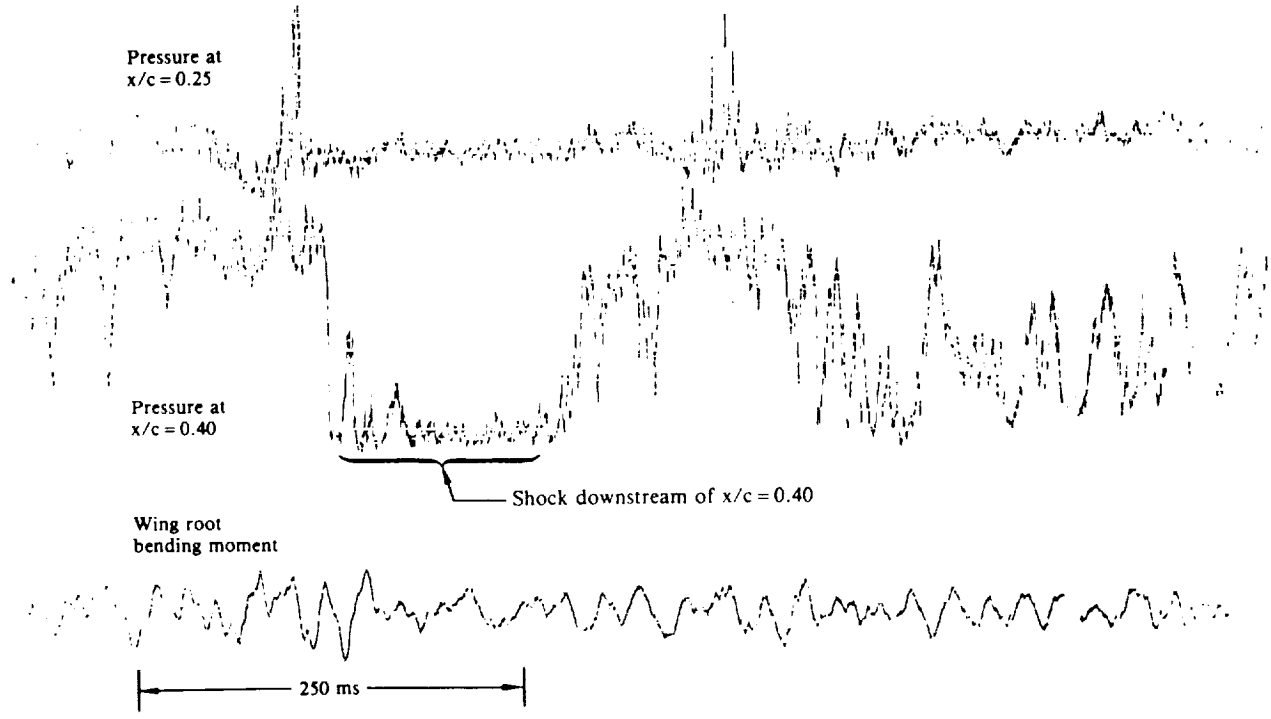

Figure 35. Pressure transducer indication of shock-wave motion; $M_\infty = 0.826$, $\alpha = 3.98°$, $\eta = 0.420$.

ORIGINAL PAGE IS
OF POOR QUALITY

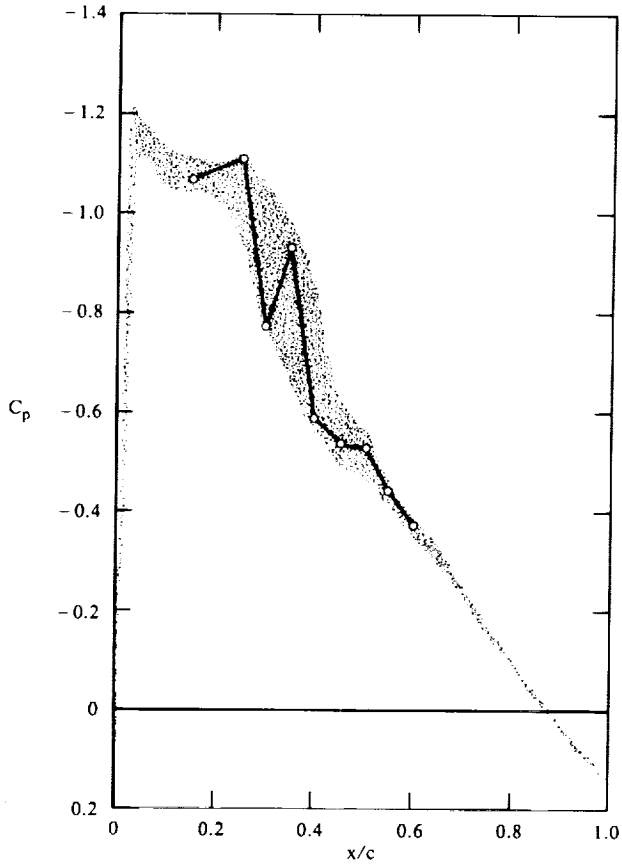

Figure 36. Envelope of 12 successive measurements of the upper-surface static-pressure distribution; $M_\infty = 0.823 \pm 0.003$, $\alpha = 4°$, $\eta = 0.450$.

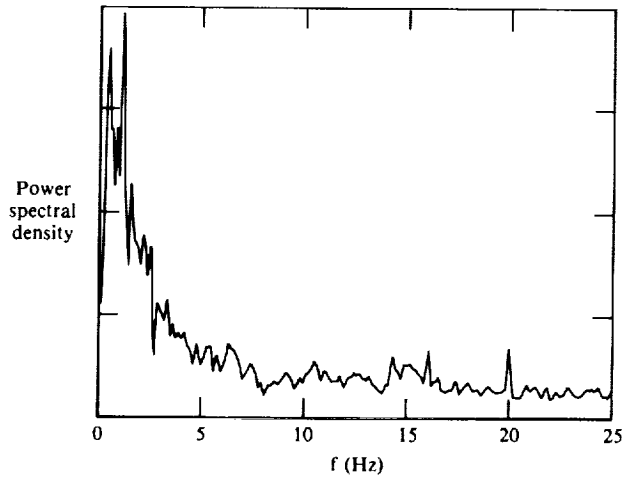

Figure 37. Power spectrum of the test-section static-pressure fluctuations in the NASA Ames 14-foot wind tunnel; $M_\infty = 0.825$.

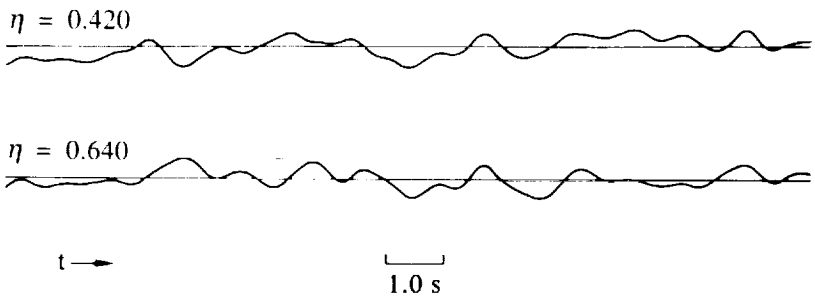

Figure 38. Low-frequency pressure fluctuations at 25% chord; $M_\infty = 0.499$, $\alpha = 5.0°$.

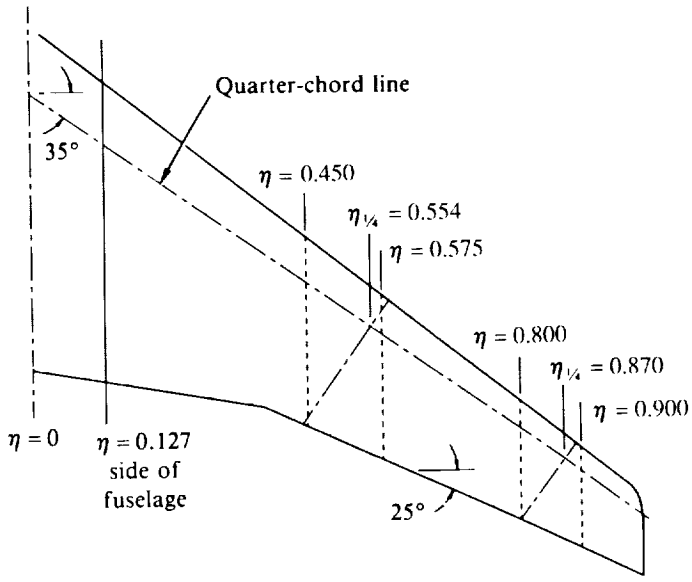

Figure 39. Spanwise locations for comparisons between measured and computed boundary-layer profiles.

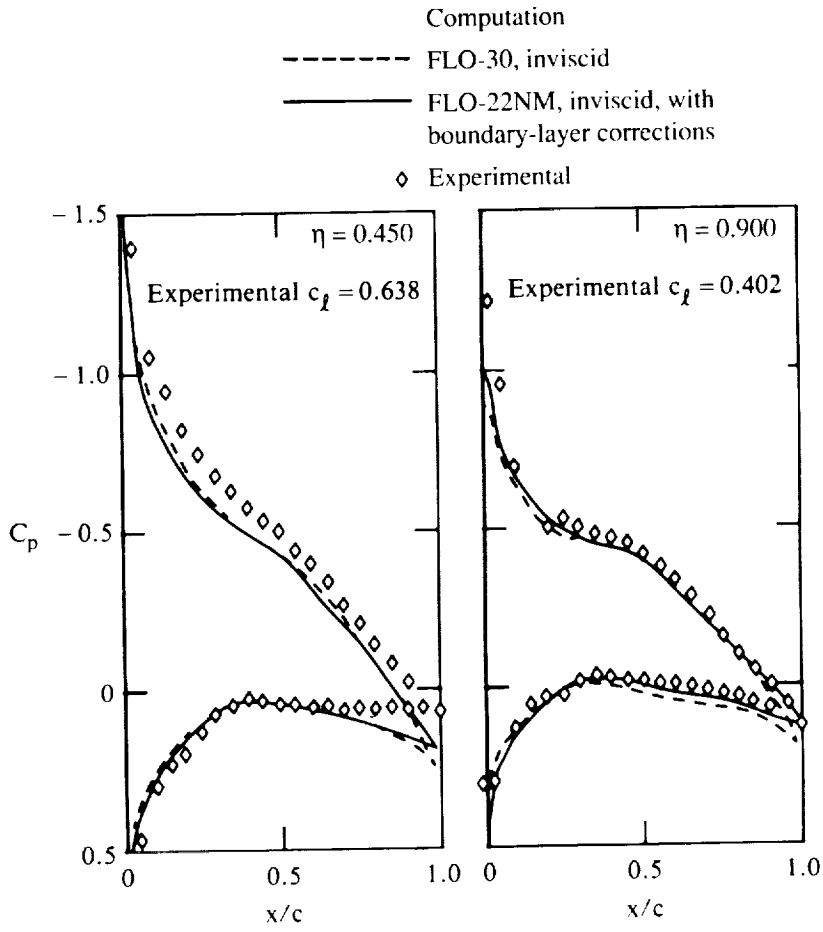

Figure 40. Surface static-pressure distributions at two spanwise stations; $M_\infty = 0.50$, $\alpha = 6°$.

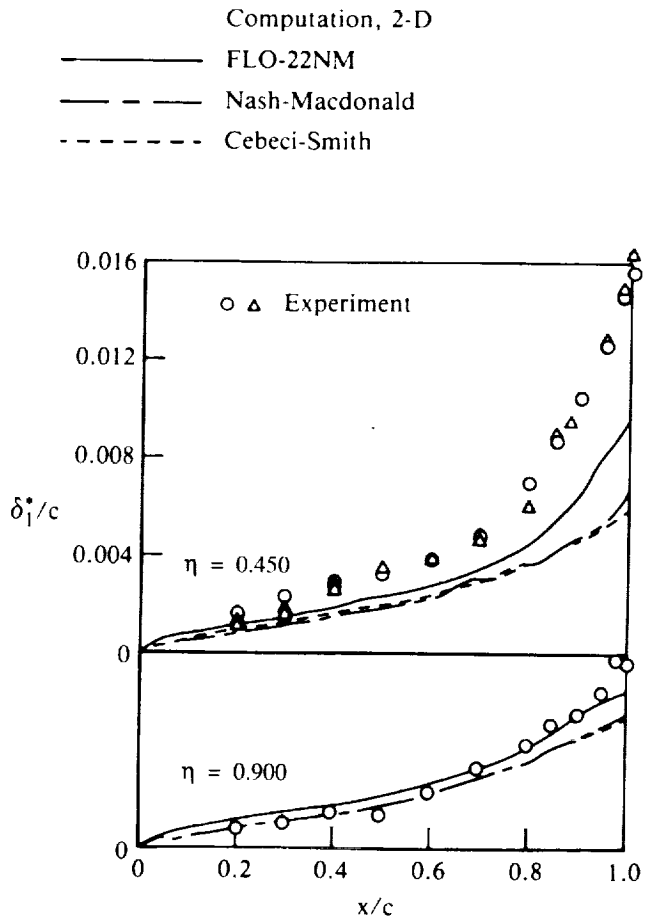

Figure 41. Measured streamwise displacement-thickness distributions and two-dimensional computations; $M_\infty = 0.50$.

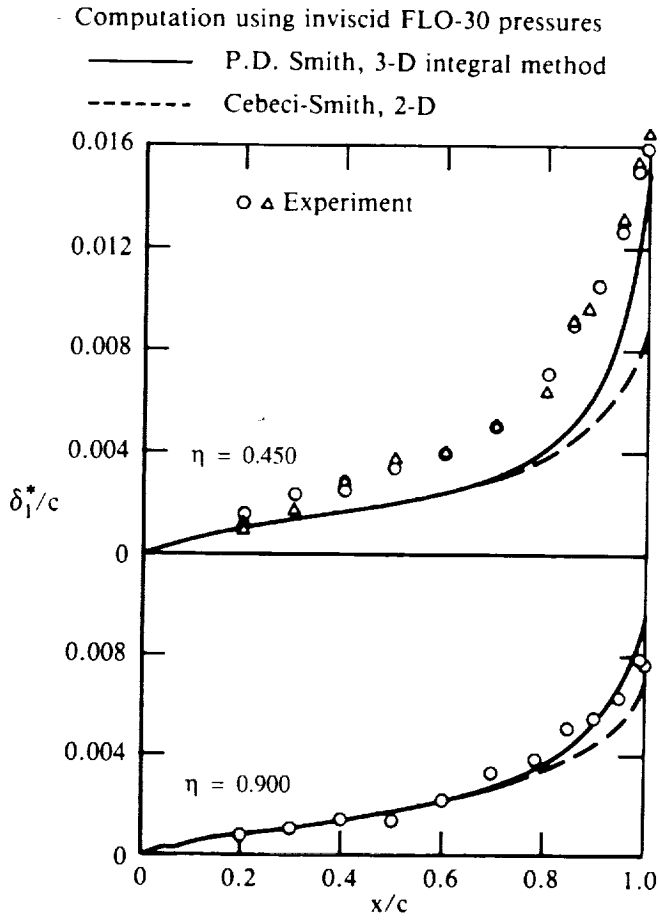

Figure 42. Measured streamwise displacement-thickness distributions and two- and three-dimensional computations; $M_\infty = 0.50$.

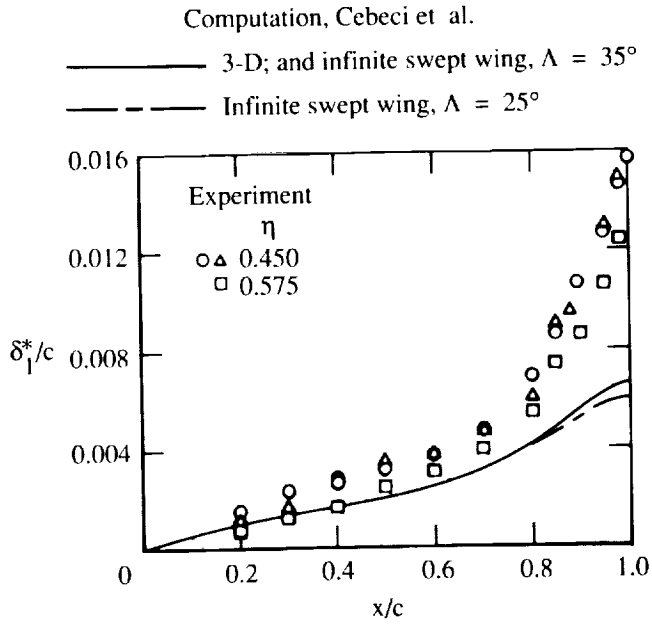

(a) Solid line represents both 3-D computation for $\eta = 0.450$ and infinite-swept-wing computation for $\Lambda = 35°$, $\eta = 0.554$. Dashed line represents infinite-swept-wing computation for $\Lambda = 25°$, $\eta = 0.554$.

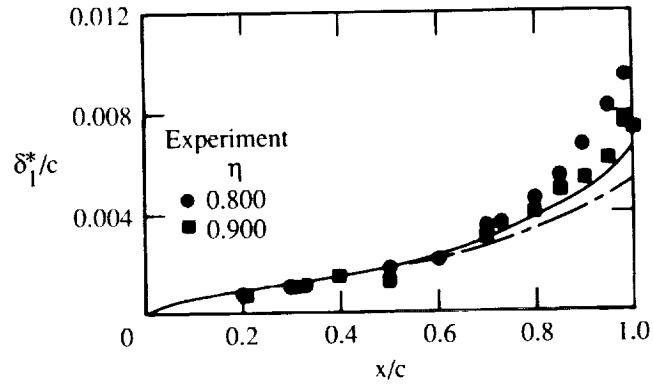

(b) Solid line represents both 3-D computation for $\eta = 0.900$ and infinite-swept-wing computation for $\Lambda = 35°$, $\eta = 0.870$. Dashed line represents infinite-swept-wing computation for $\Lambda = 25°$, $\eta = 0.870$.

Figure 43. Measured streamwise displacement-thickness distributions compared with predictions computed by methods of Cebeci et al.; $M_\infty = 0.50$.

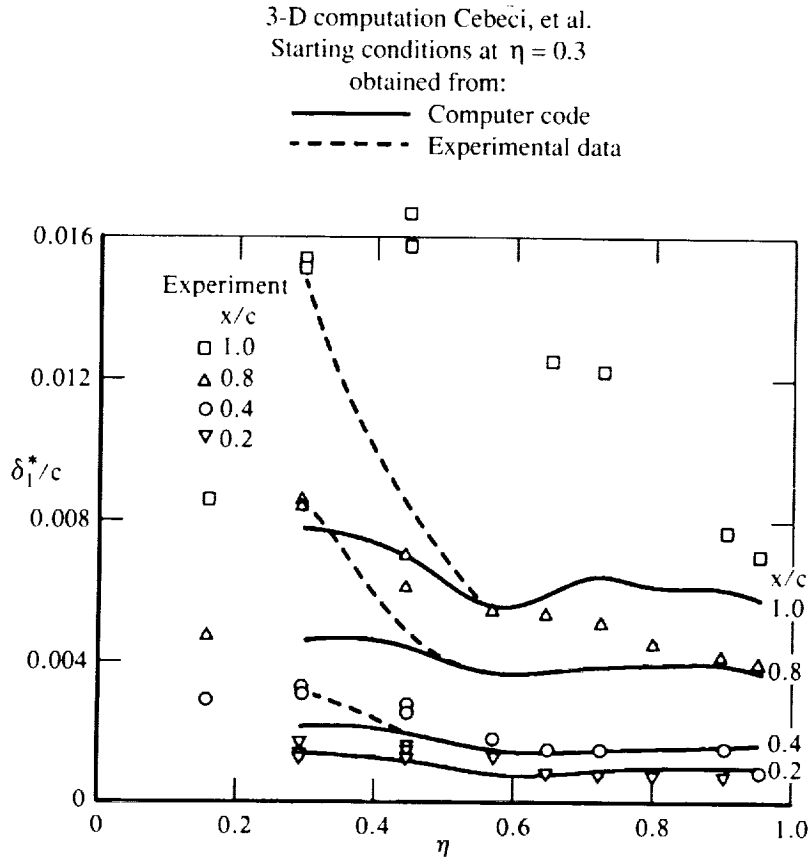

Figure 44. Spanwise variations of δ_1^*; $M_\infty = 0.50$.

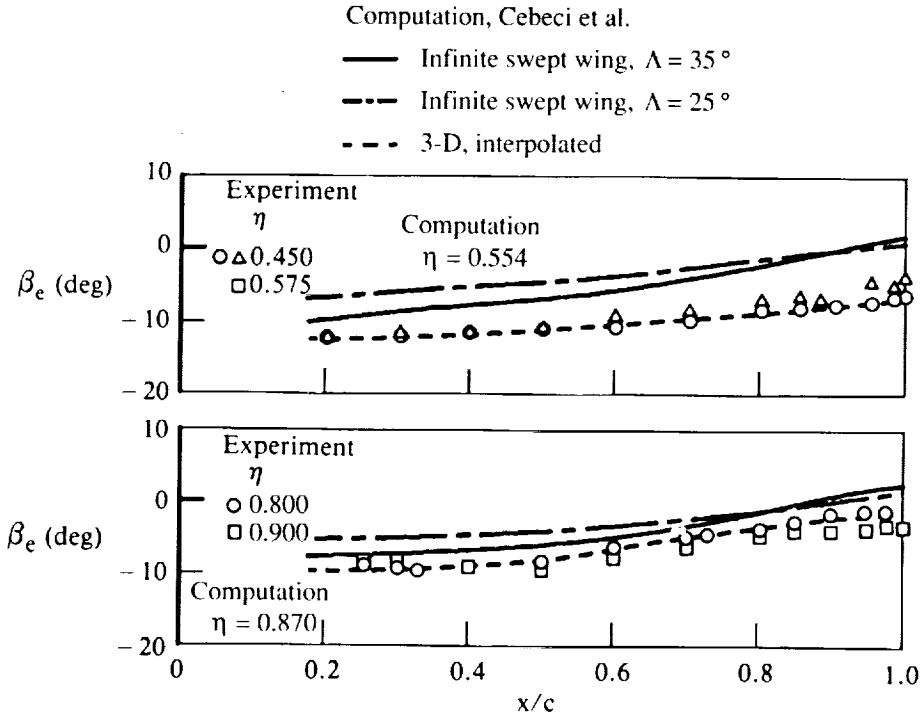

Figure 45. Measured and calculated flow directions at the boundary-layer edge; $M_\infty = 0.50$.

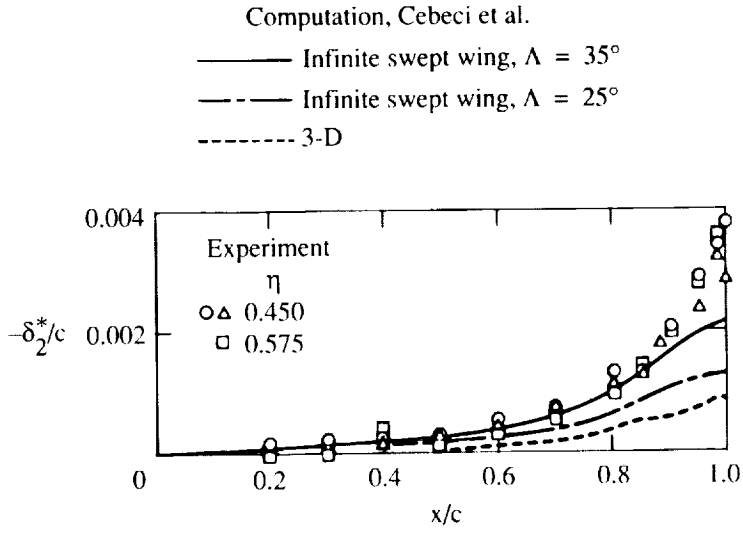

(a) 3-D computation performed for $\eta = 0.450$ and infinite-swept-wing computations for $\eta = 0.554$.

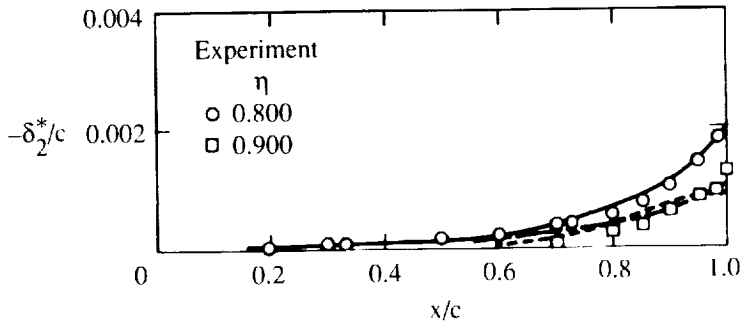

(b) 3-D computation performed for $\eta = 0.900$ and infinite-swept-wing computations for $\eta = 0.870$.

Figure 46. Measured crossflow displacement-thickness distributions compared with predictions computed by methods of Cebeci et al.; $M_\infty = 0.50$.

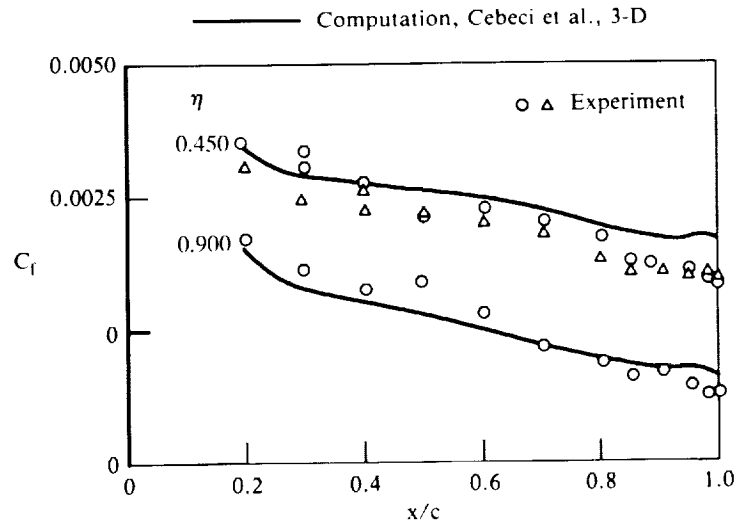

Figure 47. Measured and calculated skin-friction magnitudes; $M_\infty = 0.50$.

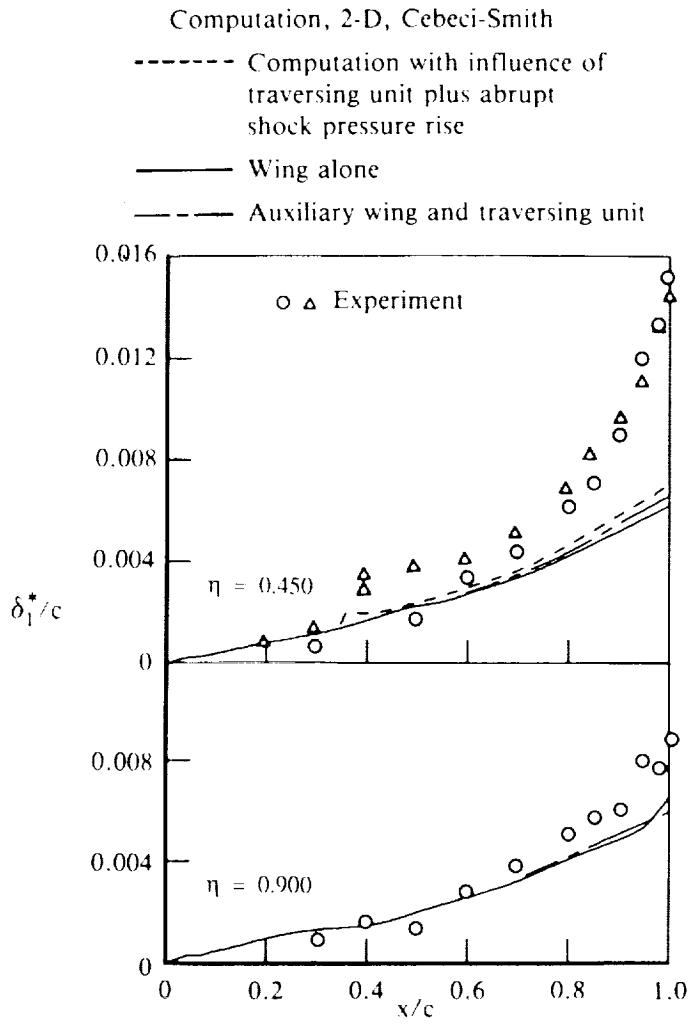

Figure 48. Measured streamwise displacement-thickness distributions and two-dimensional computations; $M_\infty = 0.825$, $\alpha = 4°$.

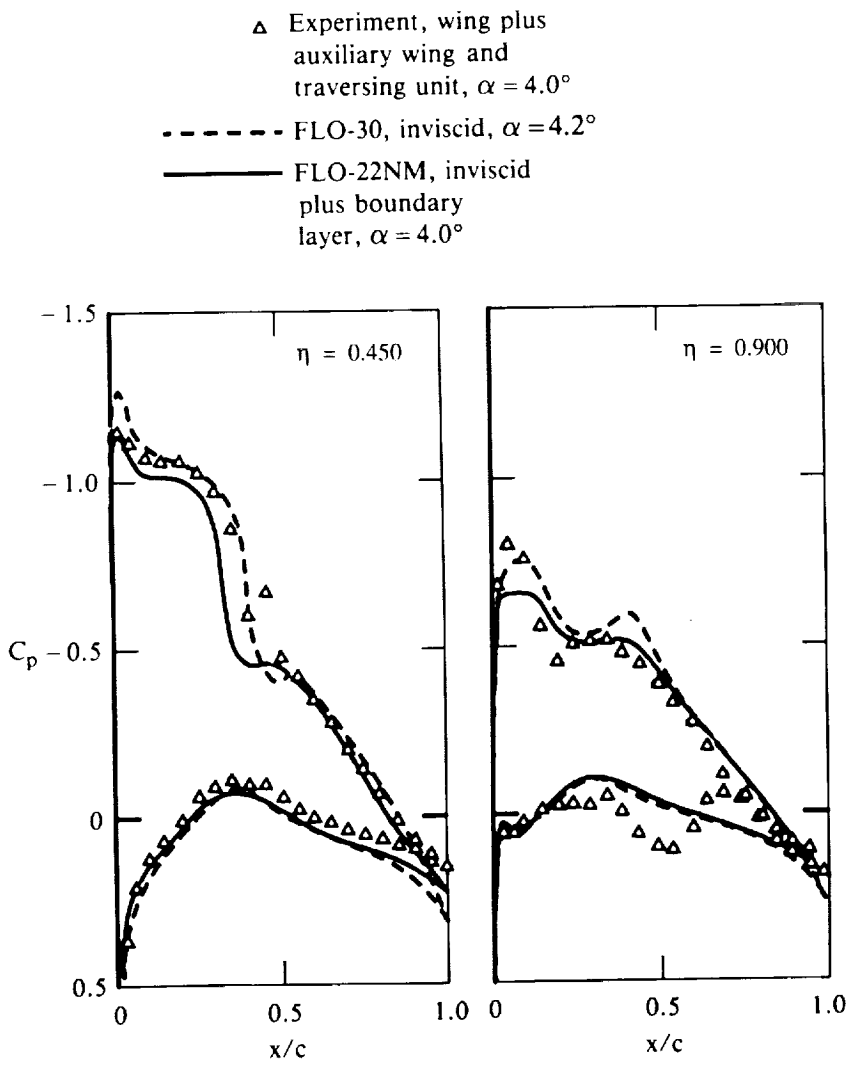

Figure 49. Surface static-pressure distributions at two spanwise stations; $M_\infty = 0.825$.

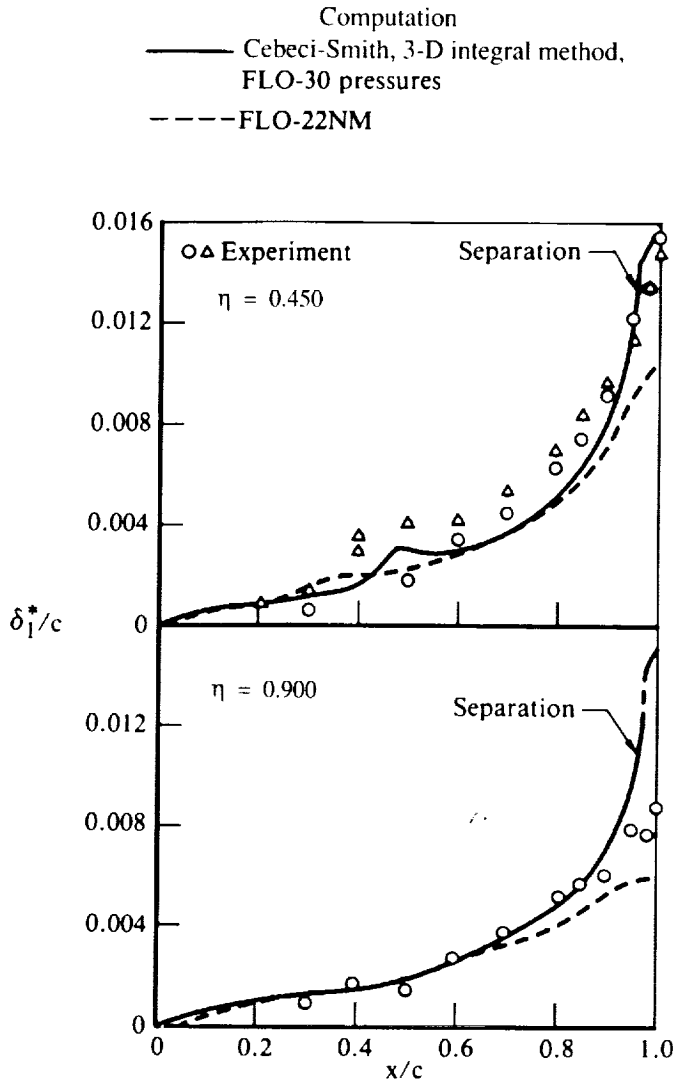

Figure 50. Measured streamwise displacement-thickness distributions and two- and three-dimensional computations; $M_\infty = 0.825$, $\alpha = 4°$.

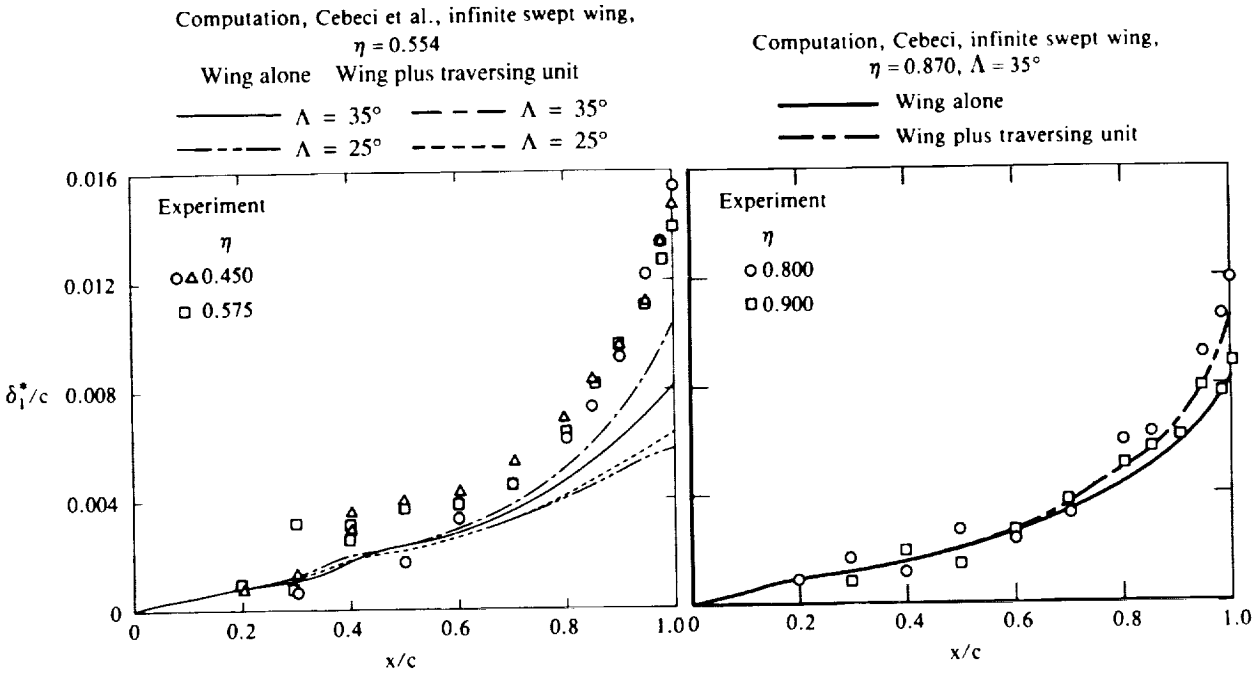

(a) Mid-semispan region (b) Tip region

Figure 51. Measured streamwise displacement-thickness distributions and infinite-swept-wing computations; $M_\infty = 0.825$, $\alpha = 4°$.

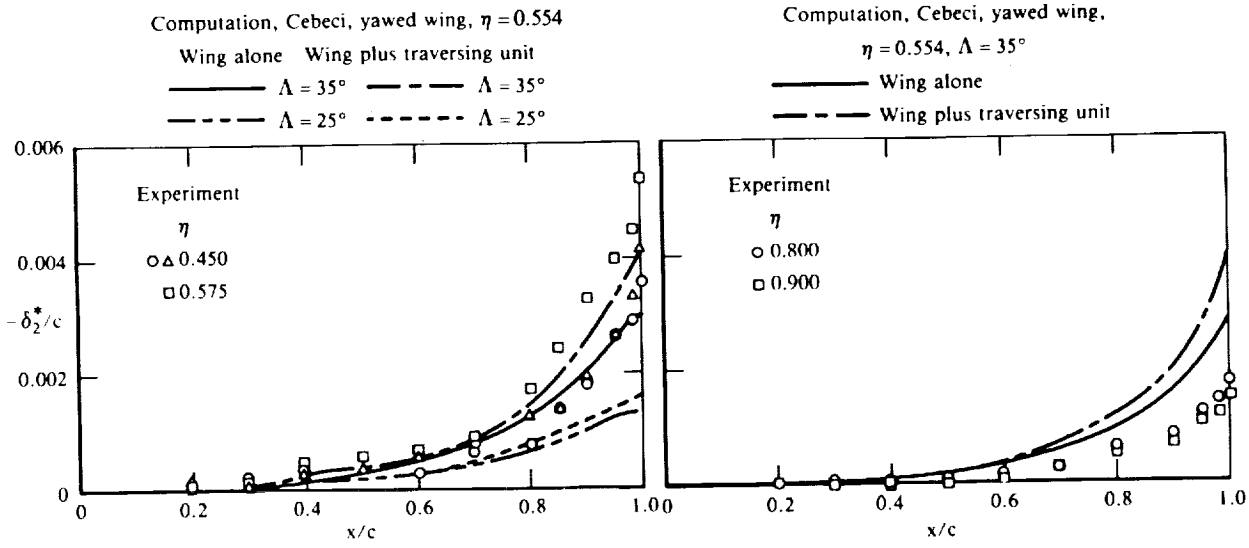

(a) Mid-semispan region (b) Tip region

Figure 52. Crossflow displacement-thickness distributions; $M_\infty = 0.825$, $\alpha = 4°$.

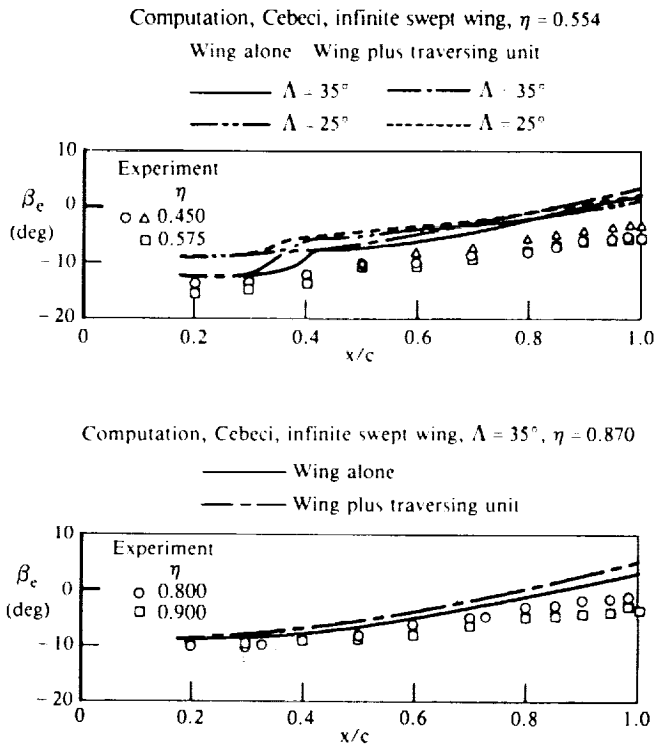

Figure 53. Measured and calculated flow directions at the boundary-layer edge; $M_\infty = 0.825$, $\alpha = 4°$.

NASA
National Aeronautics and Space Administration

Report Documentation Page

1. Report No.	2. Government Accession No.	3. Recipient's Catalog No.
NASA TM-102206		

4. Title and Subtitle

An Experimental Study of the Turbulent Boundary Layer on a Transport Wing in Subsonic and Transonic Flow

5. Report Date

August 1990

6. Performing Organization Code

7. Author(s)

Frank W. Spaid and Frederick W. Roos (McDonnell Douglas Research Laboratories, St. Louis, Missouri)
Raymond M. Hicks (Ames Research Center)

8. Performing Organization Report No.

A-89194

10. Work Unit No.

505-61-21

9. Performing Organization Name and Address

Ames Research Center
Moffett Field, CA 94035-1000

11. Contract or Grant No.

13. Type of Report and Period Covered

Technical Memorandum

12. Sponsoring Agency Name and Address

National Aeronautics and Space Administration
Washington, DC 20546-0001

14. Sponsoring Agency Code

15. Supplementary Notes

Point of Contact: Raymond M. Hicks, Ames Research Center, MS 227-2,
Moffett Field, CA 94035-1000; (415) 604-5656 or FTS 464-5656

16. Abstract

The upper-surface boundary layer on a transport wing model was extensively surveyed with miniature yaw probes at a subsonic and a transonic cruise condition. Additional data were obtained at a second transonic test condition, for which a separated region was present at mid-semispan, aft of mid-chord. Significant variation in flow direction with distance from the surface was observed near the trailing edge except at the wing root and tip. The data collected at the transonic cruise condition show boundary-layer growth associated with shock-wave/boundary-layer interaction, followed by recovery of the boundary layer downstream of the shock. Measurements of fluctuating surface-pressure and wingtip acceleration were also obtained. The influence of flow-field unsteadiness on the boundary-layer data is discussed. Comparisons among these data and predictions from a variety of computational methods are presented. The computed predictions are in reasonable agreement with the experimental data in the outboard regions where three-dimensional effects are moderate and adverse pressure gradients are mild. In the more highly loaded mid-semispan region near the trailing edge, displacement-thickness growth was significantly underpredicted, except when unrealistically severe adverse pressure gradients associated with inviscid calculations were used to perform boundary-layer calculations.

17. Key Words (Suggested by Author(s))	18. Distribution Statement
Boundary layer CFD Wing-body design	Unclassified-Unlimited Subject Category - 02

19. Security Classif. (of this report)	20. Security Classif. (of this page)	21. No. of Pages	22. Price
Unclassified	Unclassified	78	A05

NASA FORM 1626 OCT 86

For sale by the National Technical Information Service, Springfield, Virginia 22161